THE PREDICTION OF SURFACE SETTLEMENTS DUE TO TUNNELLING IN SOFT GROUND

by

LILY CHOW

A Thesis submitted for the

Degree of Master of Science at the

University of Oxford

Brasenose College

Trinity Term, 1994

Abstract

The prediction of surface settlements due to tunnelling in soft ground.

L. Chow
Brasenose College, University of Oxford.

A Thesis submitted for the degree of Master of Science.
Trinity Term, 1994.

The investigation of various soil models for the prediction of surface settlement profiles due to the excavation of a single tunnel in soft ground is described in this thesis. Both analytical and numerical methods are used. Emphasis is placed on the establishment of the width of the predicted settlement trough.

In the analytical analysis the ground is assumed to be an elastic half-space. The problem is approached using two methods: (i) the application of a line load to model the uplift of soil caused by the excavation; (ii) the application of Sagaseta's method which models the soil deformation due to ground loss.

For the numerical analysis of the tunnelling problem, the finite element program OXFEM is used. Finite element modelling for the simulation of tunnelling is investigated. The mesh size used in the analysis is found to have an important impact on the computed results. Parametric studies using linear elastic and elastic-plastic models are carried out. The effect of stress and strain amplitudes on the behaviour of soil is also investigated. The non-linear elastic model assumes a power law between the elastic moduli and the mean effective stress, and represents the increase of stiffness with increasing stress amplitudes in the elastic region of the soil. The effect of strain amplitudes on the behaviour of soil is considered using an elastic-plastic model with nested yield loci and an outer von Mises surface. Both models have been implemented in OXFEM, and parametric studies on tunnelling are carried out using both models. Comparison between the computed results and existing empirical values of the widths of settlement troughs were carried out.

Acknowledgements

I am particularly grateful to Dr. Harvey Burd and Prof. Guy Houlsby, who supervised my research described in this thesis. They have been very supportive, and have given me invaluable advice on the preparation of this thesis. I wish to record my sincere appreciation of their help and guidance. I should wish to thank Prof. Guy Houlsby for providing me a copy of the program for the nested yield loci model, which made the implementation of the model an easier task. I should also like to thank every member of the Oxford Soil Mechanics group for their advice and encouragement.

Finally, I would like to thank my friends for being extremely patience and considerate during the period that this thesis was in preparation. I am indebted to my family, who made this research possible by their support.

Contents

Nomenclature

$\boldsymbol{B}$	matrix relating strain rate and nodal velocities
c	cohesion
c_{ijkl}	compliance tensor
C	depth of tunnel crown below ground surface
$\boldsymbol{C}$	compliance matrix
d_{ijkl}	stiffness tensor
D	diameter of tunnel
$\boldsymbol{D}$	material stiffness matrix
E	Young's modulus
E	complementary energy (Chapter 5)
F	Free energy
G	shear modulus
G_0	Shear modulus at ground surface
h	work-hardening parameter
H	depth of rigid base below ground surface
H_d	depth of rigid base below tunnel axis
i	width of settlement trough
$\boldsymbol{K}$	element stiffness matrix
m	rate of change of shear stiffness with depth
n	exponent determining influence of pressure on elastic moduli
N	stability ratio
OCR	overconsolidation ratio

p'	mean effective stress
p_a	atmospheric pressure
$\boldsymbol{P}$	vector of nodal forces
R	radius of tunnel
s_u	undrained shear strength
s_{u0}	undrained shear strength at ground surface
$\dot{\boldsymbol{U}}$	vector of nodal velocities
v	ground loss
Z	depth of tunnel axis
δ_{ij}	Kronecker delta
δ_{max}	maximum surface settlement
δ_r	radial movement of soil
δ_z	vertical movement of soil
ϵ_{ij}	strain tensor
$\dot{\epsilon}_{ij}$	strain rate tensor
$\boldsymbol{\epsilon}$	vector of strain
$\dot{\boldsymbol{\epsilon}}$	strain rate vector
ϵ'_{ij}	deviatoric strain tensor
$\dot{\epsilon}'_{ij}$	deviatoric strain rate tensor
γ	total unit weight of soil
ν	Poisson's ratio
ρ	rate of change of undrained shear strength with depth
σ_{ij}	stress tensor
$\dot{\sigma}_{ij}$	stress rate tensor
$\boldsymbol{\sigma}$	vector of stress
$\dot{\boldsymbol{\sigma}}$	stress rate vector

σ'_{ij}	deviatoric stress tensor
$\dot{\sigma}'_{ij}$	deviatoric stress rate tensor

Superscripts

e	elastic value
p	plastic value

Chapter 1

INTRODUCTION

1.1 Shallow Tunnel Analysis

Construction of shallow tunnels in soft clay can result in significant surface settlements. Since tunnel construction often takes place beneath urban areas, engineers are faced with the problem of predicting these settlements.

In most analyses of geotechnical problems, simple elastic or elastic-plastic models are used to represent the behaviour of soils. However, in the analysis of shallow tunnelling, this simplification can result in inaccurate predicted settlement profiles. A more practical model which can account for the realistic behaviour of soils is required.

Real soils behave in a more complex way than that described by elastic homogeneous models. Non-linearity has a marked effect on the patterns of stresses and strains around a tunnel (Gunn, 1993). Various laboratory tests and in-situ field measurements show that elastic moduli vary with stress and strain levels (eg. Duncan & Chang, 1970, Jardine *et al*, 1984). As computer based numerical and finite element analysis techniques are becoming more advanced different soils and non-linear stiffness profiles can be modelled (eg. Prevost, 1979, Jardine *et al*, 1991). This means that ground movements for

complex geotechnical problems can be predicted more accurately.

1.2 Empirical and Closed Form Solutions

Peck (1969) established an empirical method of representing surface settlements due to tunnelling. Based on data from a variety of sources, his results showed that the settlements above a tunnel are approximately symmetrical about the vertical axis of the tunnel. Peck showed that surface settlements occurring in the field could be approximated by an error function curve (Fig. 1.1). Although not theoretically justifiable, it provided a method for estimating the settlements at varying distances from the centreline of the tunnel. He established a correlation between the relative depth of tunnel and the point of inflection of the tranverse surface settlement trough for various soil types (Fig. 1.2). Peck's investigation provides a guideline for the prediction of ground loss and settlement that occur in connection with tunnelling.

Sagaseta (1987) established a closed form solution for a strain field in an initially isotropic and homogeneous incompressible soil due to near-surface ground loss. For the determination of surface settlements, it was found that the effect of the free surface could be approximately modelled by doubling the movements calculated for an infinite space. He showed that, where displacements are imposed at some points and only the resulting strain field was required, the incompressiblity equation provided much of the information. Hence if the remaining boundary conditions could be reasonably simplified so that this equation could be integrated, the solution obtained would be close to the exact solution. Even in compressible materials, the assumption of a known value of the volumetric strain would lead to a valid solution.

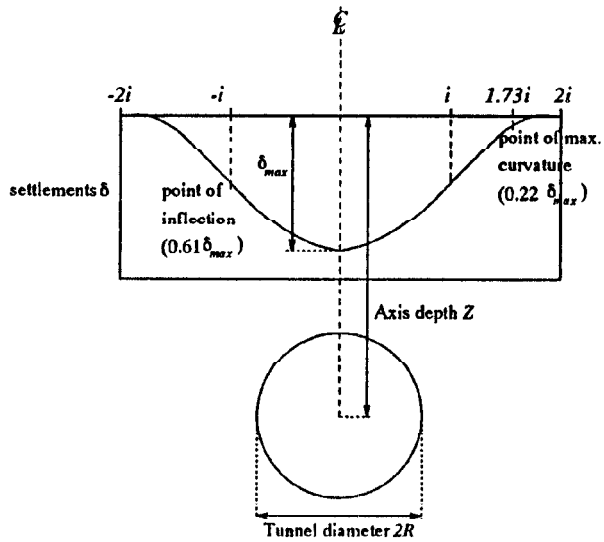

Figure 1.1: Properties of error function curve to represent cross-section settlement trough above tunnel. (After Peck, 1969)

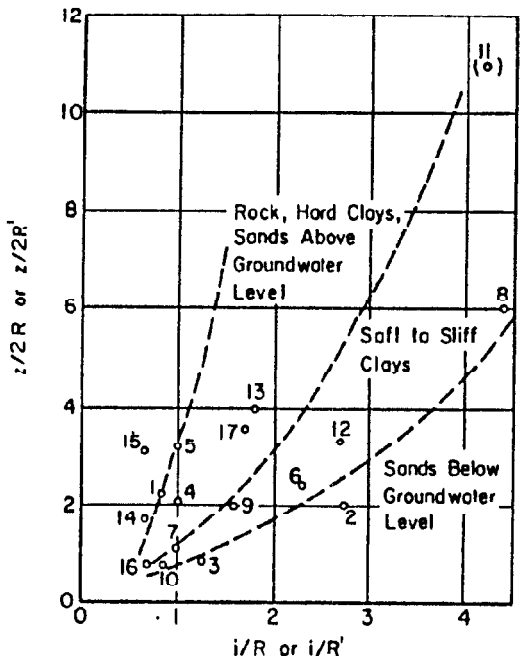

Figure 1.2: Relationship between width of settlement trough as represented by $\frac{i}{R}$, and dimensionless depth of tunnel $\frac{Z}{2R}$ for various tunnels in different materials. (After Peck, 1969)

Mair and Taylor (1993) carried out tunnel analyses using two different methods of simulating the tunnelling process. They found that the unloading of a spherical cavity is a reasonable approximation for predicting the behaviour of clay around tunnel heading, while the movement above and to the side of the tunnel can be reasonably predicted by the unloading of a cylindrical cavity. The closed form plasticity solution for a fully unloaded cylindrical cavity used in the calculation of the soil deformation was:

$$\frac{\delta_r}{a} = \frac{s_u}{2G}\left(\frac{a}{r}\right)exp(N-1) \tag{1.1}$$

where δ_r is the radial movement at radius r, a is the inner radius of the tunnel. The parameter N is the stability ratio, and is equal to $\frac{\sigma_0}{s_u}$, where σ_0 is the initial total stress at the cavity boundary. For $N = 1$, the soil behaved elastically. For larger values of N, a plastic zone developed around the tunnel which strongly influenced the magnitude of the deformations. By carrying out back analysis of field measurements around $4m$ diameter tunnels in London Clay, they showed that for a linear elastic, perfectly plastic soil model an elastic stiffness given by the ratio $\frac{G}{s_u} = 100$ was reasonable for prediction of ground movements. For most tunnels in London Clay at depths between 20m and 40m, the stability ratio was found typically between 2.5 and 3.

1.3 Non-linear Soil Models

Soils are neither linear nor elastic, even at very small strains. The moduli required to give reasonable predictions are average quantities, rather than measurable properties. It has been shown that the non-linear stress-strain curves of soil may be approximated by hyperbolae. Janbu (1963) performed

experimental studies and showed that the relationship between initial tangent modulus and confining pressure in the tests could be expressed as

$$E_i = kp_a\left(\frac{\sigma_3}{p_a}\right)^n \tag{1.2}$$

where E_i is the initial tangent modulus, σ_3 is the minor principal stress, p_a is the atmospheric pressure. The parameter k is a modulus number, and n is the exponent determining the rate of variation of E_i with σ_3.

Duncan and Chang (1970) investigated the non-linearity, stress dependency, and inelasticity of soil. On unloading and reloading of silica sand, Duncan and Chang found that the variation of the value of the modulus with confining pressure could be represented by

$$E_{ur} = k_{ur}p_a\left(\frac{\sigma_3}{p_a}\right)^n \tag{1.3}$$

where the subscripts ur correspond to the unloading-reloading value. The parameter n was the same as for primary loading (equation 1.2), but the value of k_{ur} was found to be higher than for primary loading.

It is well known that the results of laboratory triaxial tests are difficult to correlate with stiffness back-figured from measurements on full-scale structures. This is because conventional determination of the axial stiffness of a triaxial sample is based on external measurements of displacement which include a number of adventitious movements due to the compliances of the loading system and load measuring system. These errors added to a variety of sample bedding effects to give a poor definition of the stress-strain behaviour of the material under test, particularly over the small strain range. Therefore, most triaxial tests tend to give apparent soil stiffnesses far lower then those inferred from field behaviour. Threshold effects have also been

reported in soils. Atkinson (1973) concluded that: "These tests, and other like them, seem to indicate that where a delay at constant stress state is involved or where the direction of the stress probe differs from the previous stress path the strains produced by a small stress increment may be much smaller than the strains produced by a larger increment or those where there was no rest period or where the direction of the stress probe did not deviate much from the previous loading path. This apparent stiffening of a soil at small stress increments may be likened to a threshold effect; that is to say that there exists a threshold of the probing stress increment below which the soil is apparently very much stiffer than for a larger probe."

Simpson *et al* (1979) proposed an elastic-plastic stress-strain model for soil model in which a bilinear elasticity was assumed to account for the threshold effects in soil. The model had an initial elastic stiffness ten times larger than the stiffness obtained from laboratory tests when the strain was less than a threshold value of about 0.02%. These properties were used up to the plastic yield point. The threshold strain was represented by a kinematic yield surface. This defined a small zone in stress (or strain) space such that the higher stiffness applied to an element of soil until its stress (or strain) state reached the kinematic yield surface. A change in the direction of loading would lead to a certain amount of straining with the initial higher moduli until the kinematic yield surface was activated again. This model could greatly improve the prediction of soil movement due to excavations, but was, at that time, rather complex. However, it was important in that it was the first method to use a kinematic yield surface to represent a strain hardening effect and this would allow development of a non-linear model.

Jardine, Symes and Burland (1984) made laboratory measurements of soil stiffness using triaxial tests. They used local strain measurement devices which could resolve mean axial strain as low as 0.002%, and found that elastic moduli of soil continually reduced from strains as low as 0.005% until failure was reached. These measurements generally support the basic approach of Simpson *et al* (1979), but give a different detailed picture of soil stiffness at low strains.

Jardine *et al* (1991) described the practical application of a simple non-linear model for predicting ground movements. They suggested a non-linear ground model which consisted four distinct phases of behaviour of soil (Fig. 1.3).

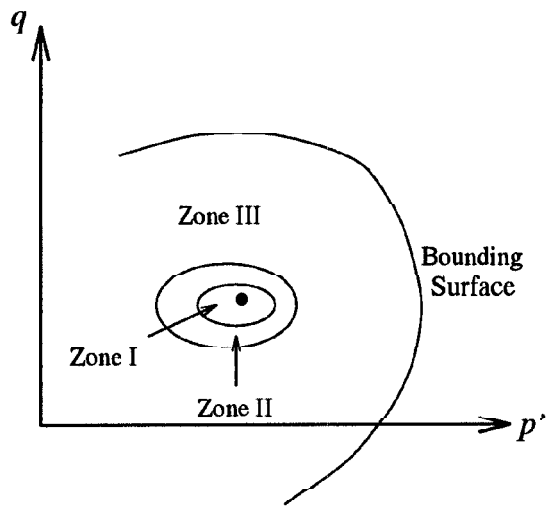

Figure 1.3: Non-linear model suggested by Jardine *et al* (1991).

The stress path engaged the boundaries to three zones (Zone I, II and III). Zone I corresponded to a region of true linear elastic behaviour. In Zone II the stress-strain behaviour was non-linear and hysteric. Strains were fully recoverable in complete load-unload cycles. Stiffness in this zone was strongly

influenced by recent stress history. The main feature of Zone III was the development of irrecoverable strains. Large scale changes in particle arrangement occurred when the stress path reached the last phase, the Bounding Surface. Stiffness was greatly reduced. This Bounding Surface was represented by a Mohr-Coulomb elastic-plastic model. Surface settlements and horizontal ground movements predicted using a non-linear elastic-plastic model to represent the Bounding Surface model for a deep basement formed in Central London were compared with field measurements during and after the excavation. The shear stiffness of the model was assumed to be dependent on the strain level of the soil. The results showed good agreement between predicted values and field measurements.

Much recent attention has centred around the type of diagram shown in Fig. 1.4, often refered to as the 'S-shaped' curve. It shows how soil stiffness is high when the strains are small, but reduces as straining proceeds.

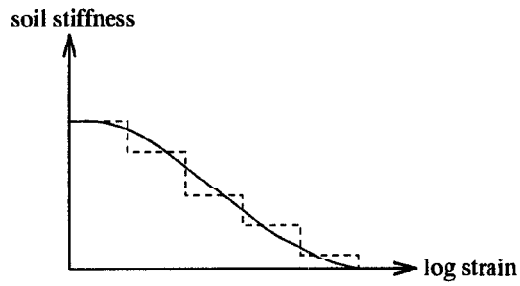

Figure 1.4: S-shaped curve showing change in stiffness with straining.

Simpson (1992) expressed this idea of non-linearity in drained analyses of soil with an analogue of bricks on strings pulled by a man. The man was taken to represent the point in the strain space of a small element. Each brick represented a proportion of the element. Movement of a brick repre-

sented plastic strains, and the elastic strain is given by the difference between the movement of the man and the sum of the movement of the bricks, each weighted by the proportion of the soil it represented. Thus, the S-shaped curve can be modelled in a stepwise fashion as shown by the dotted line in Fig. 1.4. The model reproduced small strain effects in soil and predicted the response of soil to abrupt changes in stress path.

1.4 Finite Elements in Tunnel Analysis

Zienkiewicz (1977) described the finite element method as 'a general discretisation procedure of continuum problems posed by mathematically defined statements.' The mathematically defined statements include stress-strain relationship of soils, compatibility equations, equilibrium and boundary conditions. The advantage of using finite element methods in the analysis of geotechnical problems is that it allows complex situations to be modelled. Complicated non-linear soil models can also be incorporated fairly easily.

Mair *et al* (1981) carried out finite element analysis on shallow tunnels using a program incorporating the Modified Cam-Clay model. The shape of the yield curve was assumed to be elliptical. Energy was dissipated plastically within the clay. Elastic behaviour was assumed to be isotropic, with elastic moduli dependent on the current mean effective stress. In-situ horizontal stresses were specified in the computation. As well as performing finite element analysis, centrifugal model tests were carried out to provide experimental data for comparison with finite element predictions. It was shown that predicted settlement troughs from finite element analysis using the Modified Cam-Clay model were considerably wider than experimental re-

sults. The shape of settlement troughs were also significantly different from an error function curve. The Modified Cam-Clay model therefore does not appear to be suitable for the prediction of settlement profiles in tunnelling.

Oteo and Sagaseta (1982) investigated the effect of discretisation on finite element tunnel analysis using a linear elastic model. They considered three factors introduced artificially in finite element analysis: the lateral boundary, the bottom rigid base, and the discretisation into finite elements. It was found that the effect of the bottom rigid base is the most important. When the depth of the rigid base below the tunnel axis, H_D, increases, the settlements decrease, resulting in surface heave for a value of $\frac{H_D}{D} > 7$, where D is the diameter of the tunnel. At the same time, Oteo and Sagaseta related the point of inflection of the settlement trough to the depth of the tunnel. The vertical settlement profiles were fitted to an error function curve defined by their maximum displacement, δ, and the abscissa of the inflection point, i. The computed value of i and the depth of the tunnel axis Z were related by the equation:

$$\frac{i}{D} = 2.1\frac{Z}{D} - 0.84 \tag{1.4}$$

The agreement between equation 1.4 and the empirical results established by Peck (1969) was not satisfactory.

Gunn (1993) suggested a non-linear soil model which assumed a power law expression between the undrained stuffness and deviator strain as given in equation 1.5:

$$E_u \propto \epsilon^{n-1} \tag{1.5}$$

where n is a soil parameter. This model is based on the assumption that the soil is elastic, perfectly plastic, and yields according to the Tresca yield crite-

ria. The value of E_u can vary with depth, but there is a value of strain below which the stiffness is taken to be constant. Gunn used this model to carry out finite element analysis for tunnelling in soil with parameters broadly representative of London Clay. He also performed analyses using linear elastic, and elastic-plastic soil models. Comparison of the settlement profiles obtained from the different models showed that the addition of non-linearity led to an improvement in the predicted settlement troughs, although the maximum settlements were only about 45% of the expected results, and the widths of the settlement troughs were too wide compared to those in practice. The different settlements obtained for the different models was caused by inconsistent material properties specified in Gunn's analyses. Chapter 3 examines the finite element analysis of tunnelling using the linear elastic model with identical soil parameters and tunnel configuration as Gunn's, but with a larger mesh. The analysis predicts heaving instead of settlements. This demonstrates the importance of boundary effects in finite element modelling. Although the results obtained by Gunn were not entirely satisfactory, his non-linear elastic-plastic model was an improvement on other linear elastic, elastic-plastic models.

1.5 Research Objective

The objective of the research described in this thesis is to establish an appropriate soil model for the prediction of the settlement profile due to the construction of a single shallow tunnel in soft ground. Since field observations have shown that a significant part of the total settlement occurs over a relatively short period during tunnel construction in clays, undrained conditions are investigated. Settlements at great distance from the tunnelling

face were considered, therefore plane strain was assumed. This reduced the problem to two dimensions. Both analytical and numerical methods were used to establish the surface settlement profiles. The soil parameters used in the analyses were those for London Clay. The dimension of the tunnel used in the analyses described in this thesis has a diameter of 5m (Fig. 1.5).

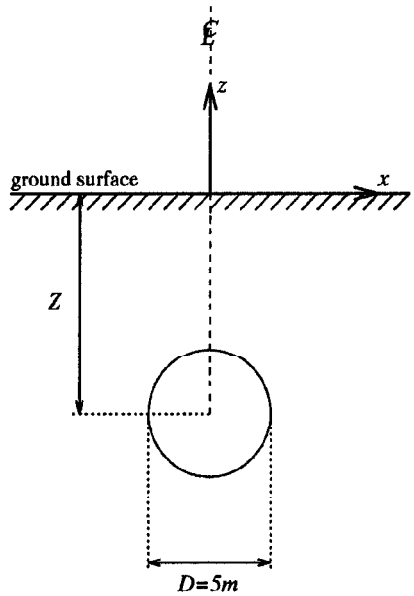

Figure 1.5: Dimensions of tunnel used in analyses of the thesis.

Two methods were used to obtain the closed form solutions for settlement profiles in shallow tunnelling. Each method modelled a different aspect of the mechanism causing the ground movements due to tunnel construction. The two methods were: (i) The elasticity solutions which modelled the uplift of soil due to the stress relief caused by the excavated material; (ii) The Sagaseta's method which modelled the component of settlement associated with the contraction of the tunnel.

Analyses using numerical methods were carried out using the finite element modelling program OXFEM. The method of simulating the tunnelling process was investigated, and the impact of rigid boundaries on computed results was explored. Two non-linear soil models were introduced to OXFEM. The constitutive equations for the models were derived to describe two (one each) different types of non-linearity of the soil: (i) the increase in stiffness with increasing stress level; (ii) the substantially higher stiffness offered by the soil under small strain deformations. Parametric studies were carried out on tunnelling using linear and non-linear models. Results from these analyses were compared with field results established by Peck (1969). The effectiveness of different models in the prediction of the width of settlement troughs was explored.

Chapter 2

CLOSED FORM SOLUTIONS

2.1 Introduction

The determination of surface settlements is an important aspect of the shallow tunnelling problem. The use of finite element methods for this purpose has been continually growing, and it has become the most efficient tool for this goal. However, there are many cases in which the available information about the soil properties is scarce and does not justify the use of a numerical method with a complex soil model. In other cases, a rapid approximation to settlement troughs are needed, and the use of the result of analytical methods becomes adequate. Analytical methods are also useful for checking numerical calculations and to conduct parametric studies.

To establish the appropriate closed form solution for surface settlements due to shallow tunnelling, the problem was approached using two different methods. For the first method, existing analytical solutions for the application of a point load in elastic half space were used in an attempt to produce solutions for line loading in elastic medium. The line loading represents the forces result after excavation took place in tunnelling. This method was developed in an attempt to model the uplift caused by the removal of soil from within the tunnel.

The second method was established by Sagaseta (1987). In his analysis of undrained soil deformation, he combined analytical results for elastic half space with a technique (with its origins in fluid mechanics) to produce closed form solutions for soil deformation due to ground loss. In this chapter these two methods will be discussed in detail.

2.2 Elasticity Solution

2.2.1 Introduction

Analytical solutions exist for a point load acting beneath the surface of an infinite elastic half space (Poulos and Davis, 1980), as in Mindlin's problem no.1 (Fig. 2.1). In this case, vertical movements at O can be expressed in terms of the load and material properties of the medium.

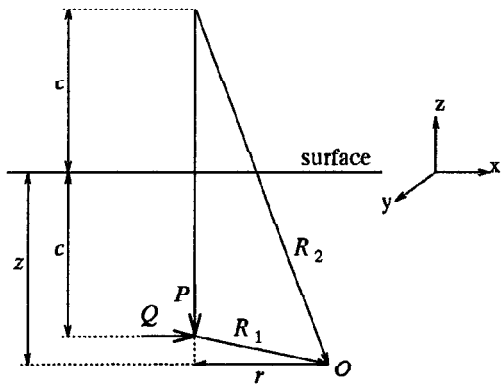

Figure 2.1: Mindlin's problem no. 1.

$$\delta_z = \frac{P}{16\pi G(1-\nu)}\left(\frac{3-4\nu}{R_1}+\frac{8(1-\nu)^2-(3-4\nu)}{R_2}+\frac{(z-c)^2}{R_1^3}+\frac{(3-4\nu)(z+c)^2-2c}{R_2^3}+\frac{6cz(z+c)^2}{R_2^5}\right) \quad (2.1)$$

where P and Q are vertical and horizontal point loads beneath the surface, $r = \sqrt{x^2 + y^2}$, $R_1 = \sqrt{r^2 + (z-c)^2}$, and $R_2 = \sqrt{r^2 + (z+c)^2}$.

2.2.2 Application to Shallow Tunnelling

In the prediction of settlement profiles due to shallow tunnelling, the effect of the tunnel face was ignored, and the tunnel was assumed to have infinite length. The line of application of the forces was taken as the position of the tunnel axis.

Consider Mindlin's problem no.1, the total vertical movements at point O (Fig. 2.2) will be the integral of equation 2.1 from $-\infty$ to $+\infty$ along the y-axis.

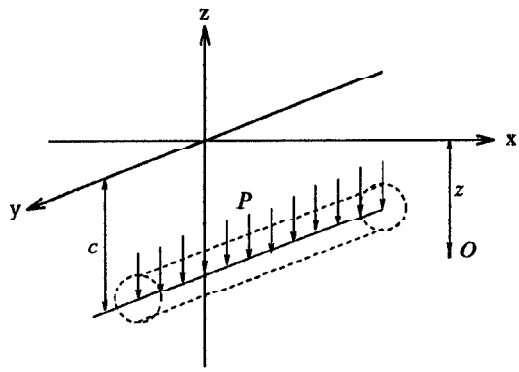

Figure 2.2: Application of Mindlin's problem no. 1 to tunnelling problem.

After integration of equation 2.1, we obtain

$$\begin{aligned}\delta_z = \frac{p}{16\pi G(1-\nu)}\Bigg(& (3-4\nu)\left[ln(y+\sqrt{x^2+y^2+(z-c)^2})\right]_{-\infty}^{+\infty} \\ & + \left[8(1-\nu)^2 - (3-4\nu)\right]\left[ln(y+\sqrt{x^2+y^2+(z+c)^2})\right]_{-\infty}^{+\infty} \\ & + \frac{2(z-c)^2}{x^2+(z-c)^2} + \frac{2(3-4\nu)(z+c)^2 - 4cz}{x^2+(z+c)^2} + \frac{8cz(z+c)^2}{\left[x^2+(z+c)^2\right]^2}\Bigg) \quad (2.2)\end{aligned}$$

where p is the force per unit length along the y-axis. It is assumed that

as $y \rightarrow \infty$, the definite integrals of the natural log functions with limits from $-\infty$ to $+\infty$ in equation 2.2 can be approximated by $[ln(y+|y|)]_{-\infty}^{+\infty}$. Therefore equation 2.2 becomes:

$$\delta_z \approx \frac{p}{16\pi G(1-\nu)}\left(8(1-\nu)^2\left[ln(y+|y|)\right]_{-\infty}^{+\infty} + \frac{2(z-c)^2}{x^2+(z-c)^2} + \frac{2(3-4\nu)(z+c)^2-4cz}{x^2+(z+c)^2} + \frac{8cz(z+c)^2}{[x^2+(z+c)^2]^2}\right) \quad (2.3)$$

Difficulty arises as the definite integral in equation 2.3 can not be evaluated analytically. Therefore exact values for the surface displacements can not be obtained. However, relative ground movements on the surface can be acquired by taking reference points at positions where vertical movements are comparitively small. Two cases are considered:

Case 1

By considering the displacement of the soil on the surface ($z = 0, x \neq 0$) relative to that at the line of symmetry at large depths below the surface ($z \rightarrow \infty, x = 0$). For $z = 0, x \neq 0$, equation 2.3 becomes:

$$\delta_{z=0,x\neq 0} = \frac{p}{2\pi G}\left((1-\nu)\left[ln(y+|y|\right]_{-\infty}^{+\infty} + \frac{c^2}{x^2+c^2}\right) \quad (2.4)$$

For $z \rightarrow \infty, x = 0$, equation 2.3 becomes:

$$\delta_{z\rightarrow\infty,x=0} \approx \frac{p}{2\pi G}\left((1-\nu)\left[ln(y+|y|\right]_{-\infty}^{+\infty} + 1\right) \quad (2.5)$$

Therefore the relative displacement can be obtained by subtracting equation 2.5 from 2.4:

$$\begin{aligned}\delta_{z=0,x\neq 0} - \delta_{z\rightarrow\infty,x=0} &= \frac{p}{2\pi G}\left(\frac{c^2}{x^2+c^2} - 1\right) \\ &= -\frac{px^2}{2\pi G(x^2+c^2)}\end{aligned} \quad (2.6)$$

Case 2

By considering the displacement of the soil on the surface ($z = 0, x \neq 0$) relative to that at large distances from the tunnel ($z \to \infty, x \neq 0$). For $z = 0, x \neq 0$, the expression for the vertical displacements of soil is the same as equation 2.4 in Case 1. For $z \to \infty, x \neq 0$, equation 2.3 becomes:

$$\delta_{z\to\infty,x\neq 0} \approx \frac{p}{2\pi G}\Big((1-\nu)\,[ln(y+|y|]_{-\infty}^{+\infty}+1\Big) \tag{2.7}$$

The relative displacement can be obtained by subtracting equation 2.7 from 2.4:

$$\begin{aligned}\delta_{z=0,x\neq 0} - \delta_{z\to\infty,x=0} &= \frac{p}{2\pi G}\Big(\frac{c^2}{x^2+c^2}-1\Big)\\ &= -\frac{px^2}{2\pi G(x^2+c^2)}\end{aligned} \tag{2.8}$$

Both cases give the same expression for surface displacements for soil due to a line loading below the ground surface. However, equation 2.6 (or 2.8) gives zero displacement at the line of symmetry of the tunnel. Surface displacements at $x \neq 0$ are expressed relative to the value at $x = 0$. Since movements of soil at large distances from the tunnel are small relative to the the original ground level, it is more useful to express the vertical displacements of soil relative to those at large horizontal distances from the tunnel axis. As $x \to \infty$, equation 2.6 (or 2.8) becomes:

$$\delta_z \approx \frac{p}{2\pi G} \tag{2.9}$$

The relative surface displacements can then be obtained by subtracting equation equation 2.6 (or 2.8) from equation 2.9:

$$\delta_z = \frac{pc^2}{2\pi G(x^2+c^2)} \tag{2.10}$$

In the case of tunnelling, the value of p can be represented by the weight of the excavated soil. In the two dimensional case, $p = -\frac{\pi\gamma D^2}{4}$ per unit length of the tunnel. The pressure acting on the soil is assumed to be concentrated at the tunnel axis, and replacing the value of c by the depth of the tunnel axis, Z, we obtain:

$$\delta_z = -\frac{\gamma D^2 Z^2}{8G(x^2 + Z^2)} \tag{2.11}$$

The settlement profiles obtained using equation 2.11 for a value of Z=10m, G=33557kPa and γ=20kPa per unit length of the tunnel is shown in Fig. 2.3.

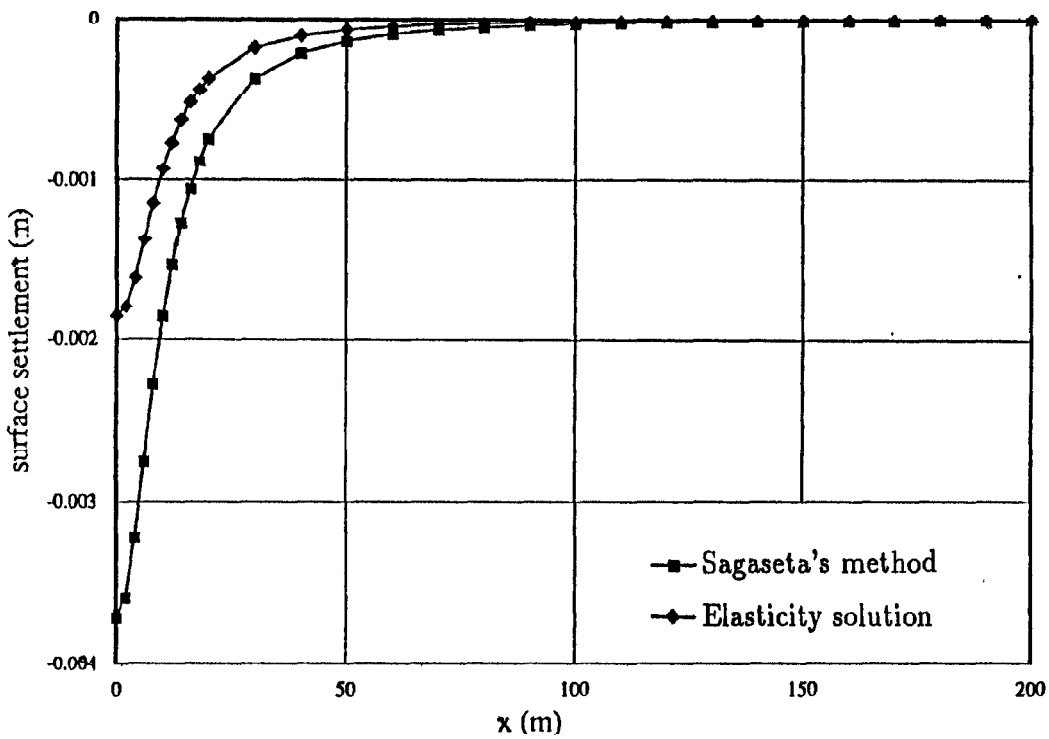

Figure 2.3: Surface settlement profiles obtained from closed form solutions.

2.2.3 The elasticity solution for the prediction of settlement profiles in tunnelling

Examination of the settlement profile given by equation 2.11 shows that the point of inflection, i, occurs at $x = \frac{Z}{\sqrt{3}} (\approx 0.5774Z)$. The corresponding surface displacement, δ_i, is equal to $0.75\delta_{max}$. This result can be compared with the empirical representation of the settlement trough by the error function curve established by Peck (1969). One property of the error function curve is that the point of inflection occurs at $\delta_i = 0.61\delta_{max}$. For the analytical elasticity solution, $\delta_z = 0.61\delta_{max}$ when $x = 0.78Z$, giving a narrower settlement trough than field observations as investigated by Peck.

2.3 Sagaseta's Method

2.3.1 Introduction

The governing equations of any stress-strain problem are

1. Equilibrium conditions
2. Constitutive equations
3. Compatibility equations
4. Boundary conditions.

The equilibrium equations are in terms of stresses only, while the constitutive law includes both stresses and strains. Sagaseta (1987) suggested that in problems where the boundary conditions are only in terms of displacements, and only displacements are required for the solution, it is possible to eliminate the stresses from the governing equations and work in terms of strains for simple soil models. An example of this type of problem is the

determination of the displacement field in an isotropic homogeneous incompressible soil when some material is extracted from it at shallow depth, and the surrounding soil completely fills the void left by the extraction. Shallow tunnelling in elastic homogeneous material can be regarded as this type of problem, where the extracted material is defined by the ground loss.

The advantage of Sagaseta's method is that the strain field obtained is independent of the soil stiffness, and is valid for any incompressible material, even for a fluid. As a result, some commonly used principles of fluid mechanics, such as the superposition of elementary cases, can also be applied to soil mechanics. By combining analytical results for an elastic half-space with a technique originated from fluid mechanics, Sagaseta showed that closed form solutions for soil deformation due to ground loss (such as in tunnel excavation) can be obtained.

The analysis is first performed ignoring the effect of the ground surface and assuming that the soil is an infinite medium. The effect of the free surface is introduced at a later stage using a procedure based on a virtual image technique and solutions for the elastic half-space. However, the effect of stress relief caused by the removal of excavated material is not included.

2.3.2 Application of Sagaseta's Method to Tunnelling Problems

Removal of soil during tunnelling is modelled as a point sink which extracts a finite volume of soil at some depth Z below the top surface (Fig. 2.4(a)). The extracted soil has a volume per unit length of v in plane strain, and is assumed to be distributed over the tunnel periphery. As a first approxima-

tion, the ground loss can be concentrated at the axis. The analysis is then carried out using the following steps:

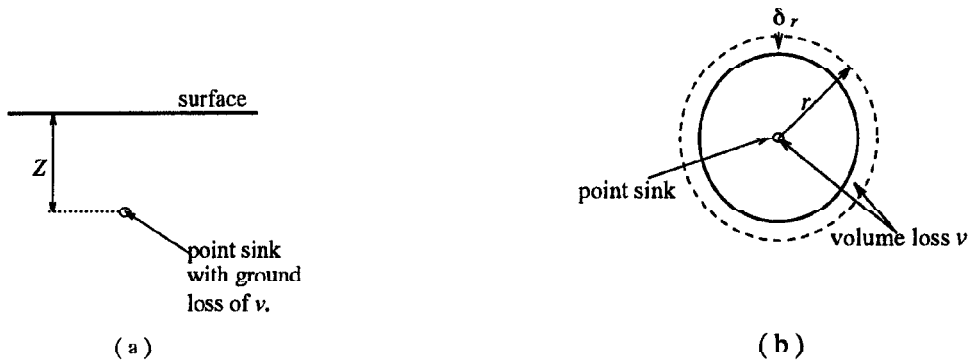

Figure 2.4: (a) Using a point sink to model ground loss. (b) Movement of soil due to a point sink in an infinite medium.

Step 1

Ignoring the topsoil surface, the problem is symmetrical about the sink (ie. the tunnel axis), and the displacement of any point is purely radial. Assuming the soil to be incompressible and the ground loss defined by a radius a of an equivalent cylinder (Fig. 2.4), then

$$v = \pi a^2 = 2\pi r \delta_r \tag{2.12}$$

in the plane strain condition. Therefore the displacement at a distance r from the sink has an inward radial displacement of

$$\delta_r = \frac{a^2}{2r} \tag{2.13}$$

The derivation of equation 2.13 assumed small displacements and neglects any change in geometry of the soil sample. In Cartesian coordinates, the expression for vertical displacement on the surface can be expressed as:

$$\delta_z = \frac{a^2 Z}{2(x^2 + Z^2)} \tag{2.14}$$

Step 2

The displacement in the above equation produces a stress field in the medium. Using a negative image (a virtual source) with respect to the top surface produces opposite normal stresses and the same horizontal stresses as the actual sink. Therefore the surface normal stresses are eliminated. However, the displacement is totally constrained in the horizontal direction. This is similar to having the soil surface covered by an inextensible membrane that is flexible in bending, and matches closely real soil.

Step 3

Taking the soil to be incompressible (Poisson's ratio of 0.5), the application of a horizontal load at the soil surface (Boussinesq's problem) produces zero vertical movements at the surface. Therefore the remaining surface shear stresses will cause no additional vertical movement and the vertical surface displacements due to the ground loss are given by the sum of the displacements caused by the sink and its negative image

$$\delta_z = \frac{a^2 Z}{x^2 + Z^2} \tag{2.15}$$

In terms of the ground loss v, the surface settlements can be written as

$$\delta_z - \frac{vZ}{\pi(x^2 + Z^2)} \tag{2.16}$$

To calculate the value of v, the forces acting on the tunnel due to the weight of soil above the tunnel axis are considered. At a depth Z below the ground level, the weight acting vertically on the tunnel axis is γZ. Since the material is assumed to be elastic homogeneous, and loading is assumed to be isotropic,

the change in the radius of the tunnel can be expressed as

$$\frac{\delta_R}{R} = -\frac{\gamma Z}{2G} \tag{2.17}$$

where R is the radius of the tunnel. From equation 2.12, the radial movement at the periphery of the tunnel can be obtained by replacing r by the radius of the tunnel. Substituting equation 2.17 into the expression for v (equation 2.12) we obtain:

$$v = -\frac{\pi\gamma R^2 Z}{G} \tag{2.18}$$

Using equation 2.18 with equation 2.16 gives an expression for the surface settlements:

$$\delta_z = -\frac{\gamma R^2 Z^2}{G(x^2+Z^2)} = -\frac{\gamma D^2 Z^2}{4G(x^2+Z^2)} \tag{2.19}$$

The settlement profile obtained using Sagaseta's method for Z=10m, G=33557kPa and γ =20kPa per unit length of the tunnel is shown in Fig. 2.3.

2.3.3 Correction for Rigid Boundaries

The results obtained by Sagaseta's method are valid for an infinite elastic half space. In real cases, the presence of a rigid base would affect the amount of soil movement. In this section, the consequence of rigid boundaries on surface settlements is discussed.

The boundary conditions at a smooth rigid wall are zero shear stress and zero normal displacement. This can be modelled by adding a positive image to the sink. However, if the boundary is rough, the displacement parallel to the wall is also constrained and modelling is more complex. A method similar to the surface stress relief method would be necessary.

The joint action of a rigid boundary and a free surface results in multiple reflections. For example, a rigid base produces a doubly infinite series of reflections (Fig. 2.5). It is then necessary to superimpose an infinite number of virtual sinks and sources.

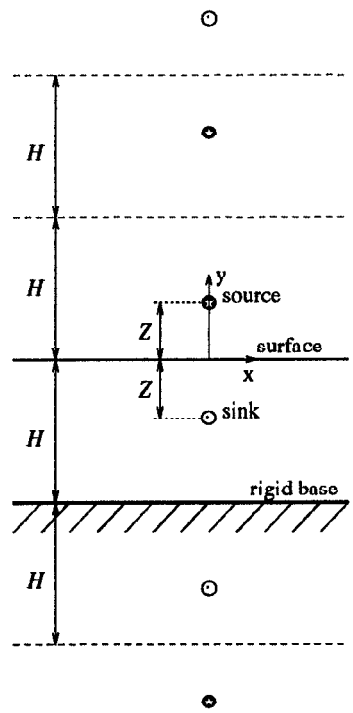

Figure 2.5: Correction for rigid boundaries using multiple reflections.

However, for simplicity in the derivation of the analytical solutions, only two cases were considered: reflections at $\pm H$; and at $\pm H$ and $\pm 3H$, where H is the depth of the rigid base below the ground level. Two values of H were used: 30m and 110m. Their results were compared in order to find the number of reflections required for a realistic simulation of a rigid boundary. The difference between settlements for the two cases for each value of H were found to be extremely small. Solutions for surface settlements in this

tunnelling problem using Sagaseta's method are therefore seen to converge rapidly when the effect of a rigid base is included.

2.3.4 Sagaseta's method for the prediction of settlement profiles in tunnelling

Equation 2.19 provides a closed form solution for the surface settlement profile due to a single shallow tunnel in a elastic homogeneous medium. The point of inflection, i, occurs at $x = \frac{z}{\sqrt{3}}$, giving a corresponding displacement of $0.75\delta_{max}$. Thus, Sagaseta's method produces narrower settlement trough than Peck's empirical results.

2.4 Comparison of Closed Form Solutions

The tunnelling analysis using the elasticity closed form solution modelled the uplift caused by the removal of soil from within the tunnel. It did not account for the component of settlement associated with the contraction of the tunnel. However, analysis using Sagaseta's method modelled the deformations of soil due to the ground loss in excavation. The effect of stress relief caused by the removal of soil was not accounted for. It can been seen from the settlement profiles that the effect of stress relief caused by the removal of material in an elastic homogeneous medium produces less disturbance on the surface than the effect due to the ground loss of the excavation. Settlements obtained using elasticity solutions are half that for Sagaseta's method. Both methods gave the same width of predicted settlement troughs, being narrower than that for an error function curve.

Closed form solutions are only valid for isotropic homogeneous material

and do not allow for non-linear behaviour. However as a first approximation of the effect due to shallow tunnelling, both methods described in this chapter can give a reasonable estimate of the width of the surface trough.

Chapter 3

FINITE ELEMENT MODELLING

3.1 Introduction

In this chapter, the method of finite element modelling using program OXFEM is examined. The first part of the chapter reviews some aspects of OXFEM. Particular emphasis is placed on the incorporation of constitutive laws and their corresponding stress updating procedures. This is important for the introduction of two non-linear soil models to the existing program as discussed in Chapter 5 and 6. The problem with shallow tunnelling using finite element modelling will be discussed in the second part of this chapter.

3.2 Finite Element Analysis with OXFEM

The basic formulation used in OXFEM was discussed by Burd (1986). Burd originally designed the program to carry out large displacement analyses. It was then modified to perform small strains calculations. The structure of OXFEM is shown in Fig. 3.1.

The mesh can be generated using the program OXMESH. OXMESH can

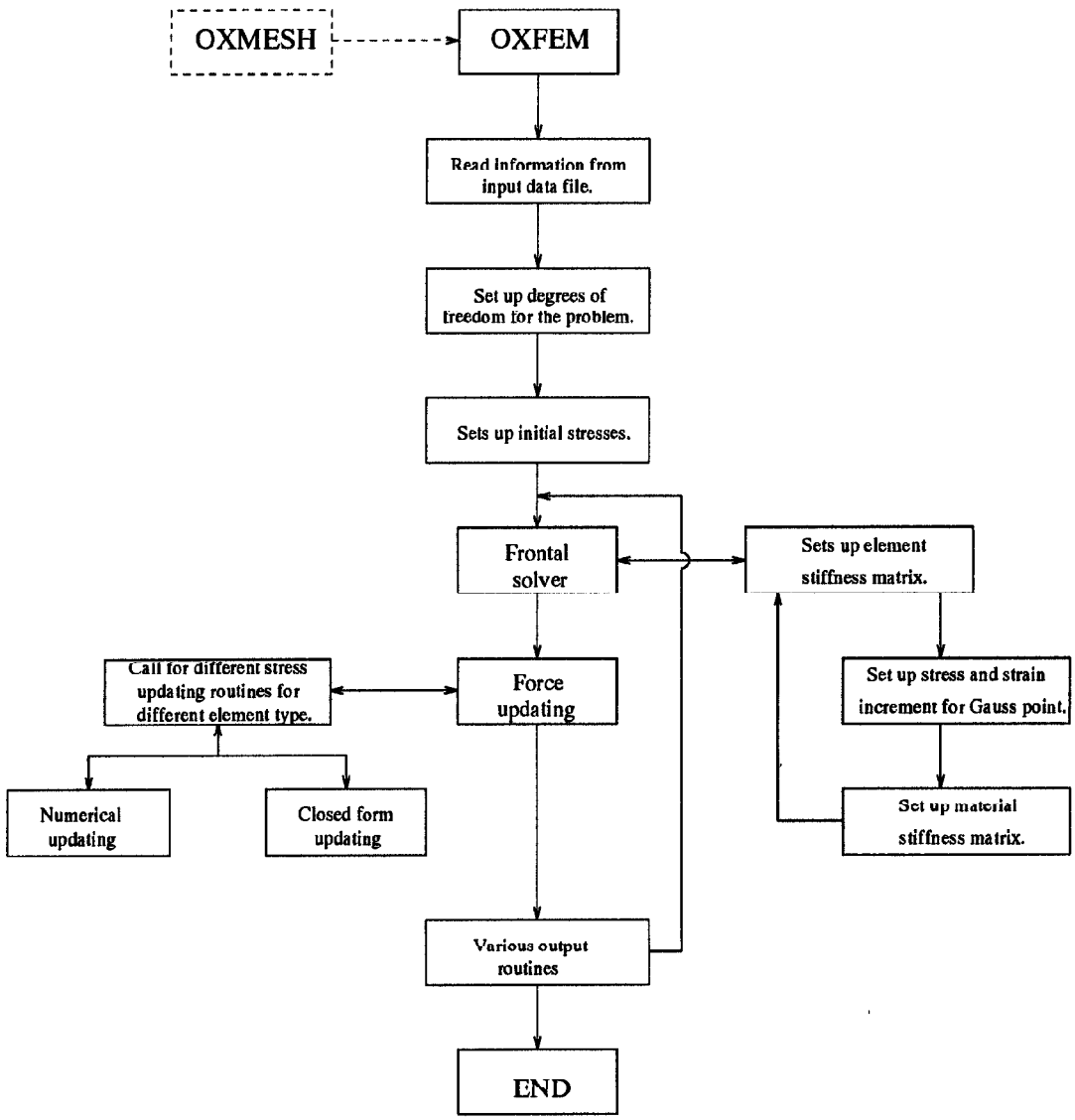

Figure 3.1: Basic structure of program OXFEM.

produce finite element meshes for triangular two-dimensional elements and is able to write an output file of the mesh created in the input format for OXFEM. The input file for OXFEM contains this information, as well as material properties of each element in the mesh and its boundary conditions. OXFEM is then used to calculate values of the primary variables at discrete times during loading. The modified Euler scheme is used to obtain all of the finite element solutions.

3.2.1 Solution Scheme

This section describes the modified Euler scheme used in OXFEM in obtaining solutions (Fig. 3.2). At the start of each load step, the individual

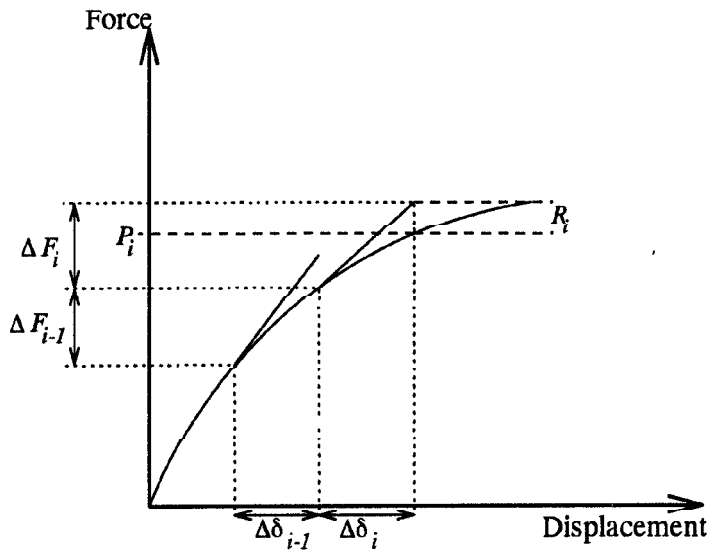

Figure 3.2: Solution scheme for OXFEM.

element stiffness matrices are calculated, and then assembled and inverted using a Frontal solution algorithm to give a set of incremental nodal displacements $\Delta\delta_i$. Stress increments $\Delta\sigma$ at each Gauss point corresponding to the

incremental nodal displacements $\Delta\delta_i$ are then calculated. This is done by performing the operation:

$$\boldsymbol{\Delta\sigma} = \int_t^{t+\Delta t} \boldsymbol{D}\dot{\epsilon}dt \tag{3.1}$$

where $\boldsymbol{D}$ is the material stiffness matrix relating stress rate to strain rate, and $\dot{\epsilon}$ is a strain rate vector which, when integrated over the time step, is compatible with the incremental nodal displacement $\Delta\delta_i$. The increment begins at time t, and ends at time $t + \Delta t$. In general, a numerical integration scheme must be used to evaluate equation 3.1, but in some cases a closed form solution can be obtained and this is preferable. The final step in the solution scheme is to calculate nodal loads consistent with the stresses at the updated geometry (P_i of Fig. 3.2). A set of unbalanced nodal loads are then calculated (R_i in Fig. 3.2) and then applied as an equilibrium correction during the next load increment.

3.2.2 Material stiffness matrix and stress updating

Formulation of the element stiffness matrix is based on infinitesimal theory. The stress-strain relationship for an elastic material may be written as:

$$\dot{\boldsymbol{\sigma}} = \boldsymbol{D}\dot{\epsilon} \tag{3.2}$$

where $\boldsymbol{D}$ is the material stiffness matrix. The strain rate vector is related to the nodal displacements $\dot{\boldsymbol{U}}$ by equation 3.3:

$$\dot{\epsilon} = \boldsymbol{B}\dot{\boldsymbol{U}} \tag{3.3}$$

where $\boldsymbol{B}$ is obtained by appropriate differentiation of the shape function of the element. The element stiffness matrix is derived using the virtual work principle:

$$\dot{\boldsymbol{U}}^*\dot{\boldsymbol{P}} = \int \dot{\epsilon}^*\dot{\boldsymbol{\sigma}}dv \tag{3.4}$$

$\dot{\epsilon}^*$ is the vector of strains compatible with the virtual nodal displacements, $\dot{U}^*$, and $\dot{\sigma}$ is the vector of stresses in equilibrium with the nodal forces $\dot{P}$. The integration is taken over the whole of the volume of the element. From equation 3.2 and 3.3, we obtain:

$$\dot{\sigma} = D\dot{\epsilon} = DB\dot{U} \tag{3.5}$$

and

$$\dot{\epsilon}^{*T} = \dot{U}^{*T}B^T \tag{3.6}$$

Sunstituting equations 3.5 and 3.6 into equation 3.4 gives:

$$\dot{U}^{*T}\dot{P} = \int \dot{U}^{*T}B^T DB\dot{U}dv \tag{3.7}$$

Since the virtual displacements are arbitrary, the element stiffness K which relates the nodal forces and nodal displacements is given by:

$$K = \int B^T DBdv \tag{3.8}$$

From equation 3.8, it can be seen that in order to set up the element stiffness matrix, it is necessary to derive the material stiffness matrix, D, which relates the vectors of stresses to strains. Therefore constitutive laws which describe the material behaviour are required to evaluate the material stiffness. The existing OXFEM program contains various linear-elastic perfectly-plastic soil types. Derivation of all constitutive laws of those models is on the basis that elastic moduli remain constant during the deformation. At each iteration, the material stiffness matrix for the element is set up, giving the stress-strain relationship of the material at the current stress state.

At the end of each calculation increment, OXFEM performs an equilibrium check. This requires that the stresses at each Gauss point be updated

by evaluating an integral of the form given in equation 3.1.

Three operations, in general, are needed to calculate the updated Gauss point stresses.

1. It is necessary to calculate the strain rate $\dot{\epsilon}$ which, when integrated over the time step, is compatible with the incremental displacements.
2. The incremental Gauss point stresses are obtained by integrating the constitutive equations. In some cases, updated stresses may be obtained from a closed form solution.
3. The stresses are converted back to the yield surface if a numerical scheme has been used to integrate the constitutive law.

The setting of the material stiffness matrix and stress updating procedures are particularly important in the introduction of new soil types to OXFEM.

3.3 Method of Simulating Tunnelling Process

In this section, simulation of the tunnelling process using finite element analysis is examined, as well as the effect of mesh size. OXMESH was used to create the mesh. Symmetry is assumed along the tunnel axis, and the vertical boundaries of the mesh are free of vertical traction, while the base of the mesh is pinned (Fig. 3.3). The element size of the mesh increases with increasing distance from the tunnel.

An appropriate way to represent the tunnelling process is required for analysis with OXFEM. The tunnels are considered unsupported in the analysis, and the effect of lining is not modelled. Two different methods were

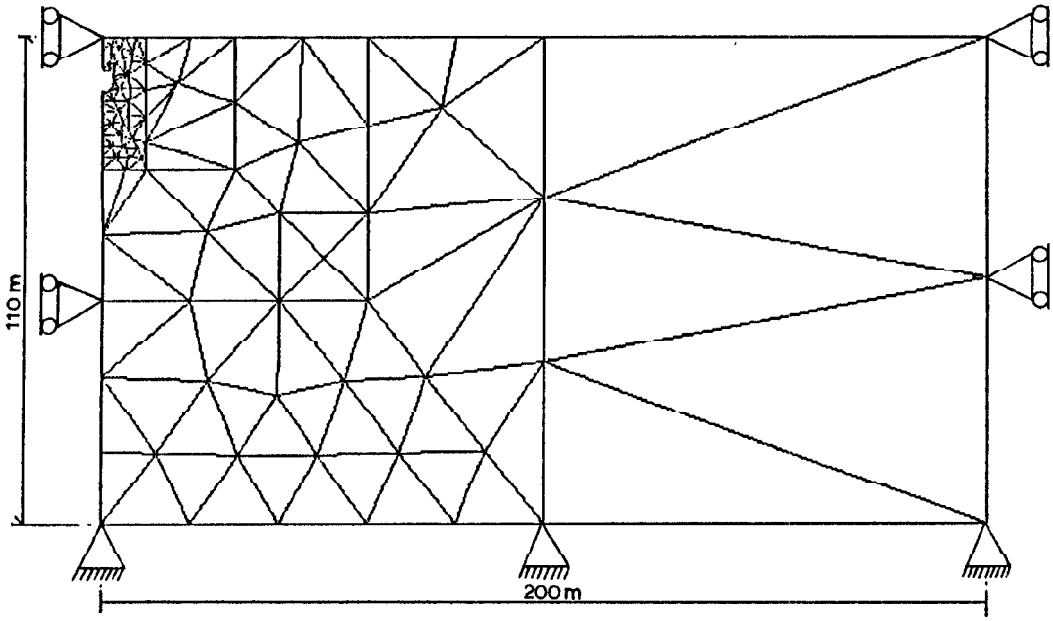

Figure 3.3: Boundary conditions and dimensions for the mesh used in finite element modelling of tunnel analysis.

used. Their results were compared and the more suitable one was used for parametric studies of tunnelling with OXFEM. The two methods used were:

1. Application of uniform radial displacements around the periphery of the tunnel to represent the movement of soil due to excavation.
2. Application of nodal forces around the periphery of the tunnel to represent the reduction in soil pressure due to the removal of soil.

Elastic homogeneous material was used. The properties of the material represent closely that of London clay, and were taken from Gunn (1993). Since the effect of advancing the tunnel at the face is not considered in this thesis, a plane strain model was assumed.

3.3.1 Application of uniform radial displacement

The movement of soil around the periphery of the tunnel was assumed to be radially inwards. The magnitude of displacements are the same for each node. These values were calculated by modelling the tunnel as a thick cylinder acted on by the pressure due to the weight of soil around the tunnel. Elastic solutions were used to find the resulting displacement. Two standard solutions were used

$$\sigma_r = A + \frac{B}{r^2} \tag{3.9}$$

$$\sigma_\theta = A - \frac{B}{r^2} \tag{3.10}$$

where A and B are arbitrary constants. A and B were found by applying the boundary conditions that as $r \rightarrow \infty, \sigma_r = 0, \sigma_\theta = 0$. Thus the radial displacement, δ_r, around the tunnel can be written as

$$\delta_r = \frac{-P(1+\nu)R^2}{Er} = -\frac{PD^2}{8Gr} \tag{3.11}$$

where P is the pressure acting on the tunnel. At the periphery of the tunnel, the radial movement is:

$$\delta_R = -\frac{PD}{4G} \tag{3.12}$$

Isotropic pressures were assumed, and K_0 was equal to unity so that the pressure was uniform. This analysis is only valid for isotropic initial stresses, and P had the value of γZ. Equation 3.12 becomes:

$$\delta_R = -\frac{\gamma DZ}{4G} \tag{3.13}$$

and this value of radial displacement is prescribed for nodes around the periphery of the tunnel. The settlement profiles obtained using this method for Z=10m, G=33557kPa, and γ =20kPa, are shown in Fig. 3.4.

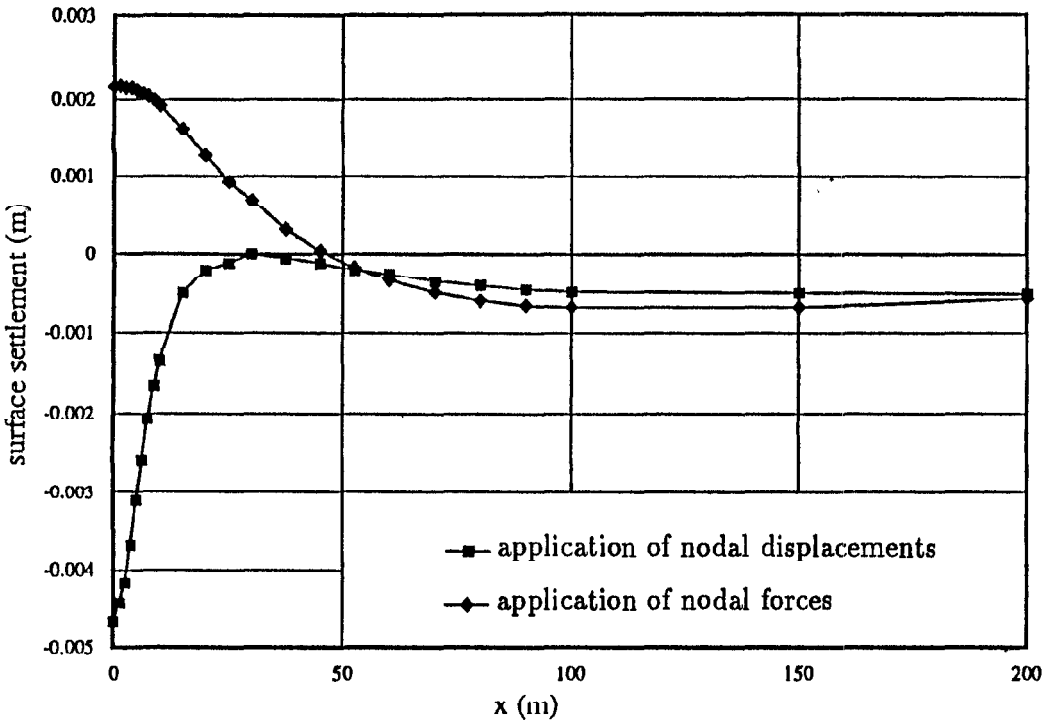

Figure 3.4: Surface displacements from OXFEM for tunnelling using two different methods for the simulation of tunnelling process.

A disadvantage of this method is that the nodal displacements of soil at the periphery of the tunnel are fixed. Arching is not taken into consideration. Deformation of the tunnel was assumed radially uniform, and the deformed shape remained circular. However, in a real situation the deformed tunnel may not retain its circular shape, and displacements around the tunnel are not uniform.

3.3.2 Application of nodal forces

Another method used to represent the absence of supporting pressure due to the excavation process was the application of nodal forces to the tunnel. This was achieved as follows:

1. The nodes around the periphery of the tunnel were identified from OXMESH.
2. OXFEM was run without any prescribed nodal displacements or forces, except the self weight of the soil. The force vectors acting at the nodes (from 1) due to in-situ stresses before excavation were found.
3. The nodal forces determined in 2 were applied in the opposite direction.

The surface displacements obtained using the method of application of nodal forces, with the same soil properties as that for the method with the application of nodal displacements, are superimposed on Fig. 3.4. The results for an elastic homogeneous material show heaving. This is mainly due to the stress relief mechanism. As with the uniform radial displacement method (section 3.3.1), the value of K_0 was taken to be unity. Thus no shear stresses were acting on the periphery of the tunnel and only normal radial nodal forces were present.

Gunn (1993) performed finite element analysis of tunnelling in elastic homogeneous material with the same soil properties, tunnel dimensions, and modelling method for tunnel construction as those used for the analysis described in this section. However, Gunn used a different mesh size which is shown in Fig. 3.5.

Instead of the heaving obtained using OXFEM, Gunn's analysis predicted settlements. It is because the mesh size used by Gunn was not large enough which restrained the surface movement of the soil.

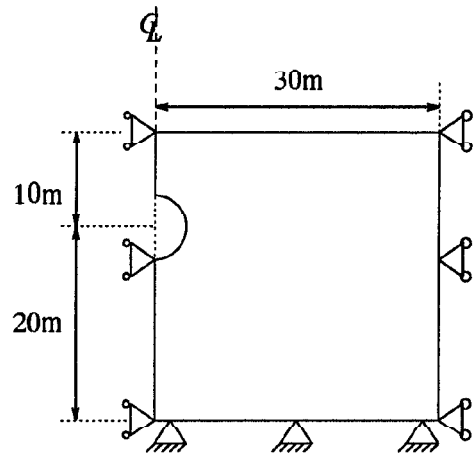

Figure 3.5: Size of mesh used in Gunn's finite element analysis on tunnelling.

3.4 Effect of Mesh Size

Section 3.3.2 showed that finite element analysis is greatly affected by the boundary conditions applied to the mesh. Therefore, before parametric studies on different soil models were carried out, analyses on three different mesh sizes were performed in order to find the best combination of accuracy of results and computation time. The three meshes are shown in Fig. 3.6.

Oteo & Sagaseta (1982) investigated effects introduced artificially to finite element analysis of tunnelling problem. They found that the bottom rigid base had the most significant effect on the predicted settlements. When the depth of the rigid base below the tunnel axis, H_D, increases, the settlements decreases, resulting in surface heave for a value of $\frac{H_D}{D} > 7$. The three different mesh sizes used in this analysis covered depths of rigid base from 30m to 110m. At the same time, the lateral boundaries were increased accordingly.

Results obtained from OXFEM using the method of applying nodal forces

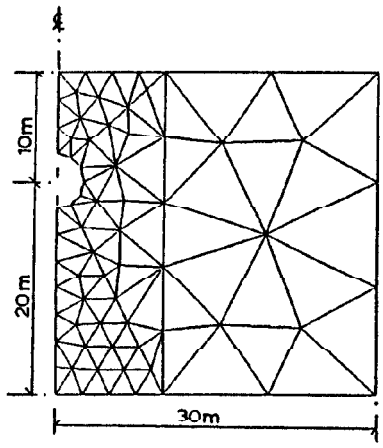

Mesh (a)

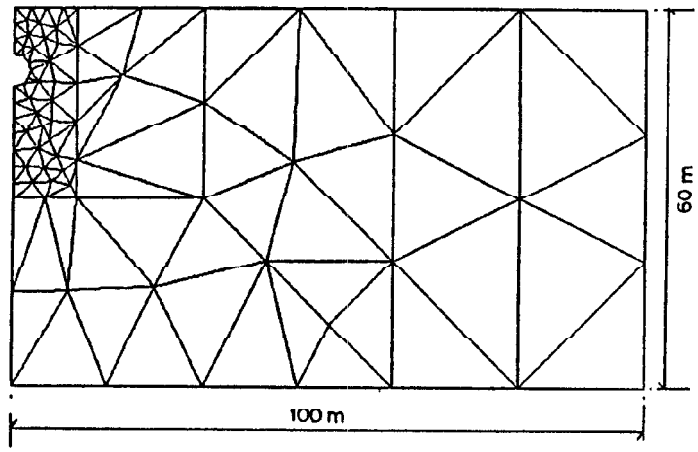

Mesh (b)

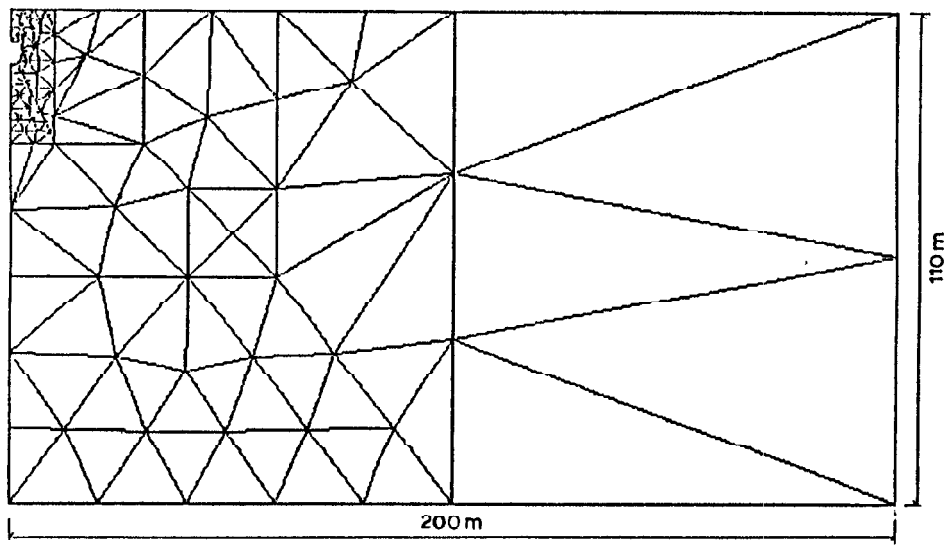

Mesh (c)

Figure 3.6: Meshes used in the investigation of the effect of boundary conditions in tunnelling problem.

for tunnels at Z=10m are shown in Fig. 3.7. A value of G=33557kPa, and γ=20kPa were used. When using the smallest mesh (Fig. 3.4(a)), settlements were obtained. However, heaves were found from analyses using meshes (b) and (c). This is because the smaller the mesh, the more profound is the effect of the fixed boundary. As the nodes at the rigid base are restricted in vertical and horizontal movements, the movement of soil on the surface is restrained as well.

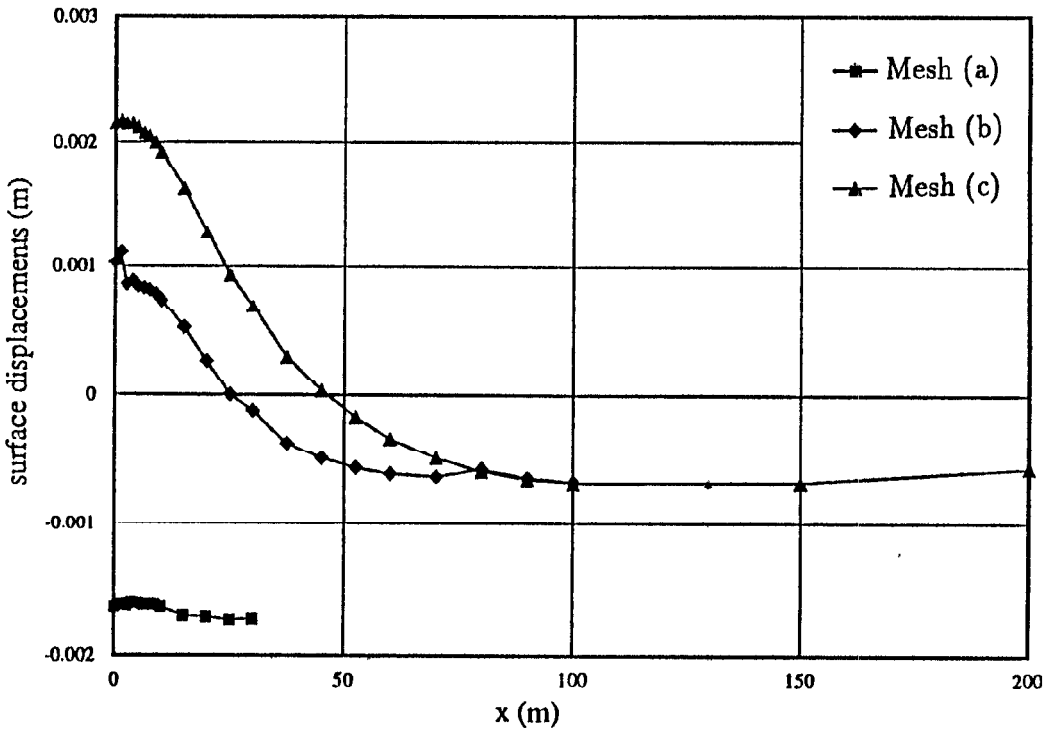

Figure 3.7: Surface displacements from OXFEM for tunnelling using the method of application of nodal forces for three different mesh size.

Although using a larger mesh size in finite element analysis reduces the effect of the fixed boundary, computation time increases with the increase in number of elements in the mesh. Mesh (c) shown in Fig. 3.6 was considered to be large enough that the fixed boundary effect was comparitively small and was used in all parametric studies discussed in this thesis.

3.5 Comparison of the Two Simulation Methods

Before a choice of simulation method of the tunnelling process can be made, the basic mechanisms which cause soil movements when excavation takes place have to be understood.

There are two main causes of surface movements of soil due to tunnelling: stress relief; and the subsidence due to the removal of support due to excavation. The stress relief mechanism causes an upward movement of soil. This is because when soil is removed from the ground, there is a global reduction in soil weight. The second mechanism causes downward movements due to the lack of support after the excavation. Computed soil profiles will be a combination of these two effects.

Using the uniform radial displacement method (section 3.3.1) the amount of displacement of soil at the periphery of the tunnel is fixed. As a result, surface settlements were recorded with OXFEM. However, with the application of radial nodal forces, displacements are only fixed at the mesh boundary (except the tunnel periphery), and both mechanisms governing the ground movements are taken into account. Heaves are obtained except for the most highly constrained mesh. For elastic, homogeneous soil, stiffness is constant throughout the medium and the sudden absence of soil produces heaving.

In the light of this comparison, the method using the application of nodal forces was chosen and used in all finite element analyses discussed in the rest of this thesis.

Chapter 4

LINEAR ELASTIC AND ELASTIC-PLASTIC CLAY

4.1 Introduction

This chapter presents the OXFEM analyses of surface settlements due to shallow tunnelling for various linear soil models. The analyses are divided into two catagories: elastic, and elastic-plastic. For each catagory, parametric studies were carried out for (i) homogeneous soil, and (ii) soil with properties which vary with depth. For each soil model, an analysis was made for each of three values of Z, the depth below the surface of the tunnel axis. Values of Z of 7.5m, 10m, 15m were used.

4.2 Choice of Soil Parameters in Parametric Studies of Tunnelling

For undrained conditions the volumetric strain is zero. It follows that the value of the undrained bulk modulus must be infinite, and Poisson's ratio equal to 0.5. However, in finite element analyses it is not possible to use an infinite undrained bulk modulus. To approximate undrained conditions, a value of Poisson's ratio of 0.49 was used. The self weight of soil, γ, was taken

as 20kPa per unit length in the y-direction, and earth pressure coefficient at rest, K_0, was unity.

The material properties used are those chosen by Gunn (1993) to be broadly representative of London clay. The shear stiffness profile for each analysis follows the equation (Fig. 4.1):

$$G(z) = G_0 + mz \tag{4.1}$$

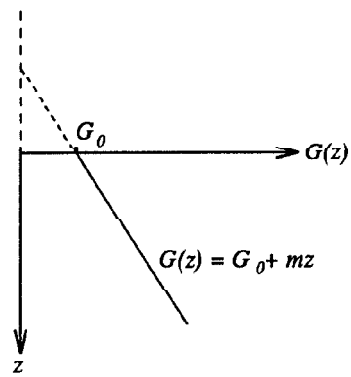

Figure 4.1: Variation of shear modulus.

where G_0 is the shear stiffness at the surface of the soil and m is the rate of increase of the stiffness with depth. The value of G at a depth of 10m is 33557kPa and is kept constant for all the analyses.

A large value of undrained shear strength was assumed in the analyses with elastic models to ensure yielding did not occur in any part of the mesh. For elastic, perfectly-plastic models, the choice of the undrained shear strength at the tunnel axis, s_u, were made with reference to the results on the stability of tunnel established by Davis *et al* (1980).

Davis *et al.* estimated the stability of tunnels in soft clay by means of lower and upper bound plasticity solutions. In their analyses, the soil was idealized as an elastic-perfectly plastic material. According to the limit theory of plasticity, the collapse load for a particular configuration of loading on a perfectly plastic body is unique, ie. the load carrying capacity of the body cannot be changed by applying various loads in a different order. The lower bound theorem states that if any stress field can be found which supports the loads, and is everywhere in equilibrium without yielding, then the loads are lower than (or equal to) those for collapse. The upper bound theorem states that if a work calculation is performed for a kinematically admissible collapse mechanism then the loads thus deduced will be higher than (or equal to) those for collapse. Davis *et al.* defined a stability ratio N in accordance with that defined by Broms and Bennermark (1967) which is equal to the difference between the total vertical stress in the ground at the axis of the tunnel (before the tunnel is constructed) and the tunnel pressure, σ_t, divided by the undrained shear strength s_u (Fig. 4.2):

$$N = \frac{\sigma_s - \sigma_t + \gamma(C + \frac{D}{2})}{s_u} \tag{4.2}$$

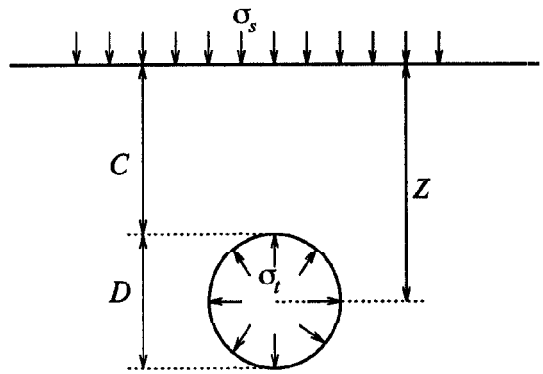

Figure 4.2: Tunnel with overburden stresses and internal pressure.

The relationship between the stability ratio N and the dimensionless groups $\frac{C}{D}$ and $\frac{\gamma D}{s_u}$ was established by Davis *et al.* using the lower and upper bound theorems. Their results are shown in Fig. 4.3.

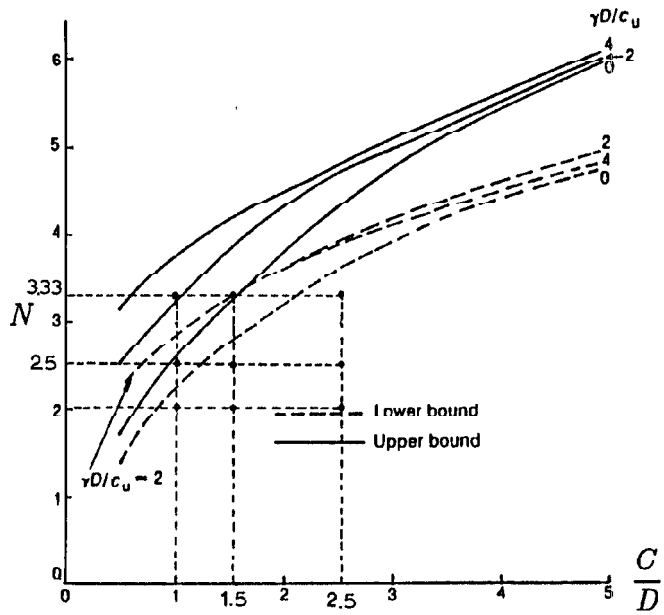

Figure 4.3: Upper and lower bound stability ratios for plane strain circular tunnels (after Davis *et al*, 1980), with the grid used to determine the value of s_u, superimposed.

In order to find a suitable range of values of s_u to be used in OXFEM in the analysis of elastic-perfectly plastic soil, the lower bound results of Davis *et al.* were referenced. Overburden stresses and internal tunnel pressures were not considered, so $\sigma_o = \sigma_i = 0$. Thus equation 4.2 becomes:

$$N = \frac{\gamma Z}{s_u} \tag{4.3}$$

where $Z = C + \frac{D}{2}$.

Simple dimensional analysis shows that the width of settlement trough, i, and the maximum displacement δ_{max} can be related to a number of dimensionless groups:

$$\frac{i}{D} = f\left(\frac{Z}{D}, \frac{s_u}{\gamma Z}\right) \tag{4.4}$$

$$\frac{\delta_{max} G}{\gamma D^2} = g\left(\frac{Z}{D}, \frac{s_u}{\gamma Z}\right) \tag{4.5}$$

As a result, it is convenient to approach the analysis in terms of the independent parameter $\frac{s_u}{\gamma Z}$, which is the inverse of the stablilty ratio expressed in equation 4.3. The lower bound theorem provides a safe estimate of the pressure required to maintain stability. Three values of $\frac{s_u}{\gamma Z}$ for the use in the parametric studies were chosen to cover the range of the results obtained from the theorem for the three depths of the tunnel axis (Fig. 4.4). The values of $\frac{s_u}{\gamma Z}$ and their corresponding s_u for each $\frac{Z}{D}$ is shown in Table 4.1. For soil with increasing undrained strength with depth, the value of s_u at the depth of the tunnel axis was set equal to that in Table 4.1.

N	3.33			2.5			2.0		
$\frac{s_u}{\gamma Z}$	0.3			0.4			0.5		
$\frac{C}{D}$	1.0	1.5	2.5	1.0	1.5	2.5	1.0	1.5	2.5
Z (m)	7.5	10	15	7.5	10	15	7.5	10	15
$\frac{Z}{D}$	1.5	2.0	3.0	1.5	2.0	3.0	1.5	2.0	3.0
s_u (kPa)	45	60	90	60	80	120	75	100	150

Table 4.1: Vaules of s_u used for different Z at tunnel analysis.

The undrained shear strength profile of the soil is assumed to vary linearly according to equation 4.2 (Fig. 4.2):

$$s_u(z) = s_{u0} + \rho z \tag{4.6}$$

where s_{u0} is the undrained strength at the ground surface, and ρ is the rate of increase of the shear strength with depth. Three different undrained

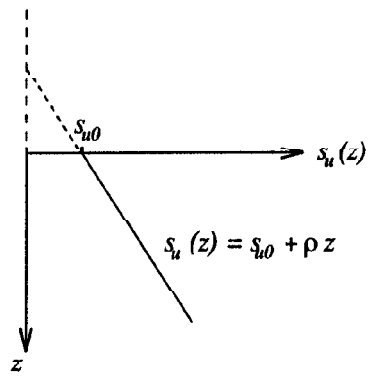

Figure 4.4: Variation of undrained shear strength with depth.

shear strength profiles were considered in the parametric studies of elastic, perfectly-plastic models:

Case 1. $s_{u0} \neq 0, \rho = 0;$

Case 2. $s_{u0} = 0, \rho \neq 0;$

Case 3. $s_{u0} \neq 0, \rho \neq 0.$

The shear strength for each analysis, corresponding to different depths of the tunnel for case 1 and 2, were kept constant at the tunnel axis, and taken from Table 4.1. For case 3, the undrained shear strength profile was obtained in an attempt to model a realistic shear strength profile for London Clay using the following expression:

$$\left(\frac{s_u}{\sigma'_v}\right) = \left(\frac{s_u}{\sigma'_v}\right)_{nc} (OCR)^{\Lambda} \tag{4.7}$$

where $(\frac{s_u}{\sigma'_v})_{nc} = 0.26$ and $\Lambda = 0.615$ (Wood, 1992). A removal of 150m of soil on the surface was assumed, and the corresponding OCR was calculated. The resulting undrained shear strength profile (Fig. 4.5) shows close agreement with the data obtained by Marsland (1972) (Fig. 4.6) for in-situ plate tests on London clay. The actual profile used in the analysis is shown on Fig. 4.5, giving the corresponding values of $s_{u0} = 100$kPa, and $\rho = 4.6$kPa/m.

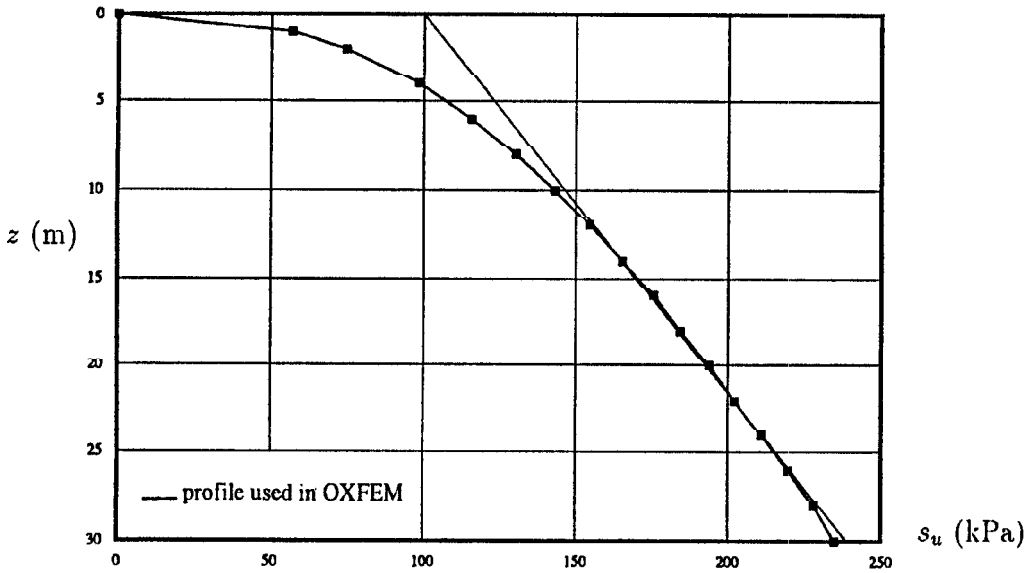

Figure 4.5: Undrained shear strength profile for the non-homogeneous elastic-plastic model with $s_{u0} \neq 0, \rho \neq 0$.

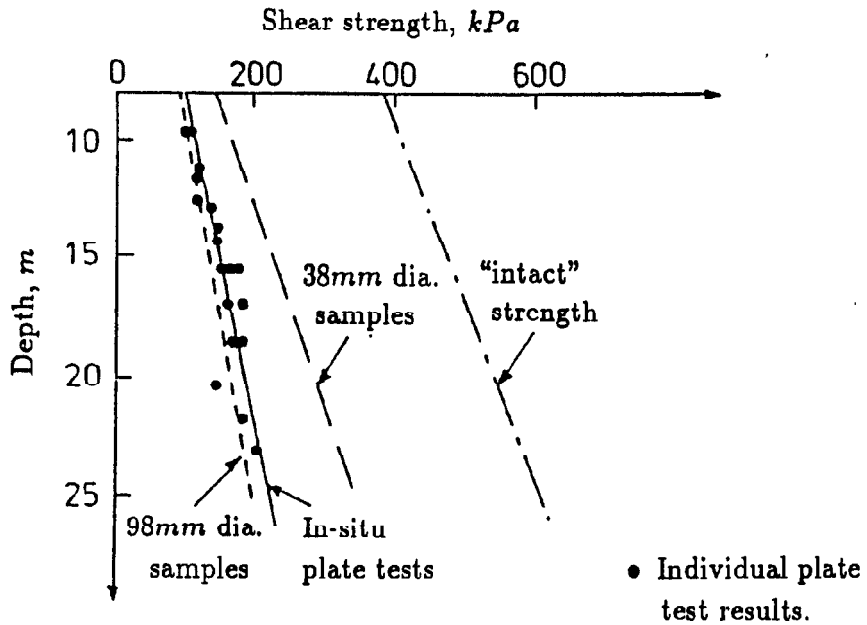

Figure 4.6: Undrained shear strength of London Clay (After Marsland, 1972).

The soil parameters used in each analysis are summarised in Tables 4.2-6.

	Homogeneous			Non homogeneous		
Z (m)	7.5	10	15	7.5	10	15
$\frac{Z}{D}$	1.5	2.0	3.0	1.5	2.0	3.0
G_0 (kPa)	33557	33557	33557	0	0	0
m (kPa/m)	0	0	0	3355.7	3355.7	3355.7
s_{u0} (MPa)	1000	1000	1000	1000	1000	1000
ρ (kPa/m)	0	0	0	0	0	0
reference	1.5eh	2eh	3eh	1.5en	2en	3en

Table 4.2: Soil properties used for linear elastic models.

	Homogeneous								
Z (m)	7.5			10			15		
$\frac{Z}{D}$	1.5			2.0			3.0		
G_0 (kPa)	33557			33557			33557		
m (kPa/m)	0			0			0		
s_{u0} (kPa)	45	60	75	60	80	100	90	120	150
ρ (kPa/m)	0	0	0	0	0	0	0	0	0
$\frac{s_u}{\gamma Z}$	0.3	0.4	0.5	0.3	0.4	0.5	0.3	0.4	0.5
reference	1.5ph3	1.5ph4	1.5ph4	2ph3	2ph4	2ph5	3ph3	3ph4	3ph5

Table 4.3: Soil properties used for elastic, perfectly plastic homogeneous models.

Elastic, perfectly-plastic									
	Non-homogeneous: Case 1								
Z (m)	7.5			10			15		
$\frac{Z}{D}$	1.5			2.0			3.0		
G_0 (kPa)	0			0			0		
m (kPa/m)	3355.7			3355.7			3355.7		
s_{u0} (kPa)	45	60	75	60	80	100	90	120	150
ρ (kPa/m)	0	0	0	0	0	0	0	0	0
$\frac{s_u}{\gamma Z}$	0.3	0.4	0.5	0.3	0.4	0.5	0.3	0.4	0.5
reference	1.5pn3c1	1.5pn4c1	1.5pn4c1	2pn3c1	2pn4c1	2pn5c1	3pn3c1	3pn4c1	3pn5c1

Table 4.4: Soil properties used for elastic, perfectly-plastic non-homogeneous models (Case 1).

Elastic, perfectly-plastic									
	Non-homogeneous: Case 2								
Z (m)	7.5			10			15		
$\frac{Z}{D}$	1.5			2.0			3.0		
G_0 (kPa)	0			0			0		
m (kPa/m)	3355.7			3355.7			3355.7		
s_{u0} (kPa)	0			0			0		
ρ (kPa/m)	6	8	10	6	8	10	6	8	10
$\frac{s_u}{\gamma Z}$	0.3	0.4	0.5	0.3	0.4	0.5	0.3	0.4	0.5
reference	1.5pn3c2	1.5pn4c2	1.5pn4dc2	2pn3c2	2pn4c2	2pn5c2	3pn3c2	3pn4c2	3pn5c2

Table 4.5: Soil properties used for elastic, perfectly-plastic non-homogeneous models (Case 2).

Elastic, perfectly-plastic			
	Non-homogenous: Case 3		
Z (m)	7.5	10	15
$\frac{Z}{D}$	1.5	2.0	3.0
G_0 (kPa)	0	0	0
m (kPa/m)	3355.7	3355.7	3355.7
s_{u0} (kPa)	100	100	100
ρ (kPa/m)	4.6	4.6	4.6
ref.	3pnc3	2pnc3	3pnc3

Table 4.6: Soil properties used for elastic, perfectly-plastic non-homogeneous models (Case 3).

4.3 Presentation of Results

The results from the parametric studies were presented in dimensionless form of $\frac{\delta G}{\gamma D^2} : \frac{x}{D}$, where G is the shear modulus at the tunnel axis. In some cases where the width of the settlement trough, i, and the maximum displacement, δ_{max}, were interested, plots of $\frac{i}{D} : \frac{Z}{D}$ and $\frac{\delta_{max} G}{\gamma D^2} : \frac{Z}{D}$ were presented with independent parameter of $\frac{s_u}{\gamma Z}$, where s_u is the undrained shear strength at the tunnel axis.

It is necessary to define a method to evaluate the width of the computed settlement trough, i. Two methods were attempted.

1. Using linear regression to obtain the gradient of the plot of $ln\delta : x^2$ for each settlement profile, which the value equal to $-\frac{1}{2i^2}$.
2. Establishing the change in the slope of the computed settlement profile.

For the first method which linear regression was used, it was assumed that the predicted settlement profiles followed the shape of an error function curve:

$$\delta = \delta_{max} exp\left(-\frac{x^2}{2i^2}\right) \tag{4.8}$$

Taking natural log for equation 4.8 gives:

$$ln\delta = ln\delta_{max} - \frac{x^2}{2i^2} \tag{4.9}$$

By plotting $ln\delta : x^2$, the gradient obtained would be equal to $-\frac{1}{2i^2}$, and the value of i could be evaluated. A disadvantage of this method lies in the assumption made for the shape of predicted settlement troughs. Although field investigations carried out by Peck (1969) showed that surface settlements in tunnelling problems could be fitted by this type of probability function, computed settlements did not necessarily produce results that could be represented by this type of probability function. This is due to the fact that the data from field investigations were usually obtained in a region comparitively close to the tunnel (eg. $<$ 20m). The predicted value of i becomes inaccurate since it is obtained from the gradient of the $ln\delta : x^2$ plot, and is taken as the best fit line for the total horizontal width of the finite element mesh (200m in this case).

The second method was achieved by establishing the point where the change in the slope of the settlement profile from positive to negative occured. Since the computed settlement profiles were plotted by joining the vertical displacement of each node on the surface of the mesh using straight lines, therefore the change in the slope of the settlement profiles were represented by a change in the gradient of these line segments. Using this method, the results for the whole range of x were considered, and it was more reliable than the first method. Consequently the second method was adopted.

4.4 Parametric Studies on Elastic Clay

4.4.1 Elastic homogeneous clay

The computed results for the three different depths of tunnel axis are shown in Fig. 4.7. Heaves are obtained for all three values of Z. From the displacement vectors plotted for $Z = 10$m (Fig. 4.8), it can be seen that the movement of soil is purely upwards. This is due to the stress relief effect of excavated soil in an purely elastic homogeneous medium. For larger values of Z, the upward movement of soil on the surface is smaller because the surface of the soil is more remote from the loading points around the tunnel periphery.

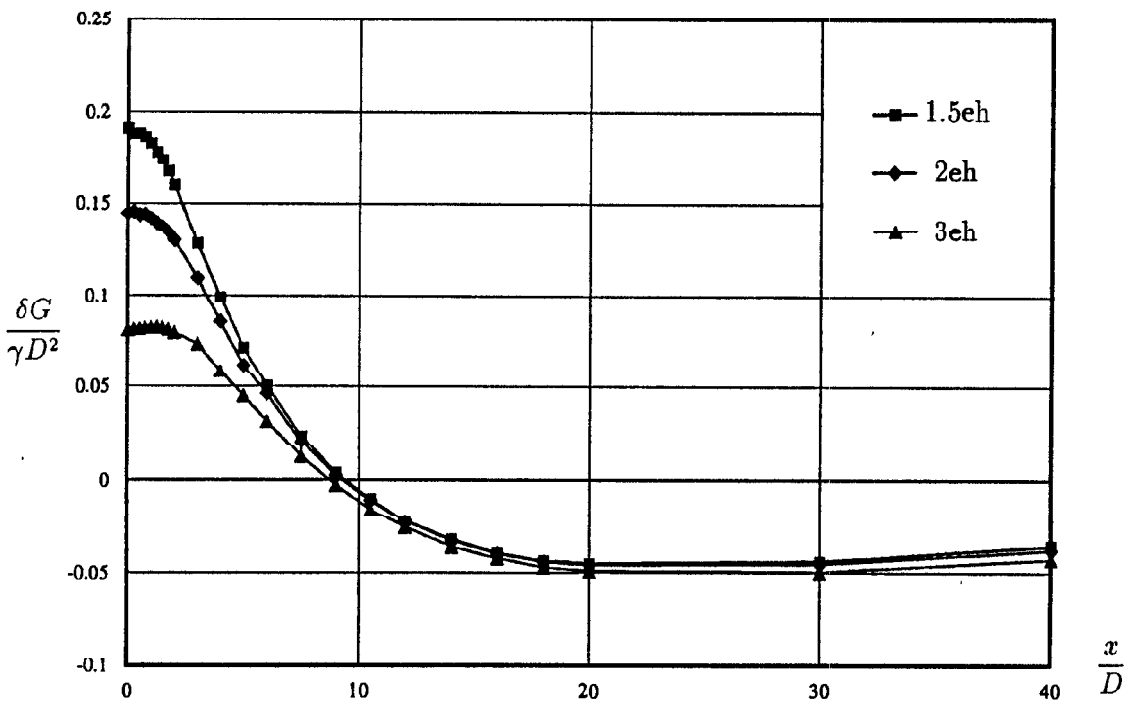

Figure 4.7: Surface displacements for elastic homogeneous model.

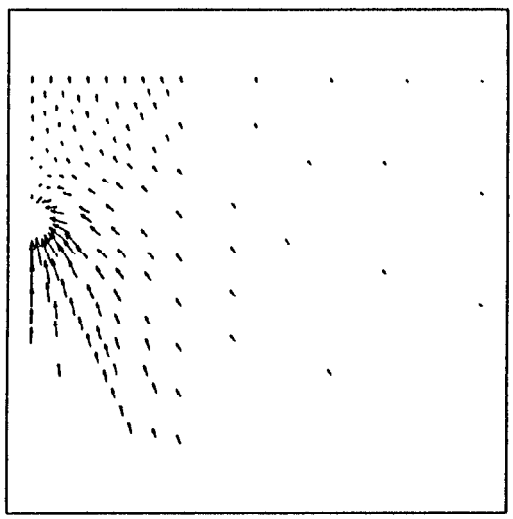

Figure 4.8: Displacement vectors for elastic homogeneous model (Z = 10m).

4.4.2 Elastic non-homogeneous clay

OXFEM provides a non-homogeneous model which material properties can vary with depth. However, verification of the model had not been carried out, and therefore it was necessary to analyses a test problem to ensure that the mathematical formulation and the corresponding computer code would provide correct results. Analysis was carried out for an uniform strip loading on an elastic half-space for which a closed form solution was known. The computed results were compared with the exact solution and found to be satisfactory.

4.2.2.1 Verification of non-homogeneous model

The displacements caused by a smooth uniformly loaded, flexible strip footing on a semi-infinite mass (Fig. 4.9) with linear variation of modulus was solved by Gibson (1967). He considered an elastic half-space where Poisson's ratio remained constant but the shear modulus G increased linearly with

depth as expressed in equation 4.1.

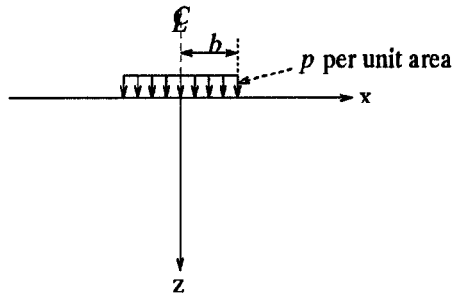

Figure 4.9: Uniform strip loading on semi-infinite mass.

For $G_0 = 0$ and $\nu = 0.5$, the vertical displacement is given by:

$$\delta_z = \frac{p}{2\pi m}\left[tan^{-1}\left(\frac{b+x}{z}\right) + tan^{-1}\left(\frac{b-x}{z}\right)\right] \tag{4.10}$$

where $2b$ is the width of the footing, and x is the horizontal distance from the centre of the footing. For the displacement on the surface (ie. $z = 0$), the equation 4.10 becomes:

$$\delta_z = \frac{p}{2m} \quad \text{for} \quad x < b \tag{4.11}$$

$$\delta_z = 0 \quad \text{for} \quad x > b \tag{4.12}$$

OXFEM was used to analyse the above problem and the results were compared with those of Gibson. The mesh used in the footing analysis in OXFEM is shown in Fig. 4.10. Two values of Poisson's ratio were used: 0.49 and 0.49999 to explore the sensitivity of the model to the value of Poisson's ratio. The displacement curves obtained from OXFEM are plotted in Fig. 4.11, and the exact solution (equations 4.11 and 4.12) is superimposed on the same plot.

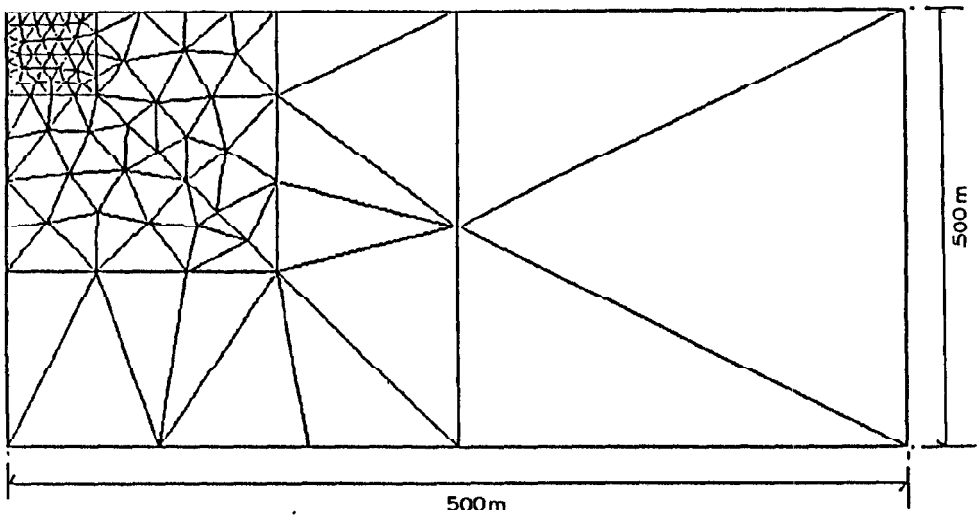

Figure 4.10: Mesh used for footing analysis.

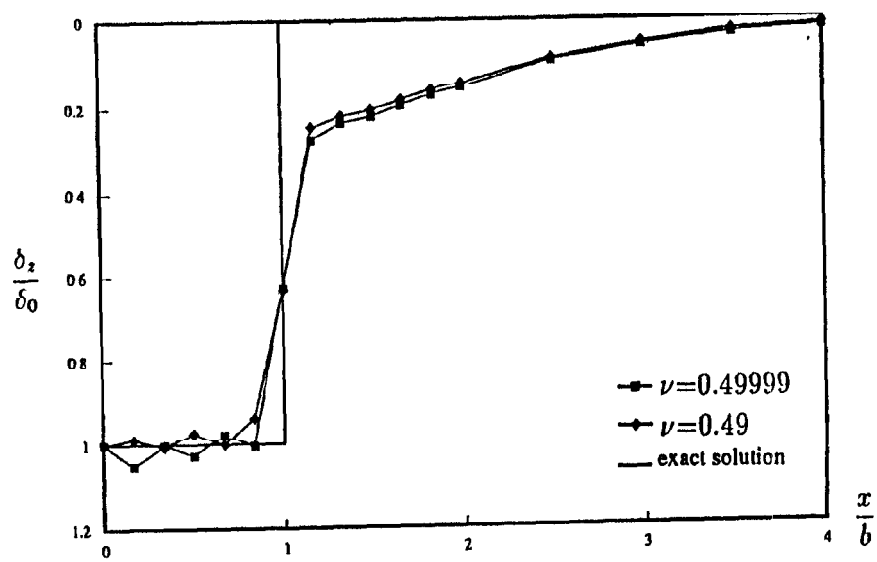

Figure 4.11: Surface displacements due to uniform strip footing on a non-homogeneous elastic medium.

The surface settlement profiles obtained from the finite element analysis agreed with the general shape of the settlement profile from the closed form solution, given that Poisson's ratios of 0.49 and 0.49999 were used instead of 0.5. The value of Poisson's ratio was found not to have a large effect on the computed displacements.

4.2.2.2 Parametric studies on elastic non-homogeneous model

Dimensionless plot of $\frac{\delta G}{\gamma D^2}$: $\frac{x}{D}$ is shown in Fig. 4.12. Plots of $\frac{i}{D}$: $\frac{Z}{D}$ and $\frac{\delta_{max} G}{\gamma D^2}$: $\frac{Z}{D}$ are presented in Fig. 4.13 and 4.14 respectively. Results obtained from Peck's field investigations for the values of $\frac{i}{D}$ for a range of values for $\frac{Z}{D}$ $(1.5 \rightarrow 3.0)$ for soft to stiff clays are superimposed on Fig. 4.13. Although the computed results from OXFEM do not furnish much information about the real behaviour of the soil, they can be treated as a limiting case where s_u is sufficiently large that yielding is prevented in any part of the mesh. The displacement vectors for the case of Z=10m are shown in Fig. 4.15.

4.5 Parametric Studies on Elastic-plastic Clay

4.5.1 Homogeneous elastic-plastic clay

The dimensionless settlement profiles obtained from the finite element analysis for elastic-plastic homogenous soil are shown in Figs. 4.16-18. Each plot corresponds to a constant value $\frac{s_u}{\gamma Z}$. In the case of $\frac{s_u}{\gamma Z}$ = 0.3 (Fig. 4.16), settlements were obtained above the tunnel for $\frac{Z}{D}$=1.5, 2.0 and 3.0 (1.5ph3, 2ph3 and 3ph3). For $\frac{s_u}{\gamma Z}$ = 0.4, settlements were obtained for $\frac{Z}{D}$=3.0 (3ph4). Analyses for $\frac{Z}{D}$=1.5 and 2.0 with $\frac{s_u}{\gamma Z}$ = 0.4(1.5ph4 and 2ph4), and for all three cases of $\frac{Z}{D}$ with $\frac{s_u}{\gamma Z}$=0.5 (1.5ph5, 2ph5 and 3ph5) showed heaving. Larger values of $\frac{s_u}{\gamma Z}$gave greater magnitudes of surface displacement of the soil.

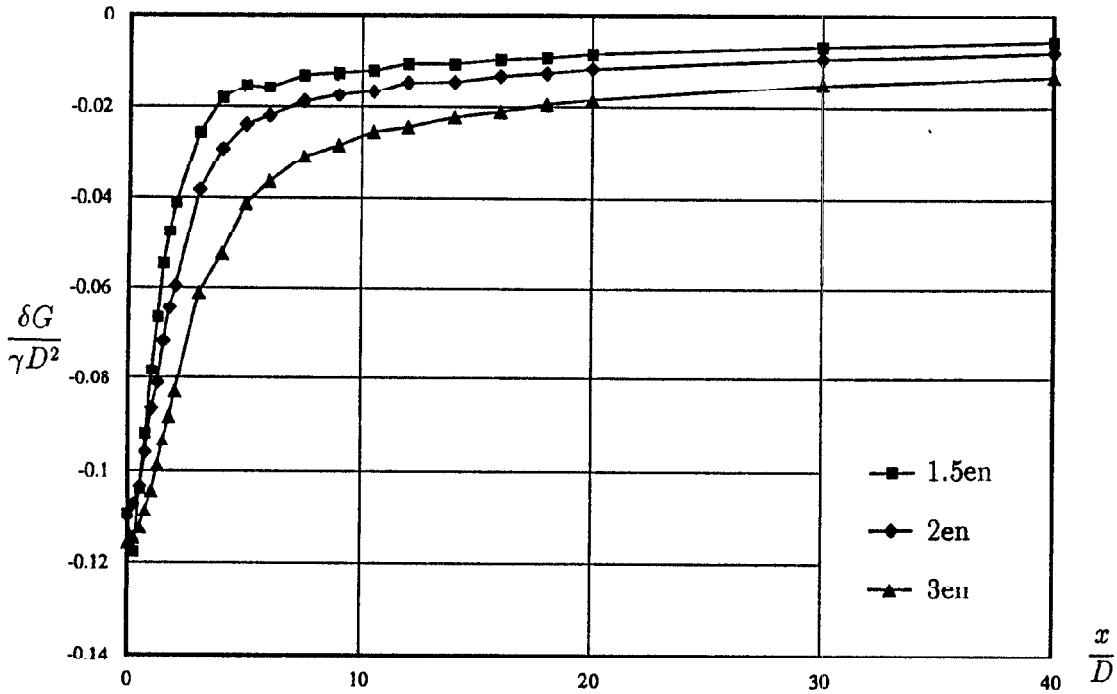

Figure 4.12: Surface displacements for elastic non-homogeneous soil model.

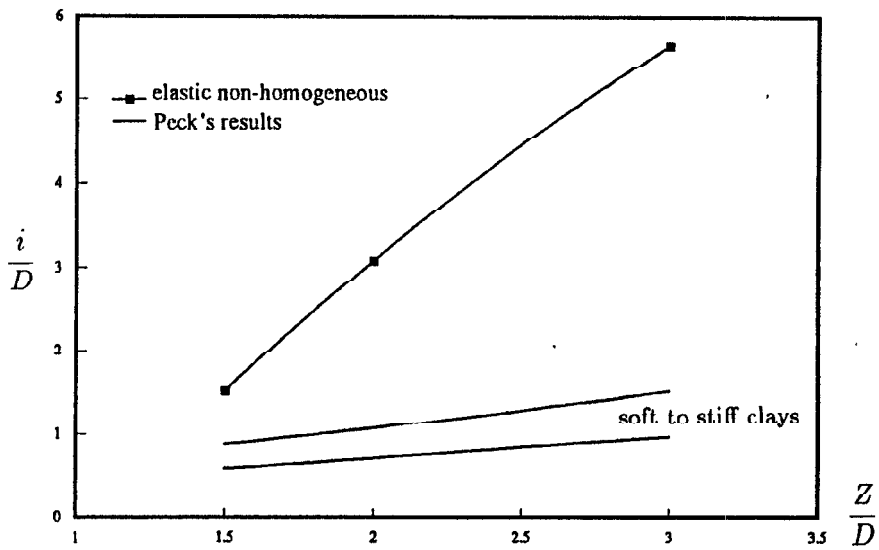

Figure 4.13: Plot of $\frac{i}{D}$ against $\frac{Z}{D}$ for elastic non-homogeneous model.

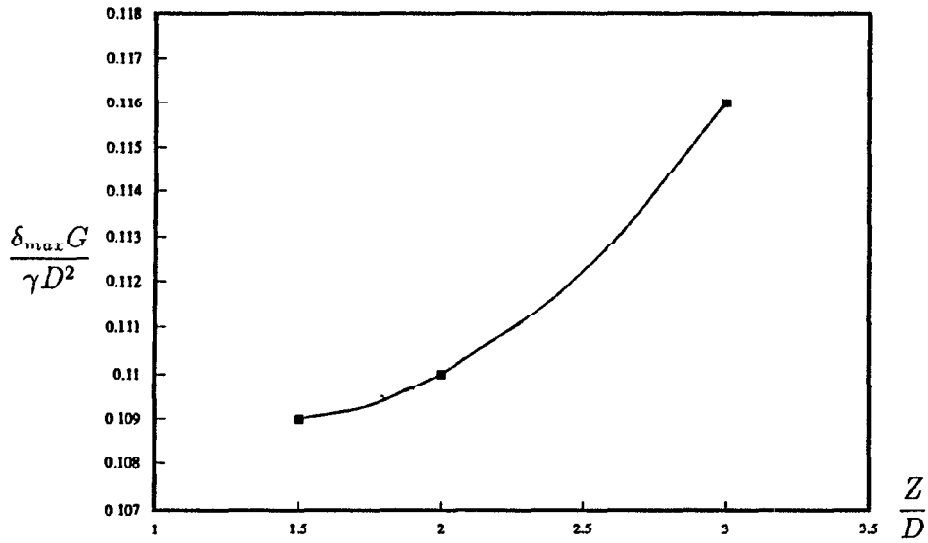

Figure 4.14: Plot of $\frac{\delta_{max}G}{\gamma D^2}$ against $\frac{Z}{D}$ for elastic non-homogeneous model.

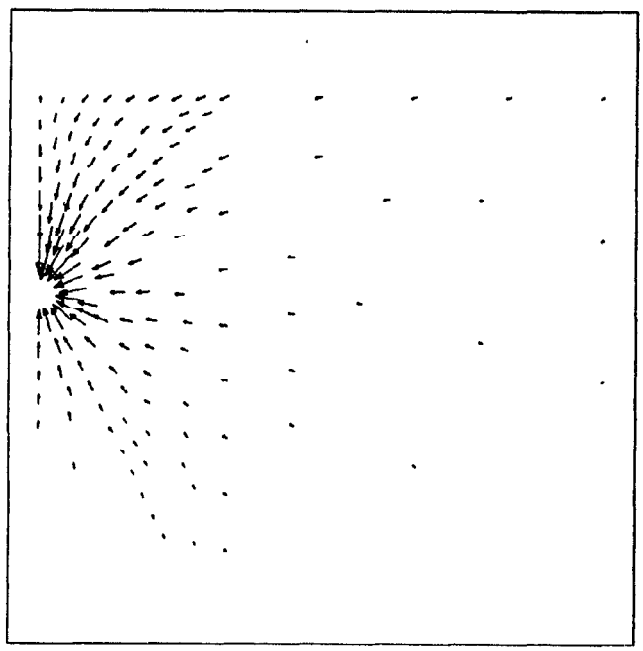

Figure 4.15: Displacement vectors for elastic non-homogeneous model with $Z = 10$m.

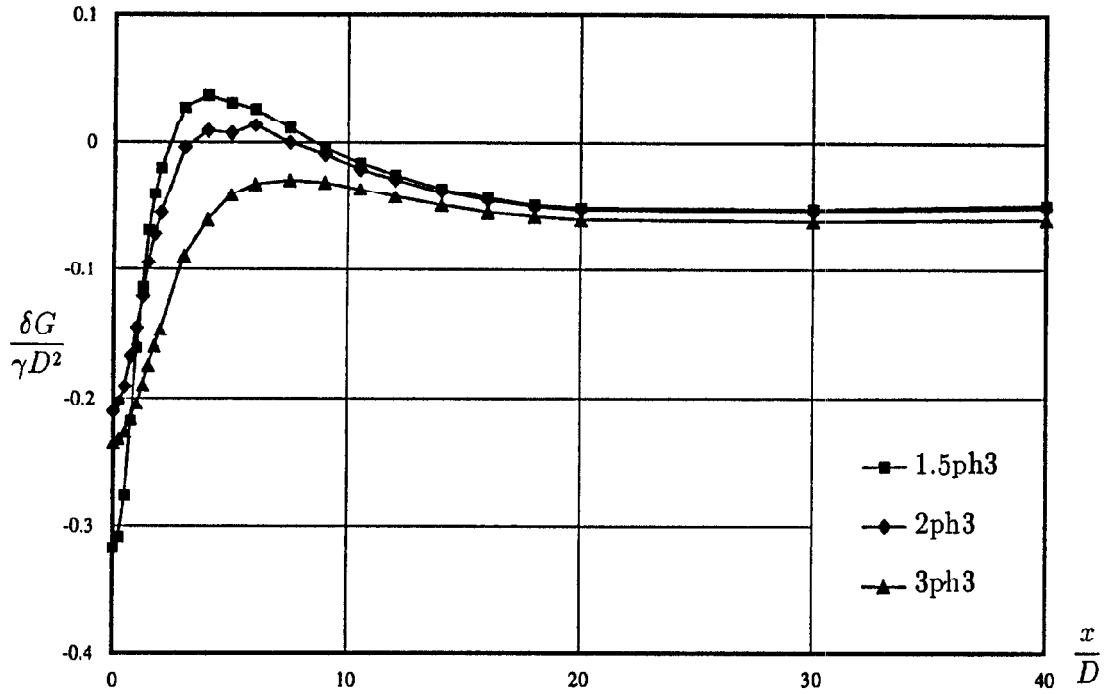

Figure 4.16: Surface displacements for homogeneous elastic-plastic model, $\frac{s_u}{\gamma Z} = 0.3$.

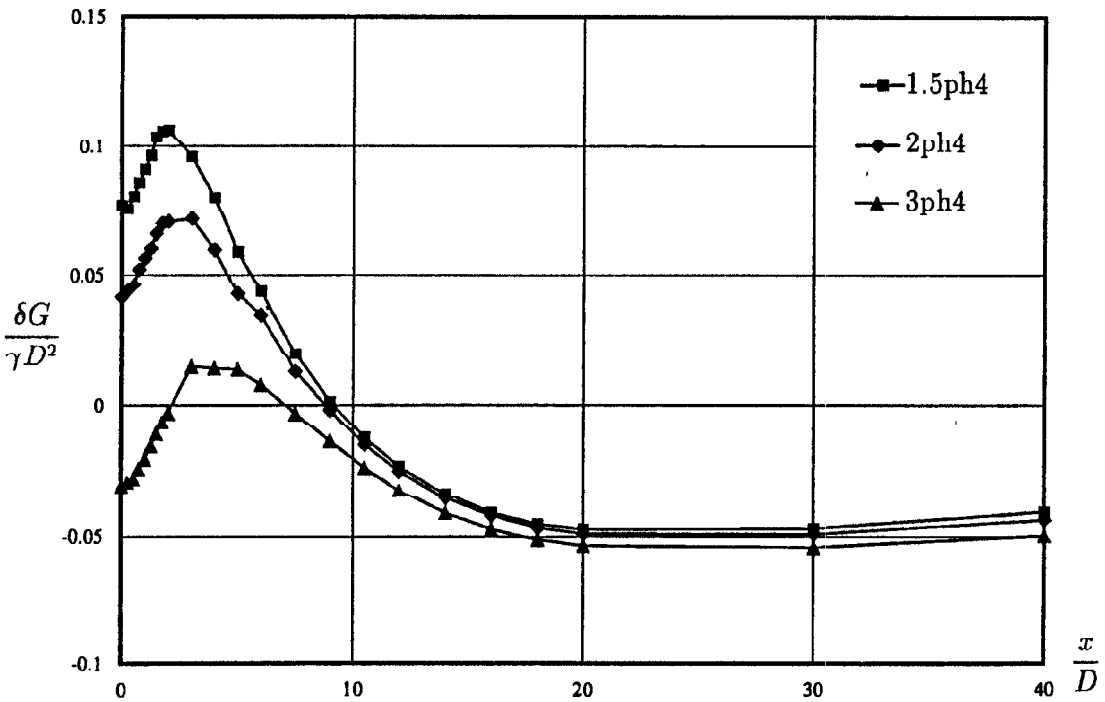

Figure 4.17: Surface displacements for homogeneous elastic-plastic model, $\frac{s_u}{\gamma Z} = 0.4$.

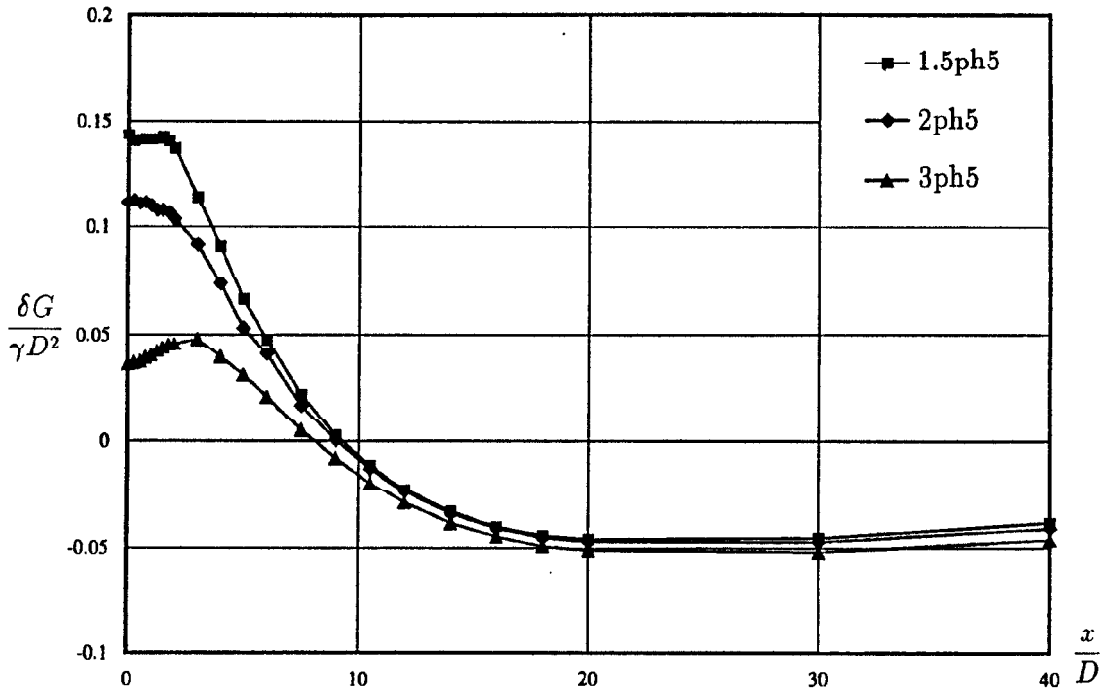

Figure 4.18: Surface displacements for homogeneous elastic-plastic model, $\frac{s_u}{\gamma Z} = 0.5$.

4.5.2 Non-homogeneous elastic-plastic clay

Non-homogeneous linear elastic-plastic soil exhibits variation in both the elastic moduli and the undrained shear strength. The shear modulus profile remains constant for each analysis of non-homogeneous elastic-plastic clay. This permitted the effect of plasticity to be investigated.

Case 1: $s_{u0} \neq 0, \rho = 0$

The dimensionless plots of $\frac{\delta G}{\gamma D^2} : \frac{x}{D}$ from OXFEM are shown in Figs. 4.19-21, each plot corresponding to a constant value of $\frac{s_u}{\gamma Z}$. Relationship between $\frac{i}{D} : \frac{Z}{D}$ and $\frac{\delta_{max} G}{\gamma D^2} : \frac{Z}{D}$ for this case are shown on Figs. 4.22 and 4.23 respectively. Empirical results obtained by Peck are superimposed on Fig. 4.22. It can be seen that for a model with constant undrained shear strength through-

out the medium, the maximum surface settlement increases with decreasing undrained strength of soil. On the other hand, the width of settlement trough increases with increasing strength.

Case 2: $s_{u0} = 0, \rho \neq 0$

Plots of $\frac{\delta G}{\gamma D^2} : \frac{x}{D}$ for three different values of $\frac{s_u}{\gamma Z}$ (0.3, 0.4 and 0.5) are shown in Figs. 4.24-26. Complete dimensionless plots of $\frac{i}{D} : \frac{Z}{D}$ and $\frac{\delta_{max} G}{\gamma D^2} : \frac{Z}{D}$ could not be obtained since failure of soil occured for some cases. The results are consistent with those established by Davis *et al* (1980) on the stability of tunnels (Fig. 4.10). For $\frac{s_u}{\gamma Z}$ =0.3 ($N \approx 3.33$), failure occurs when $\frac{Z}{D}$=1.5 and 2 (1.5pn3c2, 2pn3c2). For $\frac{s_u}{\gamma Z}$ =0.4 ($N = 2.5$), failure occurs for $\frac{Z}{D}$=1.5. These results agreed with those obtained by Davis *et al.* using the lower bound plasticity theorem (Fig. 4.3).

Case 3: $s_{u0} \neq 0, \rho \neq 0$

The results obtained from OXFEM for this case are shown in Fig. 4.27. Dimensionless plots of $\frac{i}{D}:\frac{Z}{D}$ and $\frac{\delta_m Z}{\gamma D^2}:\frac{Z}{D}$ are obtained and shown on Figs. 4.28 and 4.29 respectively. The empirical relationship of $\frac{i}{D} : \frac{Z}{D}$ from Peck's investigations is superimposed on Fig. 4.28. It can be seen that the widths of settlement trough predicted are larger than realistic values.

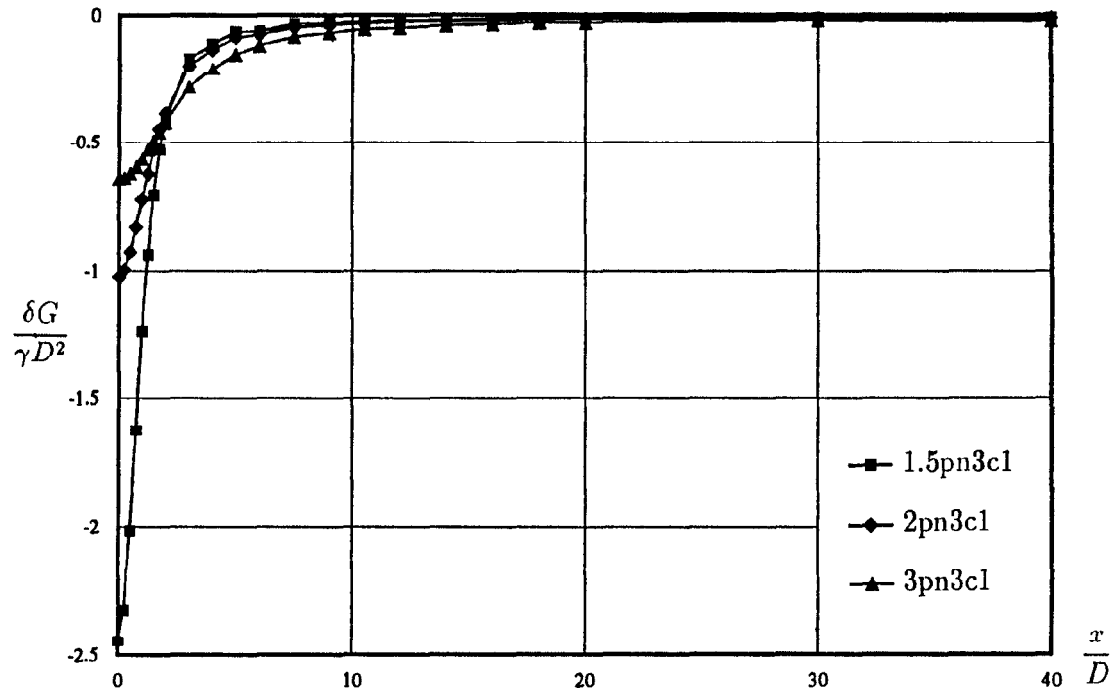

Figure 4.19: Surface displacements for non-homogeneous elastic-plastic model, $\frac{s_u}{\gamma Z} = 0.3$ (Case 1).

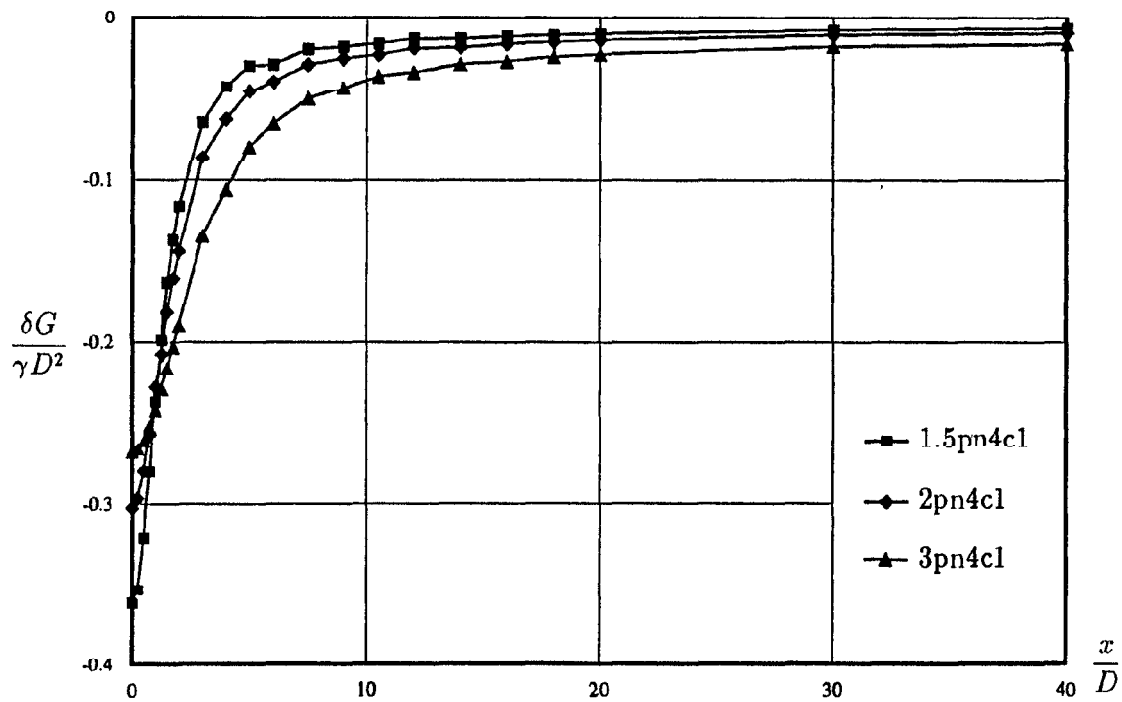

Figure 4.20: Surface displacements for non-homogeneous elastic-plastic model, $\frac{s_u}{\gamma Z} = 0.4$ (Case 1).

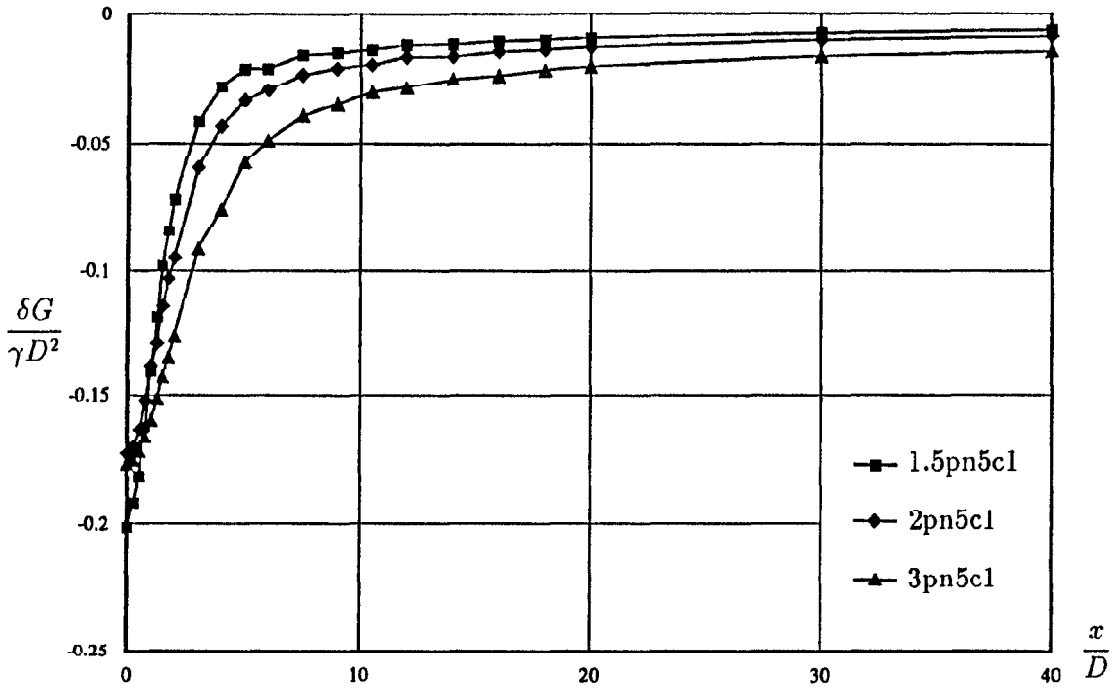

Figure 4.21: Surface displacements for non-homogeneous elastic-plastic model, $\frac{s_u}{\gamma Z} = 0.5$ (Case 1).

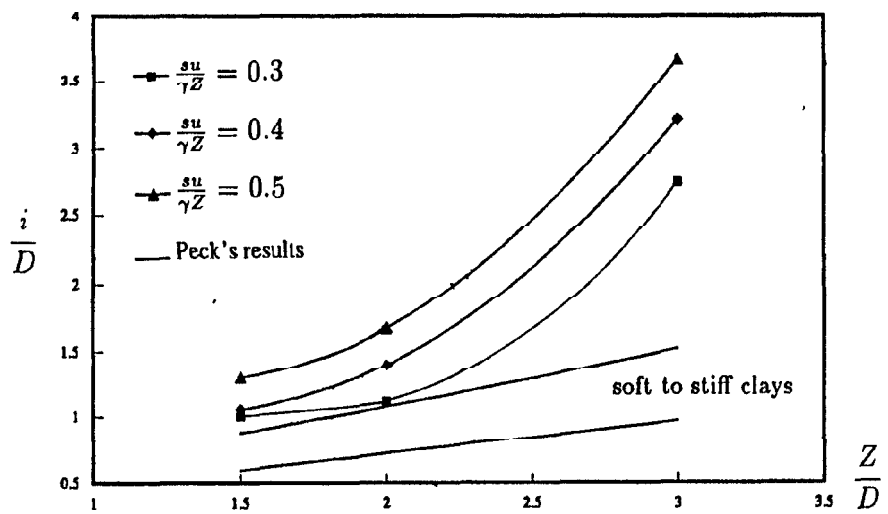

Figure 4.22: Plot of $\frac{i}{D} : \frac{Z}{D}$ for non-homogeneous elastic-plastic model (Case 1).

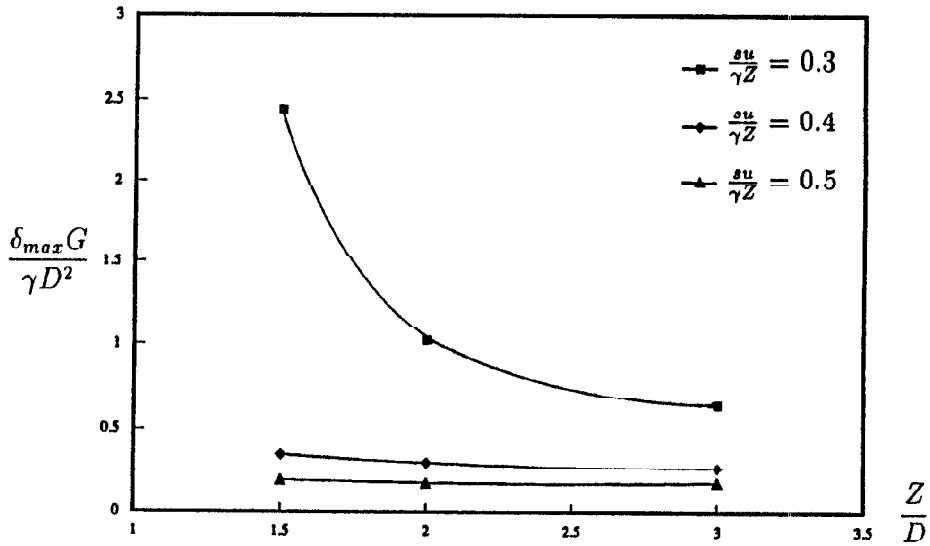

Figure 4.23: Plot of $\frac{\delta_{max} G}{\gamma D^2}$: $\frac{Z}{D}$ for non-homogeneous elastic-plastic model (Case 1).

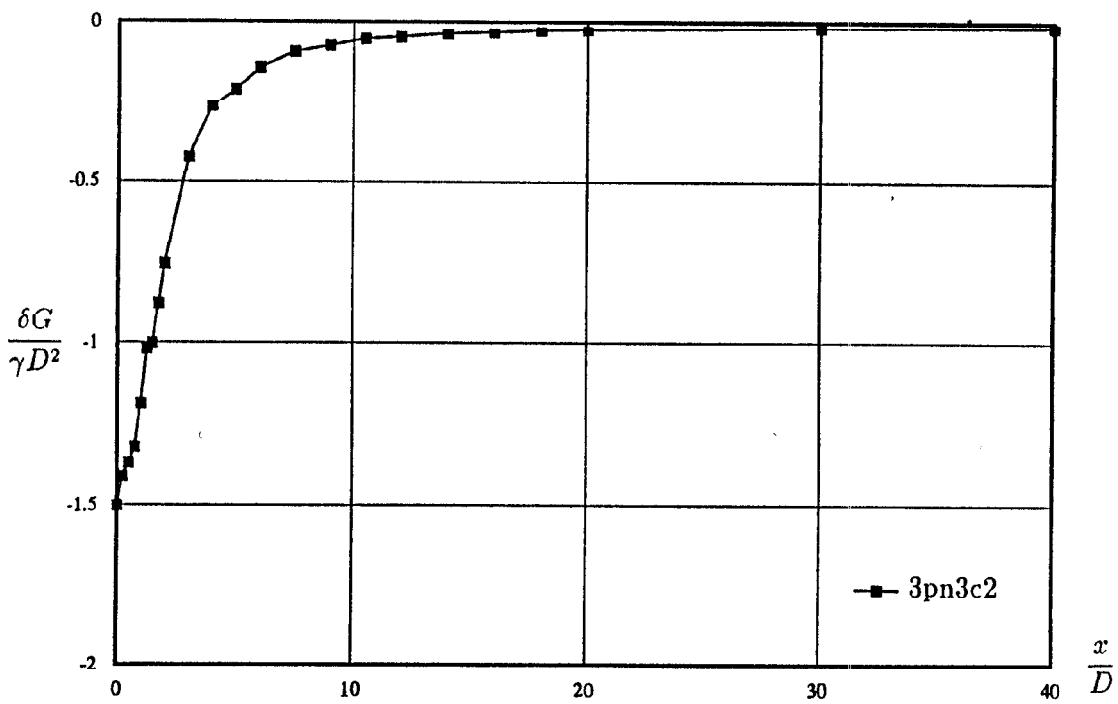

Figure 4.24: Surface displacements for non-homogeneous elastic-plastic model, $\frac{\delta_y}{\gamma Z} = 0.3$ (Case 2).

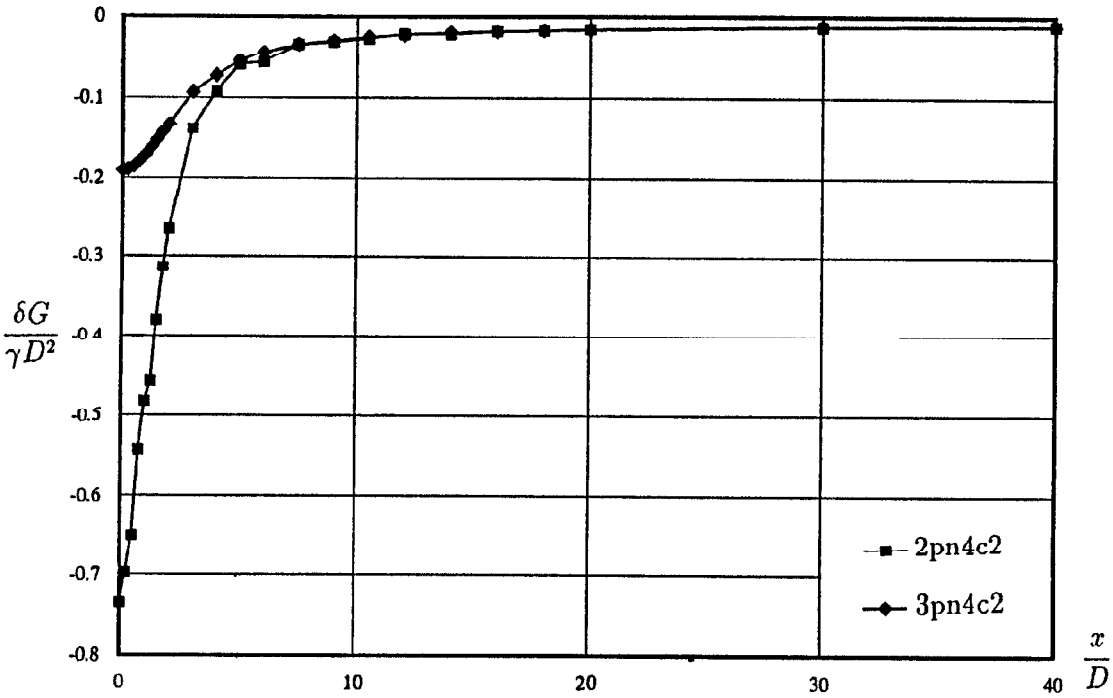

Figure 4.25: Surface displacements for non-homogeneous elastic-plastic model, $\frac{s_u}{\gamma Z} = 0.4$ (Case 2).

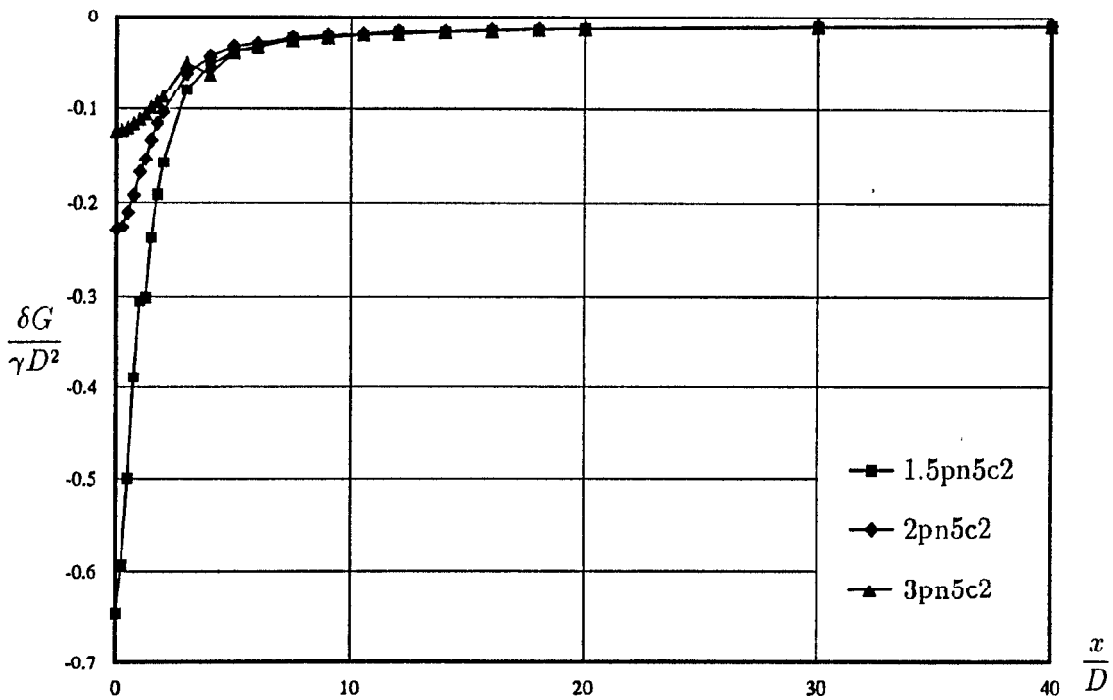

Figure 4.26: Surface displacements for non-homogeneous elastic-plastic model, $\frac{s_u}{\gamma Z} = 0.5$ (Case 2).

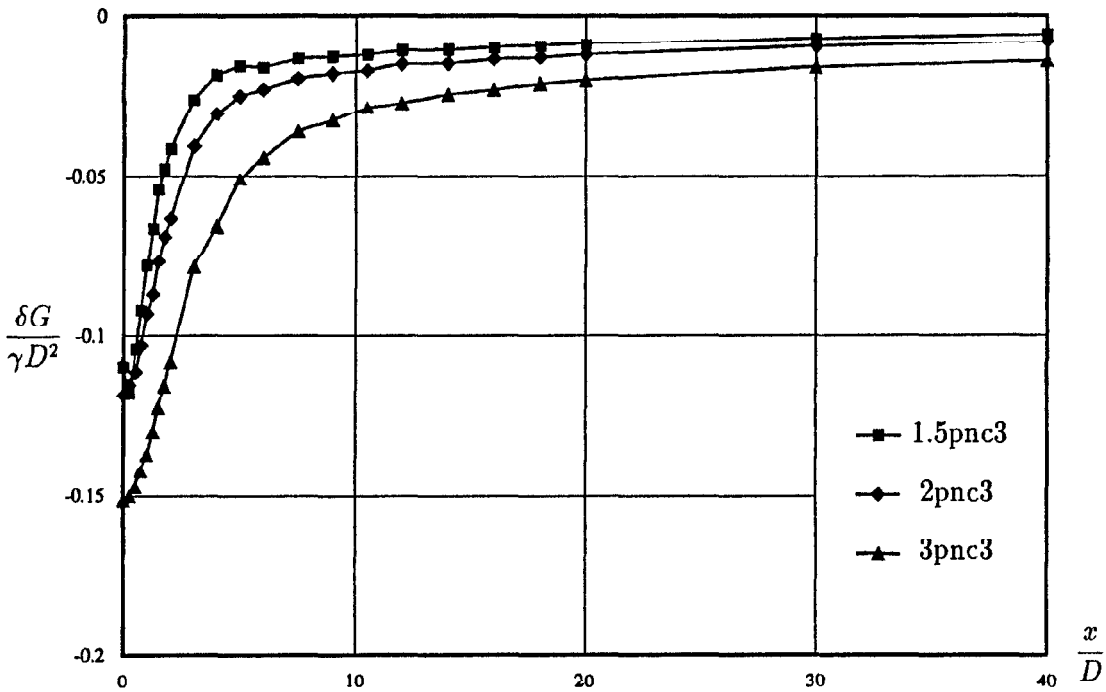

Figure 4.27: Surface displacements for non-homogeneous elastic-plastic model (Case 3).

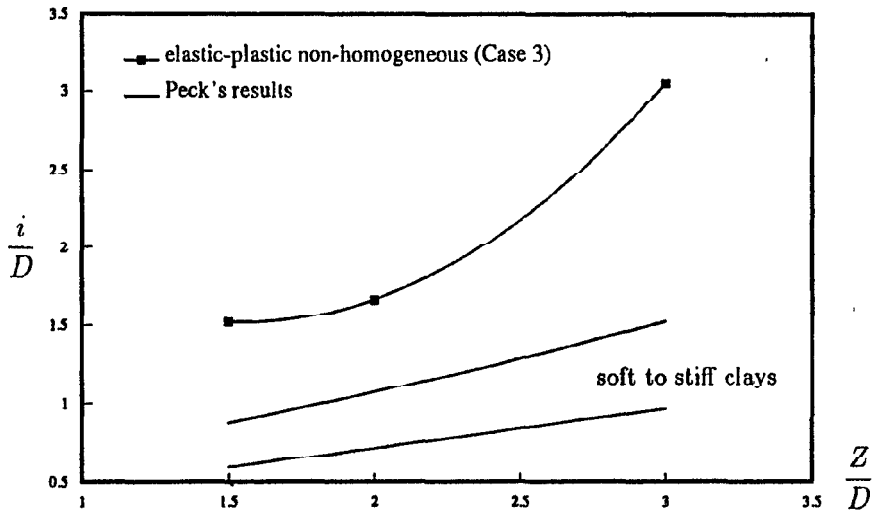

Figure 4.28: Plot of $\frac{i}{D} : \frac{Z}{D}$ for non-homogeneous elastic-plastic model (Case 3).

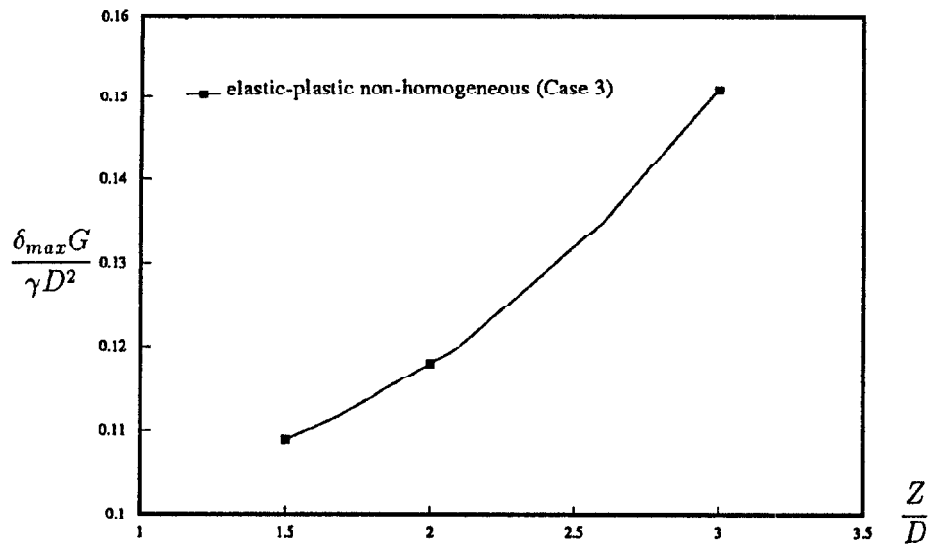

Figure 4.29: Plot of $\frac{\delta_{max}G}{\gamma D^2}$: $\frac{Z}{D}$ for non-homogeneous elastic-plastic model (Case 3).

4.6 Linear Models for the Prediction of Settlement Profiles

The linear elastic homogeneous model predicts heaving for shallow tunnelling problems, while the elastic non-homogeneous model predicts settlements. The introduction of plasticity results in larger displacements and narrower settlement troughs.

The results from the various elastic and elastic-plastic soil models used in this chapter can be compared using a combined dimensionless plot of $\frac{i}{D}$: $\frac{Z}{D}$ as presented in Fig. 4.30. The elastic non-homogeneous model (1.5en, 2en and 3en) predicts the maximum width of a settlement trough that can be expected for different depths of tunnel. When plasticity is introduced, the

width of a settlement trough decreases. Comparison of the computed results with Peck's field investigations show that linear elastic and elastic-plastic models predict wider settlement.

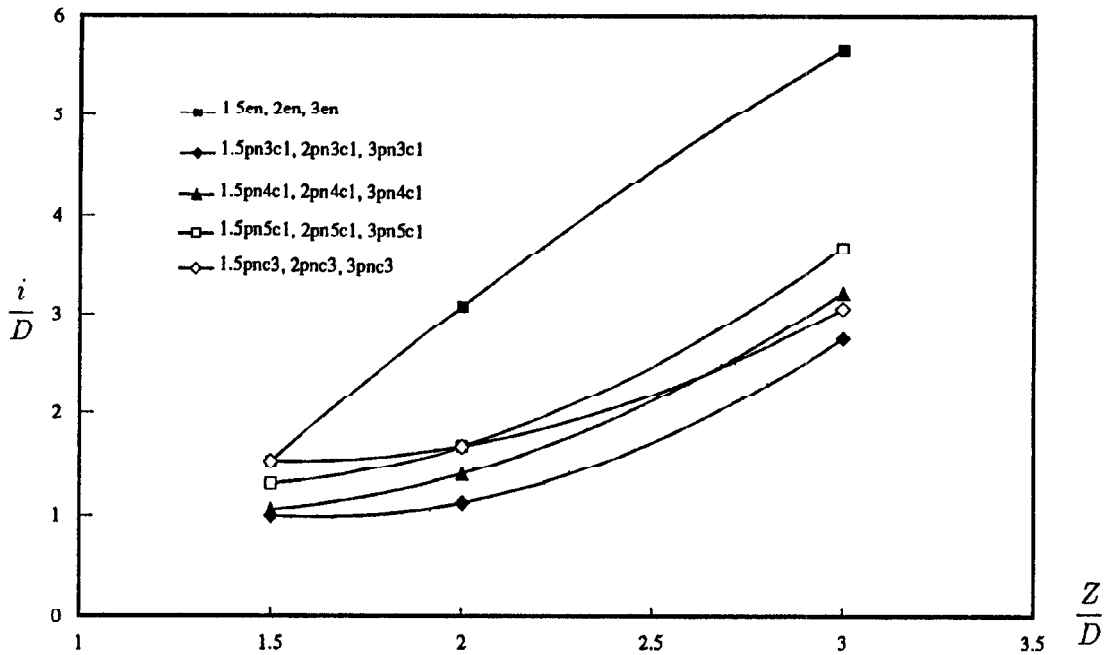

Figure 4.30: Plot of $\frac{i}{D} : \frac{Z}{D}$ for various soil models.

Chapter 5

NON-LINEAR ELASTICITY OF CLAY

5.1 Introduction

This chapter contains a discussion of the use of a non-linear elastic soil model in finite element analysis. Its effectiveness in predicting surface settlements in tunnelling problems is explored.

The use of linear elastic-plastic models is not ideal for shallow tunnelling problems. Such models overestimate the width of settlement troughs, and in some cases predict surface heave (Chapter 4). The difference between the real and predicted settlement profiles is thought to be due to the non-linear behaviour of soil at strain levels below those necessary to cause large plastic deformation. Non-linearity results in more local movement of the soil, producing narrower settlement troughs than for a linear model.

In elastic-plastic soil models, it is assumed that yield surfaces exist which bound the regions of stress space which can be reached by a soil without incurring irrecoverable deformations. Within the yield surface deformations are entirely recoverable and elastic. However, real soils show a more grad-

ual yielding process. The strain response on unloading and reloading is hysteretic. There is no longer a one-to-one relationship between stress and strain in the region conventionally thought of as elastic. The two main aspects are the effect of strain amplitude and of stress amplitude on the stiffness of the soil. Experimental studies showed that the stiffness of soil at small strain level is higher than that usually assumed (eg. Jardine *et al*, 1984). On the other hand, there is evidence that the elastic moduli of soil increase with increasing stress amplitude (eg. Janbu, 1963). The effect of stress amplitude on the behaviour of soil is discussed in this chapter, while the effect of strain amplitude is investigated in Chapter 6.

The non-linear elastic soil model that has been implemented into OXFEM exhibits the material property which the elastic moduli are dependent on the current stress state. The stiffness of the material increases with increasing stress. Constitutive laws required to model this behaviour were obtained by Houlsby and Rojas (1993), and were translated into computer codes to produce the material stiffness matrix $\boldsymbol{D}$. The $\boldsymbol{D}$ matrix relates the strain rate vector to the stress rate vector. In tensor notation, the relationship can be expressed as

$$\dot{\sigma}_{ij} = d_{ijkl}\dot{\epsilon}_{kl} \tag{5.1}$$

where d_{ijkl} is the stiffness tensor. Stress updating procedures were also developed.

5.2 Formulation of the Model

Experimental studies (Janbu, 1963) showed that the relationship between initial tangent modulus and confining pressure in the test could be expressed

as:

$$E_i = kp_a\left(\frac{\sigma_3}{p_a}\right)^n \tag{5.2}$$

where E_i is the initial tangent modulus; σ_3 is the minor principal stress; p_a the atmospheric pressure; and n and k are material parameters. The parameter n is the exponent that determines the rate of variation of E_i with σ_3, while parameter k is a modulus number. The value of k during unloading-reloading is higher than that for primary loading.

More rigorously the elastic moduli can be expressed as power functions of mean effective stress rather than the minor principal stress. For the non-linear elastic model that has been implemented into OXFEM, with elastic stiffness dependent on the stress level, the unloading-reloading behaviour is not considered. The bulk and shear moduli are assumed to follow the form of power functions of the mean effective stress p' as:

$$\frac{K}{p_a} = k\left(\frac{p'}{p_a}\right)^n \tag{5.3}$$

$$\frac{G}{p_a} = g\left(\frac{p'}{p_a}\right)^n \tag{5.4}$$

where K and G are the bulk and shear moduli respectively, p_a is a reference pressure (taken as the atmospheric pressure), k and g are dimensionless constants and n is the exponent which determines the influence of the pressure on the moduli. The value of n for a granular material would be typically in the range 0.3 to 0.7. For n=0 moduli are independent of pressure, and for n=1.0 moduli are proportional to pressure. Although it is possible to use different exponents for the bulk and shear moduli expressions, this would result in a Poisson's ratio which would vary with pressure. There is little evidence that substantially different exponents are needed to model the behaviour of soils, and so the two exponents are taken to be equal.

For most non-linear soil models in which the elastic tangent moduli depend on the stress level, a power function of the mean stress (equations 5.3, 5.4) is usually assumed. However, simple models of this sort can result in behaviour which violates the laws of thermodynamics.

Houlsby and Rojas derived equations for elastic models which allow variation of moduli as a power function of mean stress, whilst guaranteeing thermodynamic acceptability. The elastic moduli are expressed as functions of stresses, which can be derived from a free energy (or elastic strain energy) potential. The free energy function proposed was:

$$F = \frac{p_a}{2-n} k^{\frac{1}{1-n}} (1-n)^{\frac{2-n}{1-n}} \left[\epsilon_{ii}\epsilon_{jj} + \frac{3g\epsilon'_{ij}\epsilon'_{ij}}{k(1-n)} \right]^{\frac{2-n}{2-2n}} \tag{5.5}$$

where the deviatoric strain $\epsilon'_{ij} = \epsilon_{ij} - \frac{1}{3}\epsilon_{mm}\delta_{ij}$, and δ_{ij} is the Kronecker delta ($\delta_{ij} = 1$ if $i = j$, $\delta_{ij} = 0$ if $i \neq j$). The corresponding complementary energy expression for $n \neq 1$ is:

$$E = \frac{1}{p_a^{1-n}(1-n)(2-n)} \left[\sigma_{ii}\sigma_{jj} + \frac{k(1-n)}{3g}\sigma'_{ij}\sigma'_{ij} \right]^{\frac{2-n}{2}} \tag{5.6}$$

where the deviatoric stress $\sigma'_{ij} = \sigma_{ij} - \frac{1}{3}\sigma_{mm}\delta_{ij}$. For $n = 1$, the above expression becomes singular, but the complementary energy may be written in the form:

$$E = \frac{\sigma_{ii}}{3k}\left[ln\left(\frac{\sigma_{jj}}{3p_a}\right) - 1 \right] + \frac{3\sigma'_{ij}\sigma'_{ij}}{4g\sigma_{kk}} \tag{5.7}$$

For $n \neq 1$, the tangent compliance matrix can be derived from the above expression using $c_{ijkl} = \frac{\partial^2 E}{\partial\sigma_{ij}\partial\sigma_{kl}}$ as:

$$c_{ijkl} = \frac{1}{p_a^{1-n} k^{\frac{n}{2}} A^{\frac{n+2}{2}}} \left[\frac{A}{9k}\delta_{ij}\delta_{kl} + \frac{A}{2g}(\delta_{ik}\delta_{jl} - \frac{1}{3}\delta_{kl}\delta_{ij}) + \frac{n}{9k}\frac{\sigma'_{mn}\sigma'_{mn}}{2g(i-n)}\delta_{ij}\delta_{kl} \right.$$
$$\left. - \frac{n\sigma_{mm}}{9k2g}(\sigma'_{ij}\delta_{kl} + \sigma'_{kl}\delta_{ij}) - \frac{n(1-n)}{(2g)^2}\sigma'_{kl}\sigma'_{ij} \right] \tag{5.8}$$

where

$$A = \frac{\sigma_{mm}\sigma_{nn}}{9k} + \frac{(1-n)\sigma'_{mn}\sigma'_{mn}}{2g} \tag{5.9}$$

When $n = 1$, then the compliance matrix can be expressed as:

$$\begin{aligned} c_{ijkl} &= \frac{1}{p_a^{1-n}}\left(\frac{\sigma_{mm}}{3}\right)^{-n}\left[\delta_{ij}\delta_{kl}\left(\frac{1}{9k} + \frac{n(1+n)}{4g}\frac{\sigma'_{mn}\sigma'_{mn}}{\sigma_{mm}\sigma_{nn}}\right)\right. \\ &+ \left.\frac{\delta_{ik}\delta_{jl} - \frac{1}{3}\delta_{kl}\delta_{ij}}{2g} - \frac{n}{2g\sigma_{mm}}(\sigma'_{ij}\delta_{kl} + \sigma'_{kl}\delta_{ij})\right] \end{aligned} \tag{5.10}$$

The tangent compliance matrices given in equation 5.8 and 5.10 are inverted to give the material stiffness matrices for use in OXFEM.

5.3 Implementation of the Non-linear Elastic Model in OXFEM

Introduction of new material properties to OXFEM involves two steps:

1. Development of computer coding for constitutive laws to provide the material stiffness matrix.
2. Establishment of suitable algorithms for the corresponding stress updating subroutine.

Step 1

In vector notation, the strain rate $\dot{\sigma}$ is related to the stress rate $\dot{\epsilon}$ by the material stiffness matrix $\boldsymbol{D}$. The convention of the strain rate vector adopted in the current version of OXFEM is defined as:

$$\dot{\epsilon} = \begin{pmatrix} \dot{\epsilon_{11}} \\ \dot{\epsilon_{22}} \\ \dot{\epsilon_{33}} \\ \dot{\gamma_{12}} \\ 2\dot{\theta_{12}} \end{pmatrix} \tag{5.11}$$

where subscripts 1,2,3 represent the three orthogonal axes of the global co-ordinates system. The corresponding stress rate vector is defined as:

$$\dot{\sigma} = \begin{pmatrix} \dot{\sigma_{11}} \\ \dot{\sigma_{22}} \\ \dot{\sigma_{33}} \\ \dot{\tau_{12}} \\ 0 \end{pmatrix} \tag{5.12}$$

where the zero entry in the stress rate vector corresponds to the rotation term in the strain rate vector. Therefore the material stiffness matrix is required to be calculated in the form of a 5×5 array. To transfer equations 5.8 and 5.10 to computer language which can generate a 5×5 compliance matrix, each element in the matrix is calculated with the appropriate subscripts $(ijkl)$ for equations 5.8 and 5.10. The resulting compliance matrix C can be written in the form:

$$C = \begin{pmatrix} c_{1111} & c_{1122} & c_{1133} & c_{1112}+c_{1121} & 0 \\ c_{2211} & c_{2222} & c_{2233} & c_{2212}+c_{2221} & 0 \\ c_{3311} & c_{3322} & c_{3333} & c_{3312}+c_{3321} & 0 \\ c_{1211}+c_{2111} & c_{1222}+c_{2122} & c_{1233}+c_{2133} & c_{1212}+c_{1221}+c_{2112}+c_{2121} & 0 \\ 0 & 0 & 0 & 0 & 0 \end{pmatrix} \tag{5.13}$$

where the rotation terms are zero. For large strain analysis this matrix is augmented by the Jaumann rotation terms and inverted to give the material stiffness matrix D. For small strain analysis only a 4×4 submatrix is required. In each case this is achieved in OXFEM using numerical methods. The element stiffness matrix can then be produced.

Step 2

As discussed in section 3.2.2, three operations are required to calculate the updated Gauss point stresses after the incremental displacements have been calculated.

Incremental Gauss point stresses can be obtained in two ways. One approach is to integrate the constitutive eqautions:

$$\Delta\boldsymbol{\sigma} = \int_t^{t+\Delta t} \boldsymbol{D}\dot{\epsilon}dt \tag{5.14}$$

where $\boldsymbol{D}$ is the material stiffness matrix, and Δt represents the length of the load step. The matrix $\boldsymbol{D}$ is obtained as described in Step 1, and integration is done numerically.

The second method is to obtain the updated stresses using closed form solutions. In equation 5.5, the free energy F is written as a function of the strain ϵ_{ij}, and in equations 5.6 and 5.7, the expression for the complementary energy E are written as a function of stresses σ_{ij}. The relationship between the free energy and the complementary energy can be expressed as:

$$E = \sigma_{ij}\epsilon_{ij} - F \tag{5.15}$$

Differentiating equation 5.15 we obtain:

$$\sigma_{ij} = \frac{\partial F}{\partial \epsilon_{ij}} \tag{5.16}$$

$$\epsilon_{ij} = \frac{\partial E}{\partial \sigma_{ij}} \tag{5.17}$$

Using equations 5.16-17, expressions for σ_{ij} in terms of ϵ_{ij}, and ϵ_{ij} in terms of σ_{ij} can be obtained (equations 5.18-20):

$$\sigma_{ij} = p_a k^{\frac{n}{2(1-n)}}(1-n)^{\frac{1}{1-n}}\left[k\epsilon_{kk}\epsilon_{ll} + \frac{2g}{(1-n)}\epsilon'_{kl}\epsilon'_{kl}\right]^{\frac{n}{2(1-n)}} \left[k\epsilon_{kk}\delta_{ij} + \frac{2g}{(1-n)}\epsilon'_{ij}\right] \tag{5.18}$$

For $n \neq 1$:

$$\epsilon_{ij} = \frac{1}{p_a^{1-n}k^{\frac{n}{2}}(1-n)}\left[\frac{\sigma_{mm}\sigma_{nn}}{9k} + \frac{(1-n)}{2g}\sigma'_{ij}\sigma'_{ij}\right]^{-\frac{n}{2}} \left[\frac{\sigma_{mm}}{9k}\delta_{ij} + \frac{(1-n)}{2g}\sigma'_{ij}\right] \tag{5.19}$$

and for $n = 1$:

$$\epsilon_{ij} = \frac{1}{3k}\left[ln\left(\frac{\sigma_{jj}}{3p_a}\right) - 1 + \frac{\sigma_{ii}}{\sigma_{jj}}\right]\delta_{ij} + \frac{3}{4g}\left[\frac{2\sigma_{kk}\sigma'_{ij} - \sigma'_{ij}\sigma'_{ij}\delta_{ij}}{\sigma_{kk}\sigma_{kk}}\right] \qquad (5.20)$$

However, equations 5.18-20 are not in incremental form. The resulting σ_{ij} from equation 5.18 (or ϵ_{ij} from equation 5.19, 5.20) are values calculated from an initial strain free (or stress free) state. To provide the stress updating procedure using closed form solutions in OXFEM where an incremental approach is used, three steps are required:

1. Use equations 5.19 and 5.20 to calculate the total strains ($\epsilon^{\wedge}_{ij}$) for the Gauss point stresses for the $\wedge^{th}$ load step in the analysis.
2. Add the total strains ($\epsilon^{\wedge}_{ij}$) for the $\wedge^{th}$ load step to the strain increments in the $(\wedge+1)^{th}$ load step to give the total strains for the $(\wedge+1)^{th}$ load step, $\epsilon^{\wedge+1}_{ij}$.
3. Substitute the strains $\epsilon^{\wedge+1}_{ij}$ in equations 5.18 to find the updated stress for each Gauss point.

5.4 Verification of the Formulation

It is important to verify any mathematical formulation and the corresponding computer coding by checking against test problems which have known solution. Displacement controlled plane strain compression was used as the test problem. Two values of $n = 0.4$ and 1.0 were used in the analysis so that the implementation of equation 5.8 and 5.10 could be checked against the closed form solutions (equations 5.18-20). The mesh used in OXFEM has a rigid base (Fig. 5.1).

The results obtained from OXFEM for $n = 0.4$ and 1.0 are shown in Fig. 5.2, with the closed form solutions superimposed. For both cases, finite element results are in very close agreement with the closed form solutions.

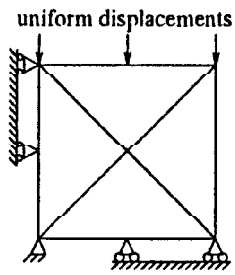

Figure 5.1: The mesh used in OXFEM for the verification of the non-linear elastic model in plane strain compression.

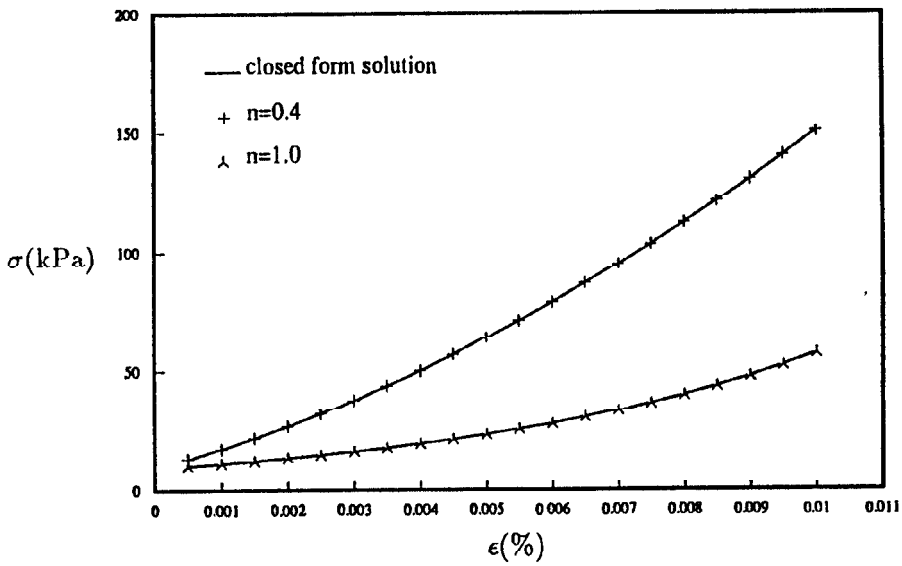

Figure 5.2: Results from OXFEM for plane strain compression using the non-linear elastic model with closed form solution superimposed.

5.5 Parametric Studies in Shallow Tunnelling

For the non-linear elastic model, the effect of varying n (the exponent that determines the influence of pressure on stiffness) on the prediction of settlement profiles due to tunnelling was investigated. This study followed a similar approach to that described in Chapter 4 for linear elastic and elastic-plastic soil models. In particular, the same three depths of tunnel axis (Z = 7.5, 10, 15m) were considered, corresponding to values of $\frac{Z}{D}$ of 1.5, 2.0 and 3.0. Five values of n ($n = 0.0, 0.3, 0.6, 0.9, 1.0$) were used. The value of k and g were chosen to give a value of Young's modulus E of 100MPa at a tunnel depth of 10m for a Poisson's ratio of 0.49. Figs. 5.3-5 show the settlement profiles for the each value of n for each of the three tunnel depths. It can be seen that surface heave occurs for $n \leq 0.9$. As n approaches 1.0, the upward displacements decrease, and when $n = 1$, settlements above the tunnel centreline are predicted. For $n = 0$, the settlement profiles are (as would be expected) the same as those obtained from the elastic homogeneous model (Fig. 4.7).

For $n = 1$, the stiffness is directly proportional to the stress level. From equation 5.3 and 5.4,

$$K = kp' \tag{5.21}$$

$$G = gp' \tag{5.22}$$

Initially, only in-situ stresses are present and so the elastic moduli profiles of the soil are the same as that for the linear elastic non-homogeneous model described in Section 4.2.2.2, but as the analysis proceeds the influence of non-linearity will be slightly diffrent from that of the elastic non-homogeneous

model. The results for the case of $n = 1$ in the model with stiffness dependent on pressure can be presented in dimensionless plots of $\frac{i}{D}$: $\frac{Z}{D}$, and $\frac{\delta_{max}G}{\gamma D^2}$: $\frac{Z}{D}$, where G is the initial shear modulus at the tunnel axis. The value of i was obtained following the same method as described in Chapter 4. Figs. 5.6 and 5.7 show the plots, with the results from linear elastic non-homogeneous model superimposed. For the non-linear elastic model, the maximum settlement δ_{max} and the width of the settlement trough i are smaller than those for the linear elastic non-homogeneous model. This difference is because in the non-linear model the elastic moduli are directly proportional to the current stress state and as the analysis used a large number of load steps, there is a continous correction of stiffness. For the linear elastic non-homogeneous model, stiffness is proportional to the original stress state (in-situ stresses). As a result - except for the case with the number of load steps equal to 1, which restricts the allowance for correction in stiffness for the non-linear model - the settlement profiles are different even if the initial stiffness profiles for the two models are identical.

5.6 Predicting Settlement Profiles Using the Non-linear Elastic Model

As shown Figs. 5.4-6, the non-linear elastic model with stiffness dependent on pressure is not suitable for the prediction of settlements in tunnelling problems since it predicts heaves for all cases except $n = 1$. The stress relief mechanism dominates and causes heaving. Plasticity is not taken into account. The main feature of the model is that stiffness increases with the current stress state. As a result, for small strain deformation, stiffness is low. The model is more suitable for problems where the stiffness increases with an increase in stress state.

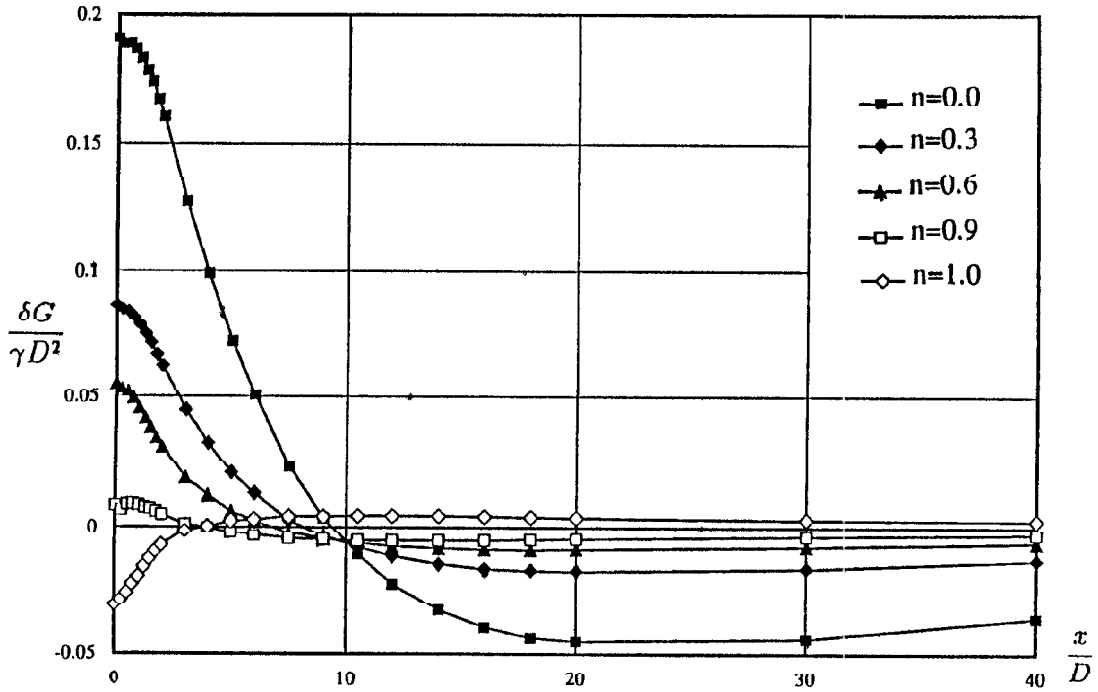

Figure 5.3: Surface displacements for non-linear elastic model, $\frac{z}{D} = 1.5$.

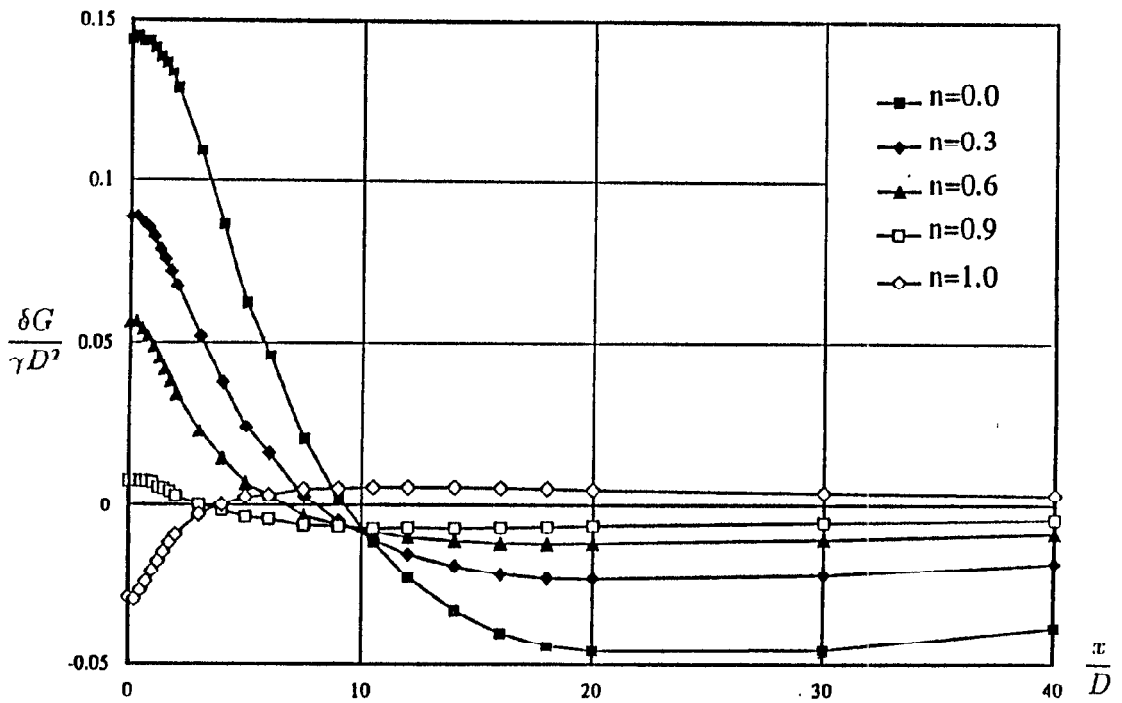

Figure 5.4: Surface displacements for non-linear elastic model, $\frac{z}{D} = 2.0$.

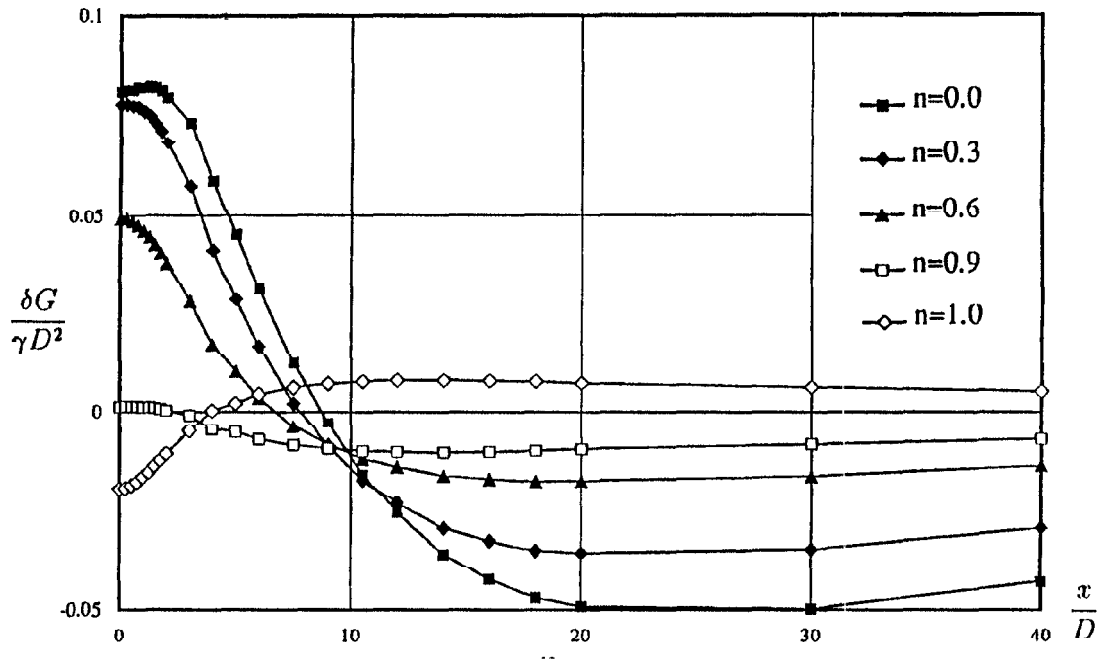

Figure 5.5: Surface displacements for non-linear elastic model, $\frac{Z}{D} = 3.0$.

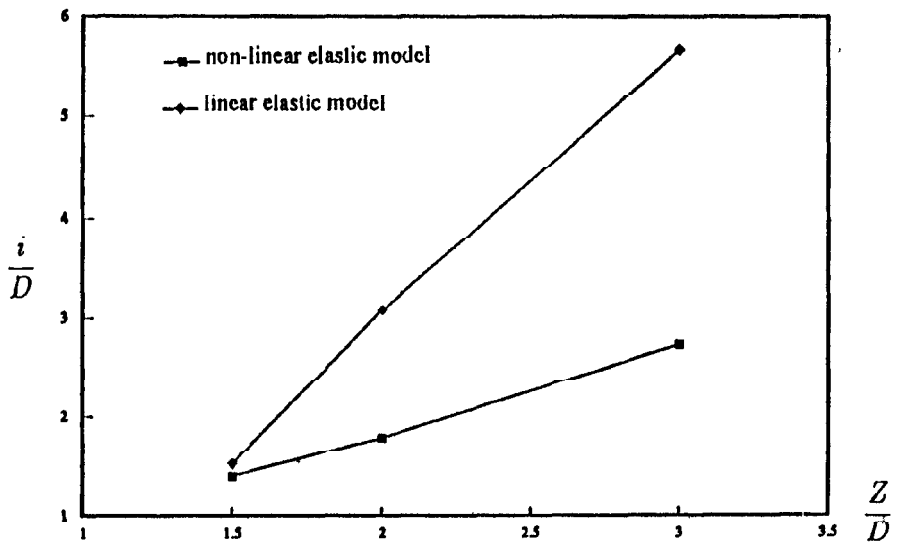

Figure 5.6: Dimensionless plot of $\frac{i}{D}$: $\frac{Z}{D}$ for the non-linear elastic model with $n = 1$.

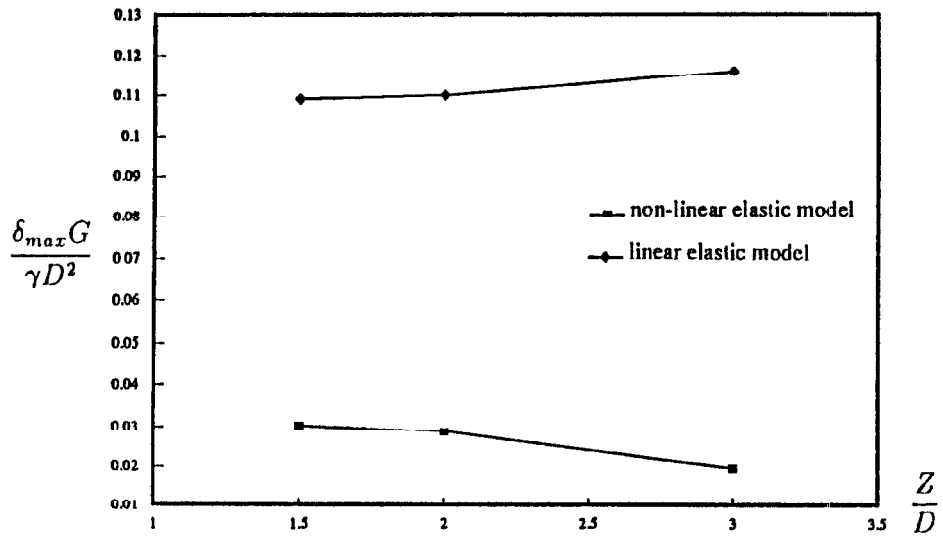

Figure 5.7: Dimensionless plot of $\frac{\delta_{max}G}{\gamma D^2}$: $\frac{Z}{D}$ for the non-linear elastic model with $n = 1$.

Chapter 6

THE NESTED YIELD LOCI MODEL

6.1 Introduction

Soil models must be chosen to suit the particular type of problem under consideration. It has been shown in Chapter 4 that linear elastic and elastic, perfectly-plastic models are not suitable for shallow tunnelling problems. In Chapter 5, the use of a non-linear elastic model in the finite element analysis of tunnelling has been investigated, and the analysis has showed that the non-linear elastic model is not capable of capturing the important feature of this type of problem.

This chapter contains a discussion of the use of a nested yield loci model in the finite element analysis of tunnelling. Such a model must be based on the concepts of the flow theory of plasticity, with modifications to incorporate experimental observations. Derivation of the mathematical formulations for the soil behaviour described by the model is discussed. The model has been implemented into OXFEM, and verification of the computer coding has been carried out.

Prevost (1979) proposed a model which describes the non-linear, anisotropic, elastoplastic, path-dependent stress-strain-strength properties of saturated soils. His model includes isotropic and kinematic plasticity, and can model any experimental hardening law by using nested yield surfaces. Elasticity was assumed to be isotropic and linear in shear. Shear non-linearity and anisotropy were shown to be a consequence of the generation of plastic strains. Elastic components of the strain rate tensor are related to the stress rate tensor by Hooke's law, where the shear modulus G is constant, and the bulk modulus K is a function of the effective mean normal stress. Successive kinematic yield surfaces are elliptical in shape in the axisymmetric stress plane ($\sigma_x = \sigma_y$), and can be translated in stress space by the stress point and to change size simultaneously. These nested surfaces are of different sizes to allow for the modelling of any hardening rule. The yield surfaces' initial positions and sizes reflect the past stress-strain history of the soil element. The normality rule of plasticity was applied to the nested yield surfaces, ie. the plastic strain rate vector lies along the exterior normal to the plastic potential surface. The outermost failure surface has its size, position, and movement as functions of the material's density and plastic volumetric strain history. An associated flow rule is used on this failure surface. All the yield surfaces may be translated in stress space by the stress point and they consecutively touch and push each other. Overlapping of surfaces is not allowed. The model was incorporated in a two dimensional finite element program by Prevost, and was applied to the analysis of the interaction of an offshore gravity structure with its soil foundation subjected to cyclic wave loading. Results were consistent with centrifuge tests results obtained by Rowe (1975).

The nested yield loci model that has been incorporated in OXFEM is a

similar but simpler elastic-plastic model to that proposed by Prevost (1979). Successive yield surfaces are in the shape of a von Mises yield surface in the stress space. Each surface can be translated in stress space by the stress point and the surfaces touch at the stress point. The outermost failure surface is represented by a von Mises yield surface, which is fixed in stress space. The sizes of the yield surfaces are governed by the hardening law used with the model. The initial positions of the yield surfaces are set up on the basis of the past stress-strain history of the soil. However, overlapping of the yield surfaces is permitted. The restriction of overlapping of the yield surfaces in Prevost's model was to ensure that the stress-strain response remained bilinear. For the nested model that has been implemented into OXFEM, although overlapping can result in multilinear state of the yield surfaces, under normal loading conditions of soil in the field, the state in which the surfaces are not nested is unlikely to occur. Therefore simpler mathematical formulations can be derived by not considering the restriction of the overlapping of the surfaces.

6.2 Formulation of Constitutive Equations

In this section, the formulation of the material stiffness matrix is discussed. To establish constitutive equations for an elastic-plastic model, assumptions are required about the following aspects of the behaviour of the soil:

1. Elastic behaviour

   (a) Description of elastic (recoverable) deformations.

2. Plastic behaviour

   (a) Definition of the boundary in stress space in which the deformations are elastic, ie. a yield surface.

(b) The mode of plastic deformation that occurs when the soil is yielding, ie. a plastic potential to specify the relative magnitudes of various components of plastic deformations.

(c) The way in which the absolute magnitude of the plastic deformation is linked with the changing size and positionof the yield locus, ie. a hardening rule to describe the change in the yield locus.

(d) The conditions under which failure occurs, ie. definition of the limiting surface in the stress space beyond which the stress state cannot be passed under any circumstances.

The derivation of constitutive equations for a general nested yield loci model is described below in a "step-by-step" fashion. The formulation follows closely the method set out in Houlsby & Chow (1994). The above assumptions are discussed for four cases which show increasing complexity of plasticity:

1. A single non work-hardening von Mises yield surface. (Note that this is simply a conventional elastic-perfectly plastic model.)
2. A single kinematic work-hardening yield locus.
3. Multiple kinematic work-hardening yield loci.
4. Multiple kinematic work-hardening yield loci with outer von Mises surface.

In the formulations of the four cases, the behaviour of the soil is decoupled into volumetric and deviatoric components. The deviators of stress and strains are defined as:

$$\sigma'_{ij} = \sigma_{ij} - \frac{1}{3}\sigma_{kk}\delta_{ij} \tag{6.1}$$

$$\epsilon'_{ij} = \epsilon_{ij} - \frac{1}{3}\epsilon_{kk}\delta_{ij} \tag{6.2}$$

The volumetric behaviour is always purely elastic. Therefore, the volumetric stress-strain relationship can be expressed as:

$$\dot{\sigma}_{kk} = 3K\dot{\epsilon}_{kk} \tag{6.3}$$

$$\dot{\epsilon}_{kk} = \frac{1}{3K}\dot{\sigma}_{kk} \tag{6.4}$$

Case 1: A single non work-hardening von Mises yield surface

From conventional plasticity theory, the strain rate can be separated into elastic and plastic components:

$$\dot{\epsilon}'_{ij} = \dot{\epsilon}'^{e}_{ij} + \dot{\epsilon}'^{p}_{ij} \tag{6.5}$$

where the superscripts e and p represent elastic and plastic components respectively.

Elastic behaviour

The change in stress is caused by the elastic strains only, and is governed by Hooke's law:

$$\dot{\sigma}'_{ij} = 2G\dot{\epsilon}'^{e}_{ij} \tag{6.6}$$

$$\dot{\epsilon}'^{e}_{ij} = \frac{1}{2G}\dot{\sigma}'_{ij} \tag{6.7}$$

Plastic behaviour

For the von Mises yield surface, an associated flow rule applies. The yield locus f and the plastic potential, g, can be expressed as:

$$f = g = \sigma'_{ij}\sigma'_{ij} - \frac{8c^2}{3} = 0 \tag{6.8}$$

where c is the shear strength of the soil. The differential form of the yield locus takes the form:

$$\dot{f} = \frac{\partial f}{\partial \sigma'_{ij}}\dot{\sigma}'_{ij} = 2\sigma'_{ij}\dot{\sigma}'_{ij} = 0 \tag{6.9}$$

The plastic strains can be expressed as:

$$\dot{\epsilon}'^{p}_{ij} = \Lambda \frac{\partial g}{\partial \sigma'_{ij}} = 2\Lambda \sigma'_{ij} \tag{6.10}$$

where Λ is a constant. Work-hardening is not taken into account for this failure surface.

To find the constant Λ, equations 6.7 and 6.10 are substituted into equation 6.5 so that:

$$\dot{\epsilon}'_{ij} = \frac{1}{2G}\dot{\sigma}'_{ij} + 2\Lambda \sigma'_{ij} \tag{6.11}$$

and

$$\sigma'_{ij}\dot{\epsilon}'_{ij} = \frac{1}{2G}\sigma'_{ij}\dot{\sigma}'_{ij} + 2\Lambda \sigma'_{ij}\sigma'_{ij} \tag{6.12}$$

From equation 6.9, $2\sigma'_{ij}\dot{\sigma}'_{ij} = 0$, therefore:

$$\sigma'_{ij}\dot{\epsilon}'_{ij} = 2\Lambda \sigma'_{ij}\sigma'_{ij} \tag{6.13}$$

Using equation 6.8 we obtain the value of Λ:

$$\Lambda = \frac{3}{16c^2}\sigma'_{ij}\dot{\epsilon}'_{ij} \tag{6.14}$$

Substituting the value of Λ into equation 6.10, and using equations 6.2, 6.5 and 6.6, we obtain:

$$\dot{\sigma}'_{ij} = 2G\dot{\epsilon}'_{ij} - 2G\frac{3}{8c^2}\sigma'_{ij}\sigma'_{kl}\dot{\epsilon}'_{kl} \tag{6.15}$$

Equation 6.15 can be re-written as:

$$\dot{\sigma}'_{ij} = 2G\left[\delta_{ik}\delta_{jl} - \frac{3}{8c^2}\sigma'_{ij}\sigma'_{kl}\right]\dot{\epsilon}'_{kl} \tag{6.16}$$

Equation 6.16 is the most convenient form of the stiffness matrix. Since the stiffness matrix is singular (because the material is perfectly plastic) it can not be inverted to give a compliance matrix.

Case 2: A single kinematic work-hardening yield locus

As in case 1, the total strain is decoupled into elastic and plastic components:

$$\dot{\epsilon}'_{ij} = \dot{\epsilon}'^{e}_{ij} + \dot{\epsilon}'^{p}_{ij} \tag{6.17}$$

Elastic behaviour

The stress increment is related to elastic strain increment only.

$$\dot{\sigma}'_{ij} = 2G\dot{\epsilon}'^{e}_{ij} \tag{6.18}$$

$$\dot{\epsilon}'^{e}_{ij} = \frac{1}{2G}\dot{\sigma}'_{ij} \tag{6.19}$$

Plastic behaviour

The yield locus and the associated flow rule can be expressed in terms of the location of the centre of the yield locus σ'^{o}_{ij}:

$$f = g = (\sigma'_{ij} - \sigma'^{o}_{ij})(\sigma'_{ij} - \sigma'^{o}_{ij}) - \frac{8c^2}{3} = 0 \tag{6.20}$$

Expressing the yield locus in differential form, we obtain:

$$\dot{f} = \frac{\partial f}{\partial \sigma'_{ij}}\dot{\sigma}'_{ij} + \frac{\partial f}{\partial \sigma'^{o}_{ij}}\dot{\sigma}'^{o}_{ij} = 2(\sigma'_{ij} - \sigma'^{o}_{ij})(\dot{\sigma}'_{ij} - \dot{\sigma}'^{o}_{ij}) = 0 \tag{6.21}$$

The direction of the plastic strain increment is independent of the direction of the stress increment and is given by the normal to the plastic potential. The plastic strains take the form:

$$\dot{\epsilon}'^{p}_{ij} = \lambda\frac{\partial g}{\partial \sigma'_{ij}}\frac{\partial f}{\partial \sigma'_{kl}}\dot{\sigma}'_{kl} = 4\lambda(\sigma'_{ij} - \sigma'^{o}_{ij})(\sigma'_{kl} - \sigma'^{o}_{kl})\dot{\sigma}'_{kl} \tag{6.22}$$

where λ is a constant, and the $\dot{\sigma}'_{kl}$ ensures incremental linearity of the plastic strain increment. The magnitude of the plastic strain increment is related by a hardening law to the movement of the yield locus. The strain-hardening relationship is assumed linear, and the kinematic yield surface moves in the direction of the plastic strain increment:

$$\dot{\sigma}'^{o}_{ij} = 2h\dot{\epsilon}'^{p}_{ij} \tag{6.23}$$

$$\dot{\epsilon}'^{p}_{ij} = \frac{1}{2h}\dot{\sigma}'^{o}_{ij} \tag{6.24}$$

where h is a strain-hardening parameter.

To obtain an expression for the constant λ, equation 6.24 is back substituted to equation 6.22, giving:

$$\frac{\sigma'^{o}_{ij}}{2h} = 4\lambda(\sigma'_{ij} - \sigma'^{o}_{ij})(\sigma'_{kl} - \sigma'^{o}_{kl})\dot{\sigma}'_{kl} \tag{6.25}$$

Multiplying both sides of equation 6.25 by $(\sigma'_{ij} - \sigma'^{o}_{ij})$ and using equation 6.20, we obtain:

$$\lambda = \frac{3}{64c^2h} \tag{6.26}$$

Substituting equations 6.19, 6.22, and 6.26 into 6.17 gives:

$$\dot{\epsilon}'_{ij} = \frac{1}{2G}\dot{\sigma}'_{ij} + \frac{3}{8c^2}(\sigma'_{ij} - \sigma'^{o}_{ij})(\sigma'_{kl} - \sigma'^{o}_{kl})\frac{1}{2h}\dot{\sigma}'_{kl} \tag{6.27}$$

which can be re-written as:

$$\dot{\epsilon}'_{ij} = \frac{1}{2G}\left[\delta_{ik}\delta_{jl} + \frac{3}{8c^2}(\sigma'_{ij} - \sigma'^{o}_{ij})(\sigma'_{kl} - \sigma'^{o}_{kl})\frac{G}{h}\right]\dot{\sigma}'_{kl} \tag{6.28}$$

This is the most convenient form of the compliance matrix. Equation 6.28 can be inverted to give the stiffness matrix:

$$\dot{\sigma}'_{ij} = 2G\left[\delta_{ik}\delta_{jl} - \frac{3}{8c^2}(\sigma'_{ij} - \sigma'^{o}_{ij})(\sigma'_{kl} - \sigma'^{o}_{kl})\frac{G}{G+h}\right]\dot{e}_{kl} \tag{6.29}$$

Note that for $h = 0$ equation 6.29 reduces to the same as equation 6.16, ie. elastic-perfectly plastic with a single von Mises yield surface. However, the compliance matrix cannot be obtained for this case. For $h = \infty$, equation 6.29 reduces to a purely elastic model (equation 6.18). The evolution rule for the internal variables σ^0_{ij} can easily be derived by substituting the value of λ into equation 6.25:

$$\dot{\sigma}'^{o}_{ij} = \frac{3}{8c^2}(\sigma'_{ij} - \sigma'^{o}_{ij})(\sigma'_{kl} - \sigma'^{o}_{kl})\dot{\sigma}'_{kl} \tag{6.30}$$

Case 3: Multiple kinematic work-hardening yield loci

For a model with multiple kinematic work-hardening yield loci, the total plastic strains will be the sum of the contribution of each yield surface:

$$\dot{\epsilon}'_{ij} = \dot{\epsilon}'^{e}_{ij} + \sum_{n} \dot{\epsilon}'^{pi}_{ij} \tag{6.31}$$

Elastic behaviour

The elastic behaviour is the same as in Case 1 and 2:

$$\dot{\sigma}'_{ij} = 2G\dot{\epsilon}'^{e}_{ij} \tag{6.32}$$

$$\dot{\epsilon}'^{e}_{ij} = \frac{1}{2G}\dot{\sigma}'_{ij} \tag{6.33}$$

Plastic behaviour

The yield loci and associated flow rules in terms of the location of the centres of the yield loci σ'^{oi}_{ij} will be:

$$f_i = g_i = (\sigma'_{ij} - \sigma'^{oi}_{ij})(\sigma'_{ij} - \sigma'^{oi}_{ij}) - \frac{8c_i^2}{3} = 0 \tag{6.34}$$

Expressing the yield loci in differential form, we obtain:

$$\dot{f}_i = \frac{\partial f_i}{\partial \sigma'_{ij}}\dot{\sigma}'_{ij} + \frac{\partial f_i}{\partial \sigma'^{oi}_{ij}}\dot{\sigma}'^{oi}_{ij} = 2(\sigma'_{ij} - \sigma'^{oi}_{ij})(\dot{\sigma}'_{ij} - \dot{\sigma}'^{oi}_{ij}) = 0 \tag{6.35}$$

As in the case with a single kinematic work-hardening surface (Case 2), the plastic strains can be expressed as:

$$\dot{\epsilon}'^{pi}_{ij} = \lambda_i \frac{\partial g_i}{\partial \sigma'_{ij}}\frac{\partial f_i}{\partial \sigma'_{kl}}\dot{\sigma}'_{kl} = 4\lambda_i(\sigma'_{ij} - \sigma'^{oi}_{ij})(\sigma'_{kl} - \sigma'^{oi}_{kl})\dot{\sigma}'_{kl} \tag{6.36}$$

and the strain-hardening relationship for each yield locus takes the form:

$$\dot{\sigma}'^{oi}_{ij} = 2h_i\dot{\epsilon}'^{pi}_{ij} \tag{6.37}$$

where h_i is the strain-hardening parameter i^{th}work-hardening surface.

Equations 6.34, 6.36 and 6.37 can be manipulated to give the value of λ_i:

$$\lambda_i = \frac{3}{64c_i^2 h_i} \tag{6.38}$$

Substituting for λ_i into equation 6.36 gives an expression for the plastic strain increments can thus be obtained:

$$\dot{\epsilon}'^{pi}_{ij} = \frac{3}{16c_i^2 h_i}(\sigma'_{ij} - \sigma'^{oi}_{ij})(\sigma'_{kl} - \sigma'^{oi}_{kl})\dot{\sigma}'_{kl} \tag{6.39}$$

Using the expressions obtained for $\dot{\epsilon}'^{e}_{ij}$ (equation 6.33) and $\dot{\epsilon}'^{pi}_{ij}$ (equation 6.39), the total strain increment can be expressed as:

$$\dot{\sigma}'_{ij} + \sum_n \frac{3G}{8c_i^2 h_i}(\sigma'_{ij} - \sigma'^{oi}_{ij})(\sigma'_{kl} - \sigma'^{oi}_{kl})\dot{\sigma}'_{kl} = 2G\dot{\epsilon}'_{ij} \tag{6.40}$$

or

$$\dot{\epsilon}'_{ij} - \frac{1}{2G}\dot{\sigma}'_{ij} + \sum_n \frac{3}{8c_i^2}(\sigma'_{ij} - \sigma'^{oi}_{ij})(\sigma'_{kl} - \sigma'^{oi}_{kl})\frac{1}{2h_i}\dot{\sigma}'_{kl} \tag{6.41}$$

Equation 6.41 can also be written as:

$$\dot{\epsilon}'_{ij} = \frac{1}{2G}\left[\delta_{ik}\delta_{jl} + \sum_n \frac{3}{8c_i^2}(\sigma'_{ij} - \sigma'^{oi}_{ij})(\sigma'_{kl} - \sigma'^{oi}_{kl})\frac{G}{h_i}\right]\dot{\sigma}'_{kl} \tag{6.42}$$

and is the most conveninent form of the compliance matrix. The compliance matrix can be inverted numerically (but not analytically) to give the corresponding stiffness matrix. The evolution rules for the internal variables can be expressed as:

$$\dot{\sigma}'^{oi}_{ij} = \frac{3}{8c_i^2}(\sigma'_{ij} - \sigma'^{oi}_{ij})(\sigma'_{kl} - \sigma'^{oi}_{kl})\dot{\sigma}'_{kl} \tag{6.43}$$

Case 4: Multiple kinematic work-hardening yield loci with outer von Mises surface

In the case of multiple work-hardening yield loci with an outer von Mises surface, the total plastic strains increments will be the sum of the plastic strain increments of each work-hardening locus, and those of the outer von Mises surface.

$$\dot{\epsilon}'_{ij} = \dot{\epsilon}'^{e}_{ij} + \sum_{n} \dot{\epsilon}'^{pi}_{ij} + \dot{\epsilon}'^{p}_{ij} \tag{6.44}$$

Elastic behaviour

The elastic behaviour is described by equation 6.45 and 6.46:

$$\dot{\sigma}'_{ij} = 2G\dot{\epsilon}'^{e}_{ij} \tag{6.45}$$

$$\dot{\epsilon}'^{e}_{ij} = \frac{1}{2G}\dot{\sigma}'_{ij} \tag{6.46}$$

Plastic behaviour

The plastic behaviour is a combination of that from the nested yield surfaces and the outer von Mises surface.

For the nested yield surfaces, the yield loci and associated flow rules for the multiple work-hardening yield loci can be expressed in terms of the location of the centres of the yield loci, σ'^{oi}_{ij}, as:

$$f_i = g_i = (\sigma'_{ij} - \sigma'^{oi}_{ij})(\sigma'_{ij} - \sigma'^{oi}_{ij}) - \frac{8c_i^2}{3} = 0 \tag{6.47}$$

and the differential form of the yield loci as:

$$\dot{f}_i = \frac{\partial f_i}{\partial \sigma'_{ij}}\dot{\sigma}'_{ij} + \frac{\partial f_i}{\partial \sigma'^{oi}_{ij}}\dot{\sigma}'^{oi}_{ij} = 2(\sigma'_{ij} - \sigma'^{oi}_{ij})(\dot{\sigma}'_{ij} - \dot{\sigma}'^{oi}_{ij}) = 0 \tag{6.48}$$

The plastic strains take the form:

$$\dot{\epsilon}'^{pi}_{ij} = \lambda_i \frac{\partial g_i}{\partial \sigma'_{ij}} \frac{\partial f_i}{\partial \sigma'_{kl}}\dot{\sigma}'_{kl} = 4\lambda_i(\sigma'_{ij} - \sigma'^{oi}_{ij})(\sigma'_{kl} - \sigma'^{oi}_{kl})\dot{\sigma}'_{kl} \tag{6.49}$$

As in case 3, the strain-hardening relationship for each yield surface is:

$$\dot{\sigma}'^{oi}_{ij} = 2h_i \dot{\epsilon}'^{pi}_{ij} \tag{6.50}$$

Equations 6.47-50 can be manipulated to give:

$$\lambda_i = \frac{3}{64c_i^2 h_i} \tag{6.51}$$

and an expression for the plastic strain increment of each nested yield surface obtained:

$$\dot{\epsilon}'^{pi}_{ij} = \frac{3}{16c_i^2 h_i}(\sigma'_{ij} - \sigma'^{oi}_{ij})(\sigma'_{kl} - \sigma'^{oi}_{kl})\dot{\sigma}'_{kl} \tag{6.52}$$

For the outer von Mises surface, the yield locus and associated flow rule take the form:

$$f = g = \sigma'_{ij}\sigma'_{ij} - \frac{8c^2}{3} = 0 \tag{6.53}$$

The differential form of this surface is given by:

$$\dot{f} = \frac{\partial f}{\partial \sigma'_{ij}}\dot{\sigma}'_{ij} = 2\sigma'_{ij}\dot{\sigma}'_{ij} = 0 \tag{6.54}$$

There is no work-hardening effect on this surface, and the plastic strains can be expressed as:

$$\dot{\epsilon}'^{p}_{ij} = \Lambda \frac{\partial g}{\partial \sigma'_{ij}} = 2\Lambda\sigma'_{ij} \tag{6.55}$$

To obtain an expression for Λ, equations 6.46, 6.52 and 6.55 are substituted into equation 6.44, giving

$$\dot{\epsilon}'_{ij} = \frac{\dot{\sigma}'_{ij}}{2G} + \sum_n \frac{3G}{16c_i^2 h_i}(\sigma'_{ij} - \sigma'^{oi}_{ij})(\sigma'_{kl} - \sigma'^{oi}_{kl})\dot{\sigma}'_{kl} + 2\Lambda\sigma'_{ij} \tag{6.56}$$

Multiply both sides by σ'_{ij}, and using equation 6.53, we obtain:

$$\sigma'_{ij}\dot{\epsilon}'_{ij} = \sum_n \frac{3G}{16c_i^2 h_i}(\sigma'_{ij} - \sigma'^{oi}_{ij})\sigma'_{ij}(\sigma'_{kl} - \sigma'^{oi}_{kl})\dot{\sigma}'_{kl} + 2\Lambda\frac{8c^2}{3} \tag{6.57}$$

Thus, Λ can be expressed as:

$$\Lambda = \frac{3}{16c^2}\left[\sigma'_{ij}\dot{\epsilon}'_{ij} - \sum_n \frac{3}{8c_i^2}\frac{1}{2h_i}(\sigma'_{ij} - \sigma'^{oi}_{ij})\sigma'_{ij}(\sigma'_{kl} - \sigma'^{oi}_{kl})\dot{\sigma}'_{kl}\right] \qquad (6.58)$$

Note that equation 6.58 gives a different expression for Λ than for the case of a single von Mises surface (Case 1, equation 6.14). Substituting Λ into equation 6.56, we obtain the relationship between stress and strain rate:

$$\dot{\sigma}'_{ij} + \sum_n \frac{3G}{8c_i^2 h_i}(\sigma'_{ij} - \sigma'^{oi}_{ij})(\sigma'_{kl} - \sigma'^{oi}_{kl})\dot{\sigma}'_{kl} - \sum_n \frac{9G}{64c^2c_i^2h_i}\sigma'_{ij}(\sigma'_{mn} - \sigma'^{oi}_{mn})\sigma'_{mn}(\sigma'_{kl} - \sigma'^{oi}_{kl})\dot{\sigma}'_{kl}$$
$$= 2G\dot{\epsilon}'_{ij} - 2G\frac{3}{8c^2}\sigma'_{ij}\sigma'_{kl}\dot{\epsilon}'_{kl} \qquad (6.59)$$

Equation 6.59 can be manipulated to give:

$$\left[\delta_{ip}\delta_{jq} + \sum_n \frac{3G}{8c_i^2 h_i}(\sigma'_{ij} - \sigma'^{oi}_{ij})(\sigma'_{pq} - \sigma'^{oi}_{pq}) - \sum_n \frac{9G}{64c^2c_i^2h_i}\sigma'_{ij}(\sigma'_{mn} - \sigma'^{oi}_{mn})\sigma'_{mn}(\sigma'_{pq} - \sigma'^{oi}_{pq})\right]\dot{\sigma}'_{pq}$$
$$= 2G\left[\delta_{ik}\delta_{jl} - \frac{3}{8c^2}\sigma'_{ij}\sigma'_{kl}\right]\dot{\epsilon}'_{kl} \qquad (6.60)$$

Although the matrix on the right hand side of equation 6.60 is singular and cannot be inverted, the matrix on the left hand side is non-singular. It can be inverted numerically and multiplied into the right hand side to give the stiffness matrix. The compliance matrix cannot be obtained because the outermost yield locus is perfectly plastic.

The evolution rules for the internal variables are again needed, and these are:

$$\dot{\sigma}'^{oi}_{ij} = \frac{3}{8c_i^2}(\sigma'_{ij} - \sigma'^{oi}_{ij})(\sigma'_{kl} - \sigma'^{oi}_{kl})\dot{\sigma}'_{kl} \qquad (6.61)$$

Equation 6.60 and 6.61 may be slightly simplified by noting that $\sigma'_{kl}\dot{\sigma}'_{kl} = 0$.

6.3 Implementation of the Model in OXFEM

The implementation of the nested yield loci model requires the following actions:

1. Establish consistency between the initial positions of each yield surface and the in-situ stress state.
2. Evaluate the number of nested yield surfaces activated by the stress increment. The material stiffness matrix is then calculated accordingly.
3. Formulate procedures to update Gauss point stresses after each iteration of load step. The stress states are checked against the failure criteria, in this case specified by the outer von Mises surface.
4. Update the positions of yield surfaces to correspond to the updated stress state for each Gauss point. The updated states are checked to ensure the consistency of the states with the model is maintained.

The nested yield loci model was incorporated in the program DRIVE by Prof. Guy Houlsby to produce the stress-strain response for a single point in stress space under various loading conditions. The code written for the implementation of the model in OXFEM was based on the program DRIVE.

DRIVE calculates the material stiffness matrix and the corresponding stresses and states under a specified loading condition. Before the material stiffness is calculated, the number of nested surface activated is evaluated. This is achieved by comparing the position of the current stress point with the positions of the centres of the inner yield surface. If the stress point lies outside the inner surface, it is activated and translated in the direction of

the stress increment. The material stiffness is calculated using equation 6.60 according to the number of mobilised yield surfaces. Stresses are checked against failure load governed by the von Mises surface. Both elastic and plastic stress updating procedures are available. The plastic stress updating procedure is used when at least one yield surface is activated. States for each yield surface are calculated accordingly.

The program DRIVE was modified to the format used by OXFEM. Adjustment of positions of yield surfaces takes place at the beginning of the analysis to ensure consistency with the in-situ stresses. Thus the stress-strain history is recorded, and this information can be used in subsequent calculations in the program. The material stiffness matrix is calculated and stresses updated as in DRIVE. The new positions of the yield surfaces are then calculated.

6.4 Verification of the Model

Verification of the model was achieved in three stages:

1. Two simple tests were carried out using the program DRIVE to indicate qualitatively that the nested yield loci model could predict hysteresis effects and the dependency of stiffness on past stress history of the soil.
2. A plane strain shear problem was used to check the results from DRIVE against the closed form solutions.
3. Plane strain shear analysis was carried out using DRIVE and OXFEM, and their results compared. Since DRIVE did not involve finite element analysis, the accuracy of implementation in OXFEM could be investigated.

Stage 1

The program DRIVE was used to predict the stress-strain relationship for soil undergoing continuous unloading and reloading. The stress path used in the analysis is shown in Fig. 6.1. A total number of ten yield surfaces were used and the results were plotted as deviator stress q against shear strain ϵ_q (Fig. 6.2). A hysteresis effect was produced giving stiff response when the load is reduced below a previous maximum value.

Another analysis was carried out to test the ability of the model to describe the path-dependent stress-strain property of soil. A specified state in the stress space was approached via three different stress paths, as shown in Fig. 6.3. The corresponding stress-strain curves are shown in Fig. 6.4. The results show a delay in achieving a constant stress state when the direction of strain differs from the previous path. A reversal in direction of strain (PATH 1) produces the highest initial stiffness, which gradually reduces. Continuation of the strain in the direction of the previous stress path (PATH 3) produces the least stiff initial response.

The above predicted results can be explained in terms of the nested yield loci model (Fig. 6.5). A change in the direction of strain means an immediate elastic response because the stress point moves away from the inner yield surfaces, into the purely elastic region. Once the inner yield surfaces are activated, plastic deformation takes place, and the soil is work hardened, causing a reduction in the soil stiffness.

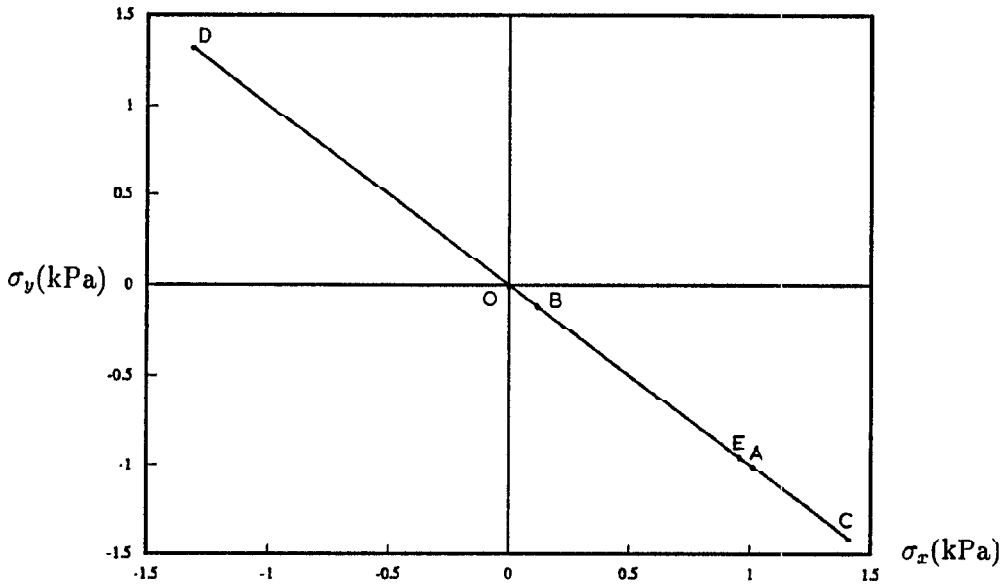

Figure 6.1: Stress path used in the analysis to produce hysteresis effect.

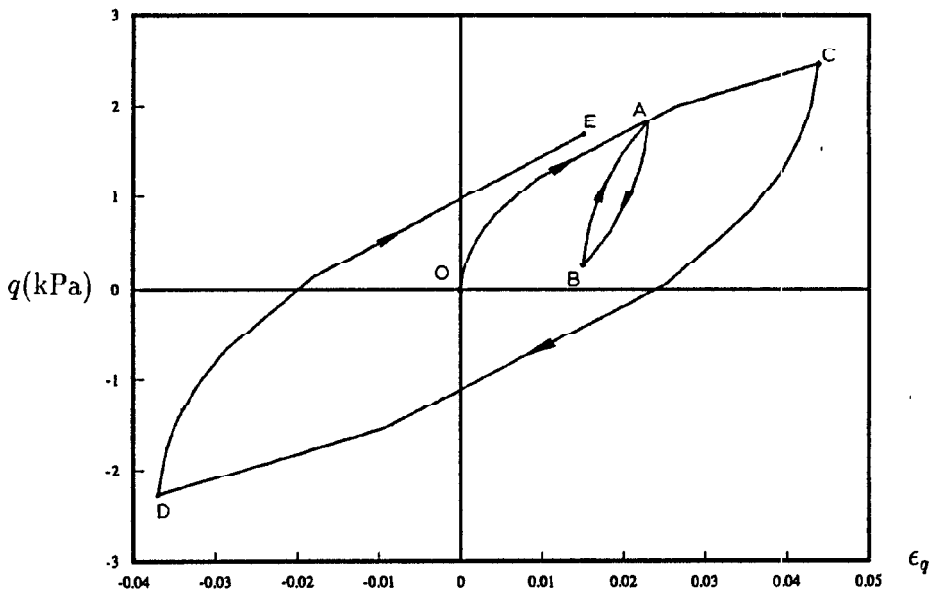

Figure 6.2: Hystersis loop produced by using the nested yield loci model on unloading and reloading of soil.

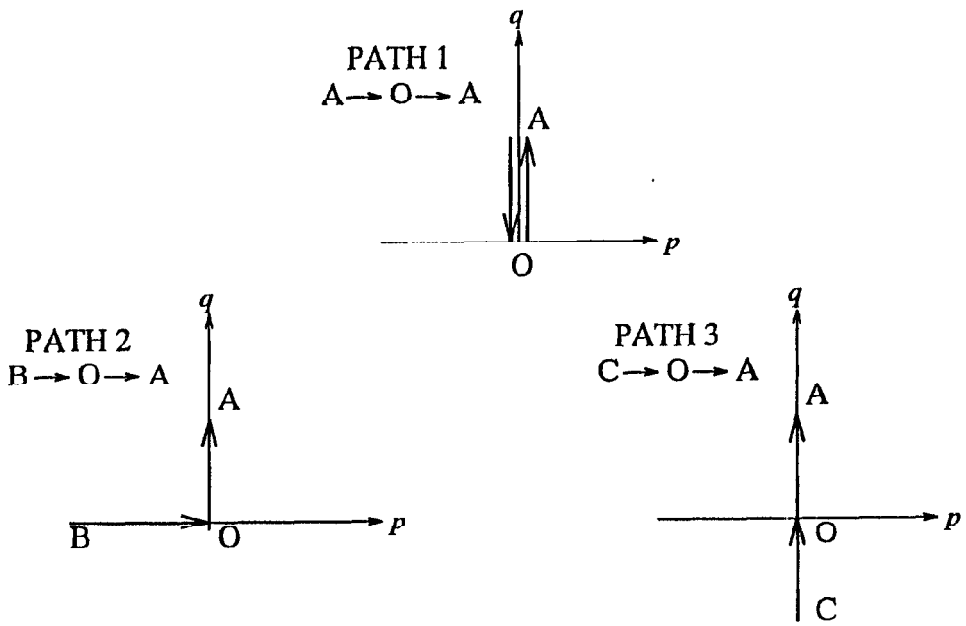

Figure 6.3: Stress paths used in the examination of the ability of the nested yield loci model in the prediction of the dependency of stiffness on the past stress history.

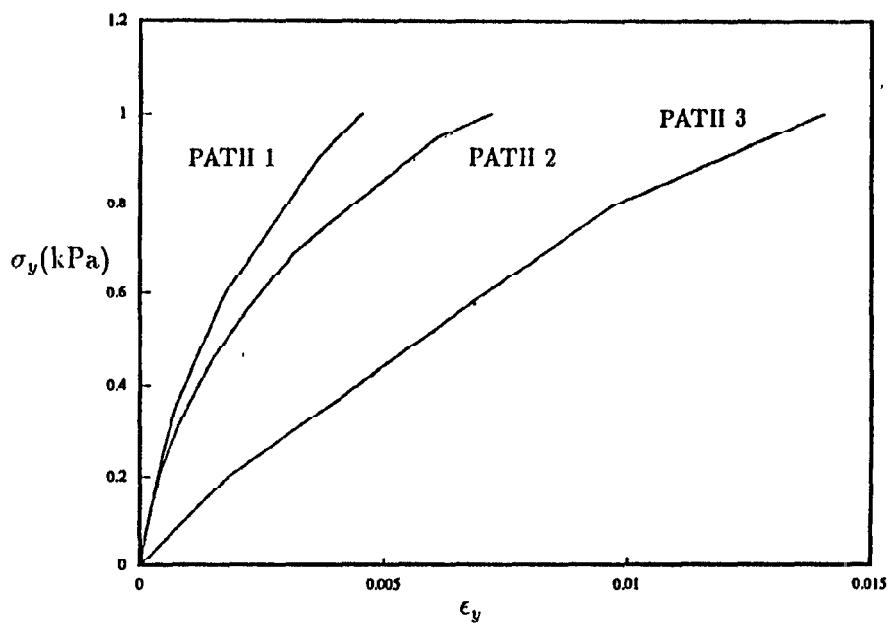

Figure 6.4: Stress-strain curves for the nested yield loci model with three different stress history.

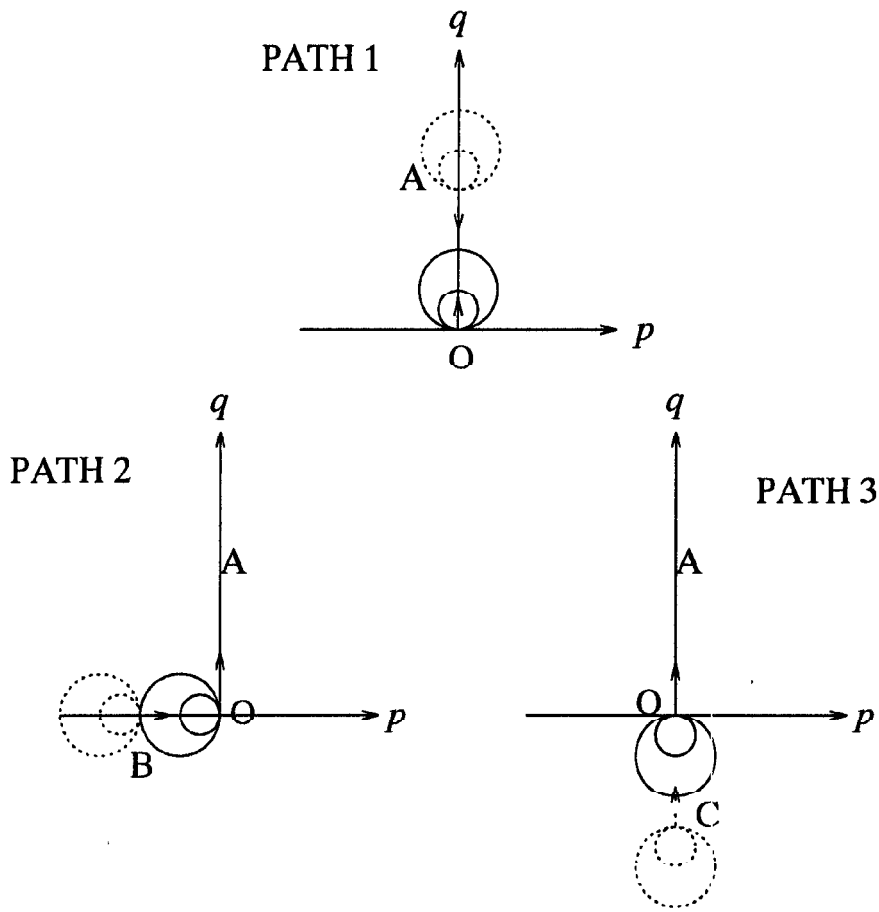

Figure 6.5: Simplified movements of inner yield surfaces for three different stress paths.

Stage 2

Computer coding for the nested yield loci model was checked against the closed form solutions for an element under pure shear deformation. To reduce the complexity of the closed form solutions only one work-hardening surface was considered. This situation is equivalent to Case 2 described in the preceeding section (6.2). For an element under the application of a shear strain $\dot{\gamma} = 2\dot{\epsilon}_{12}$, the induced shear stress $\dot{\tau} = \dot{\sigma}'_{12}$ can be deduced from equation 6.29:

$$\dot{\tau} = \dot{\sigma}'_{12} = G\left[1 - \frac{3}{8c^2}(\sigma'_{12} - \sigma'^{0}_{12})(\sigma'_{12} - \sigma'^{0}_{12})\frac{G}{G+h}\right]\dot{\gamma} \qquad (6.62)$$

Before the work-hardening surface is activated, the behaviour of the element is purely elastic:

$$\dot{\tau} = G\dot{\gamma} \qquad (6.63)$$

The stress state which causes the mobilisation of the work-hardening surface can be deduced from equation 6.20, giving:

$$(\sigma_{12} - \sigma'^{0}_{12})(\sigma_{12} - \sigma'^{0}_{12}) = \frac{8c^2}{3} \qquad (6.64)$$

Therefore, once the work-hardening surface is activated, the relationship of the shear stress and shear strain for this case becomes:

$$\begin{aligned} \dot{\tau} &= G\left[1 - \frac{G}{G+h}\right]\dot{\gamma} \\ &= \frac{Gh}{G+h}\dot{\gamma} \end{aligned} \qquad (6.65)$$

The results are represented graphically in Fig. 6.6.

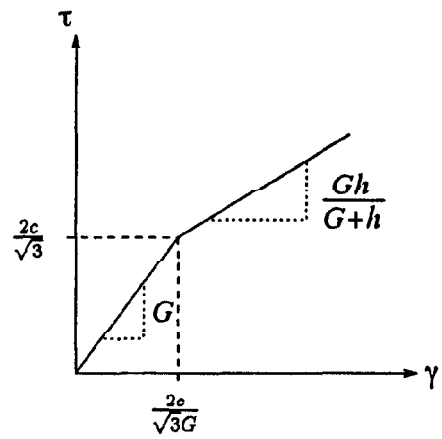

Figure 6.6: Closed form solution for a pure shear problem for the nested yield loci model with one work-hardening surface.

In the analysis, a shear strain γ of 0.08% was used. The material properties were chosen arbitarily, and are listed in Table 6.1.

G	$200kPa$
K	$1000kPa$
h	$200kPa$
c	$0.05kPa$

Table 6.1: Material properties used in the verification of the program DRIVE using closed form solutions.

The results obtained from DRIVE are shown in Fig. 6.7, with the closed form solution superimposed. The computed results and the closed form solutions are almost identical.

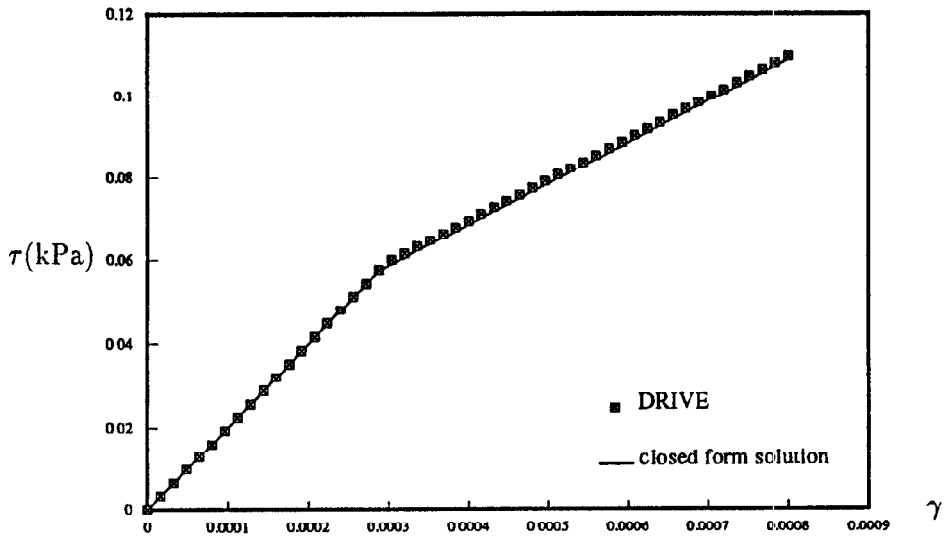

Figure 6.7: Results for test problem in pure shear from DRIVE, with closed form solution superimposed.

Stage 3

Plane strain shear analysis was carried out using DRIVE and OXFEM. The mesh used in OXFEM is shown in Fig. 6.8. The base of the mesh is restricted from vertical movement. Horizontal displacements were applied to all the nodes except those at the base of the mesh. The magnitude of prescribed horizontal displacements increased linearly with increasing vertical distance from the base. Ten yield surfaces were used in the analysis and the properties of the yield surfaces were provided by Prof. Guy Houlsby through curve fitting of stiffness plots for Todi Clay. The material properties are presented as:

$$h_f = \frac{h_i}{G_0} \tag{6.66}$$

$$c_f = \frac{c_i}{c} \tag{6.67}$$

where G_0 is the shear stiffness of the outer von Mises surface. The values of h_f and c_f used in this analysis are shown in Table 6.2. The values of G_0=33557kPa, and c=100kPa were used in this analysis.

Yield Surface	$h_f = \frac{h_i}{G_0}$	$c_f = \frac{c_i}{c}$
1	10	0.02
2	3.0	0.04
3	1.0	0.06
4	0.8	0.1
5	0.6	0.15
6	0.4	0.2
7	0.2	0.3
8	0.1	0.5
9	0.05	0.7
10	1.0	1.0

Table 6.2: Material properties used for the analysis using ten nested yield surface.

The results from OXFEM and DRIVE are shown in Fig. 6.9. The response of the soil predicted by OXFEM agreed closely with DRIVE's prediction.

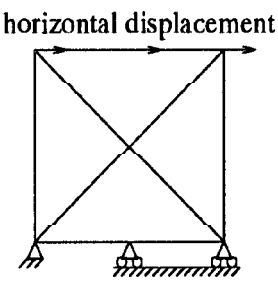

Figure 6.8: Mesh used in OXFEM for the test problem in pure shear for the nested yield loci model.

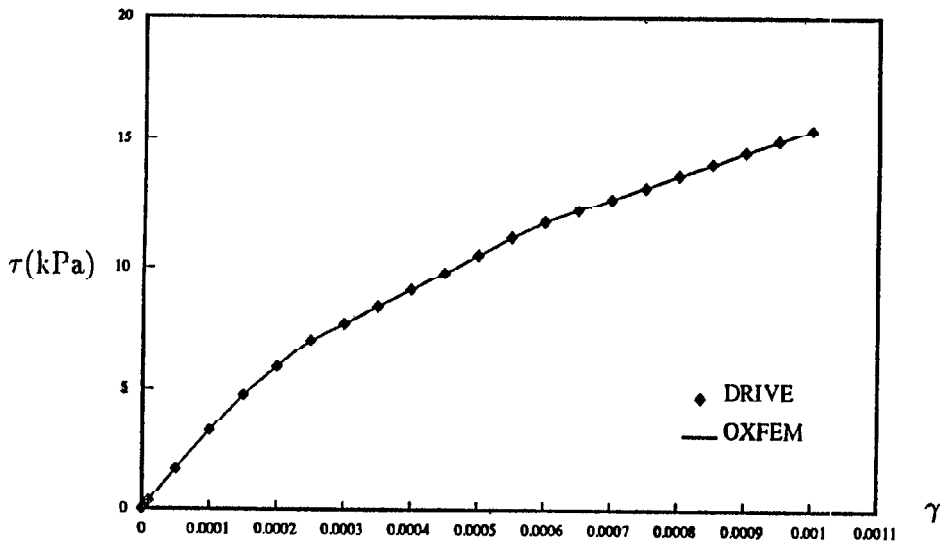

Figure 6.9: Results from DRIVE and OXFEM for a pure shear problem.

6.5 Parametric Studies on Tunnelling

As for other parametric studies described in this thesis, three depths of tunnel axis were considered (Chapter 4). The self weight of soil, γ, was taken as 20kPa/m. A total number of ten surfaces were used for the model. The properties of the ten surfaces were the same as those listed in Table 6.2.

Two features of interest were investigated:

1. The undrained shear strength.
2. The stiffness within each yield surface.

The values of undrained shear strength s_u at the outer von Mises surface (or cohesion c as used in the derivation of the constitutive equations of the model) were chosen to be the same as those used in the parametric studies of

linear elastic-plastic models (Table 4.1). The corresponding cohesion of each inner yield surface, c_i (=cc_f), was adjusted accordingly, keeping c_f constant for all c. The values of c_f for the ten surfaces are shown in Table 6.2.

The shear stiffness was modelled using two different ways:

1. By matching the initial shear stiffness (G_0) of the model with the shear stiffness of a linear elastic-plastic homogeneous soil as assumed for London clay.
2. By matching the secant stiffness at 50% of the maximum shear stress (G_{50}) with the shear stiffness of the linear elastic-plastic homogeneous soil as assumed for London clay.

The values of $h_f = \frac{h_1}{G_o}$ were constant in the parametric studies. For the G_{50} case, the value of the G_0 is found by multiplying G_{50} for the particular soil with an appropriate factor. In this case:

$$G_{50} = 0.078 G_0 \tag{6.68}$$

The shear stiffness of the elastic-plastic homogeneous model was taken to be 33557kPa for London clay (Chapter 4) giving the values of G_0 for the the two cases are:

Case 1. G_0= 33557kPa

Case 2. G_0= 430218kPa

The soil parameters used in each analysis are summarised in Table 6.3-4.

The results obtained from OXFEM for Case 1 and 2 are presented in dimensionless form in Figs. 6.10-13. Figs. 6.10-12 show plots of $\frac{\delta G_0}{\gamma D^2}$: $\frac{x}{D}$,

Nested yield loci model: Case 1									
Z (m)	7.5			10			15		
$\frac{Z}{D}$	1.5			2.0			3.0		
G_0 (kpa)	33557			33557			33557		
$s_u = c$ (kPa)	45	60	75	60	80	100	90	120	150
$\frac{s_u}{\gamma Z}$	0.3	0.4	0.5	0.3	0.4	0.5	0.3	0.4	0.5
reference	1.5n3g0	1.5n4g0	1.5n4g0	2n3g0	2n4g0	2n5g0	3n3g0	3n4g0	3n5g0

Table 6.3: Soil properties used for parametric studies using nested yield loci model (Case 1).

Nested yield loci model: Case 2									
Z (m)	7.5			10			15		
$\frac{Z}{D}$	1.5			2.0			3.0		
G_0 (kpa)	430218			430218			430218		
$s_u = c$ (kPa)	45	60	75	60	80	100	90	120	150
$\frac{s_u}{\gamma Z}$	0.3	0.4	0.5	0.3	0.4	0.5	0.3	0.4	0.5
reference	1.5n3g50	1.5n4g50	1.5n4g50	2n3g50	2n4g50	2n5g50	3n3g50	3n4g50	3n5g50

Table 6.4: Soil properties used for parametric studies of the nested yield loci model (Case 2).

each corresponding to a constant value of $\frac{s_u}{\gamma Z}$, where s_u is the undrained shear strength of the outer surface. The dimensionless plots of $\frac{i}{D}$: $\frac{Z}{D}$ is presented in Fig. 6.13. The results obtained for both values of G_0 produced (as expected) identical dimensionless plots. The width of settlement troughs predicted for different values of $\frac{s_u}{\gamma Z}$ are similar. The results obtained from OXFEM using the linear elastic-plastic non-homogeneous model with constant undrained shear strength (Section 4.5.1) are superimposed on Fig. 6.13. It can be seen that the nested yield loci model predicts narrower settlement troughs than those for the linear elastic-plastic model. The displacement vectors obtained for the case of Z= 10m using the nested yield loci model is shown in Fig. 6.14.

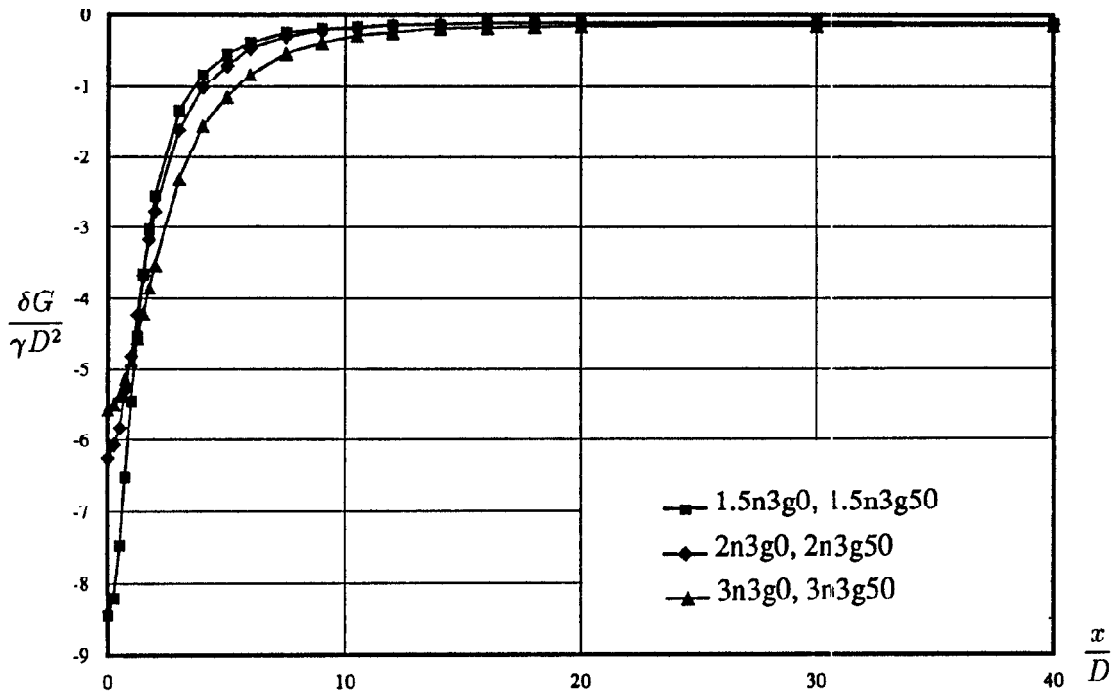

Figure 6.10: Dimensionless plot of $\frac{\delta G_0}{\gamma D^2}$: $\frac{x}{D}$ for $\frac{s_u}{\gamma Z}$ =0.3.

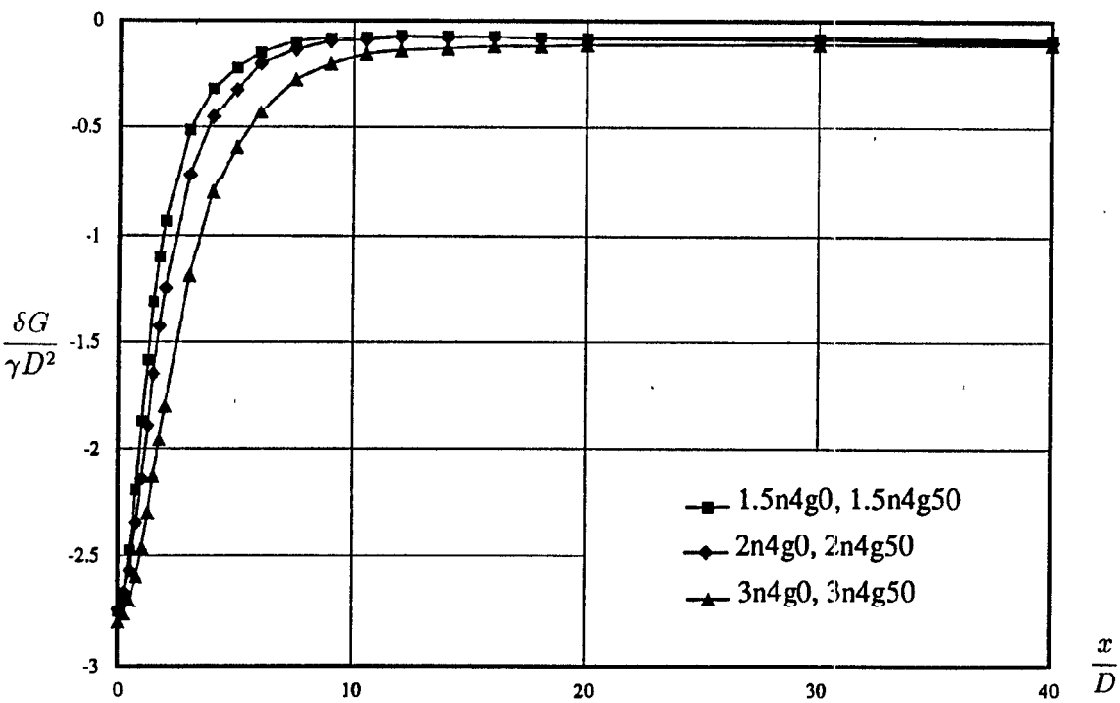

Figure 6.11: Dimensionless plot of $\frac{\delta G_0}{\gamma D^3}$: $\frac{x}{D}$ for $\frac{s_u}{\gamma Z}$ =0.4.

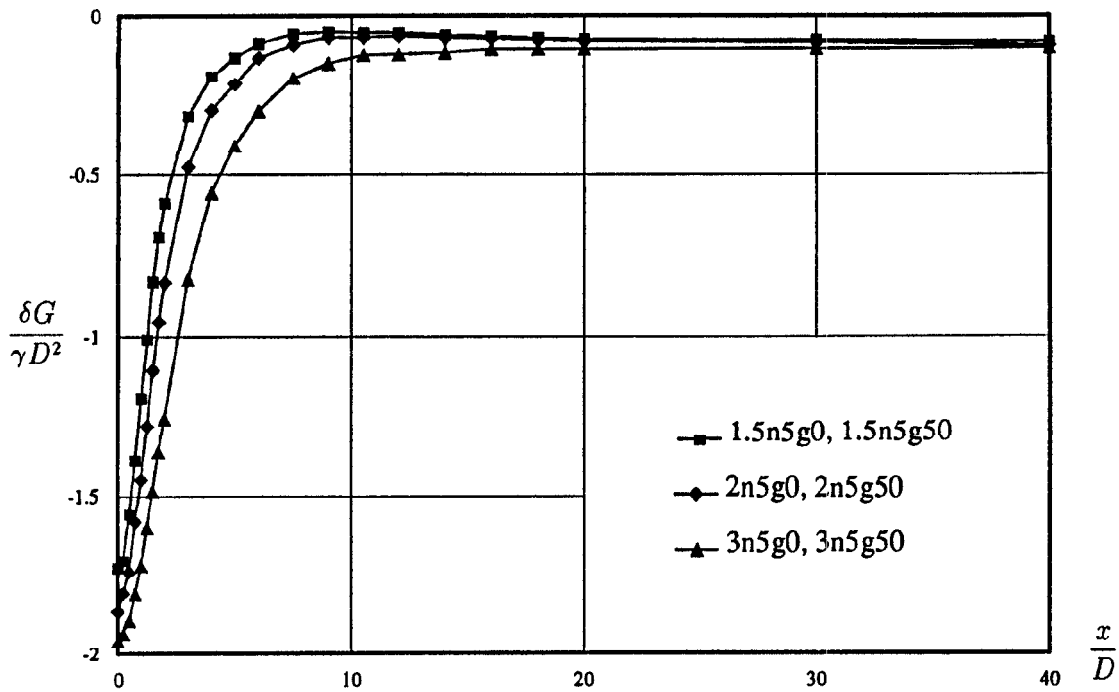

Figure 6.12: Dimensionless plot of $\frac{\delta G_0}{\gamma D^2} : \frac{x}{D}$ for $\frac{s_u}{\gamma Z}$ =0.5.

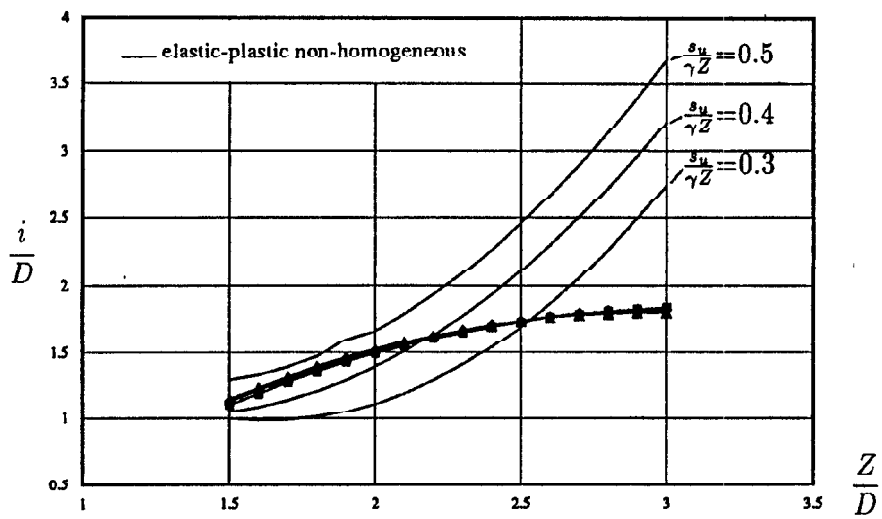

Figure 6.13: Dimensionless plot of $\frac{i}{D} : \frac{Z}{D}$ for the nested yield loci model.

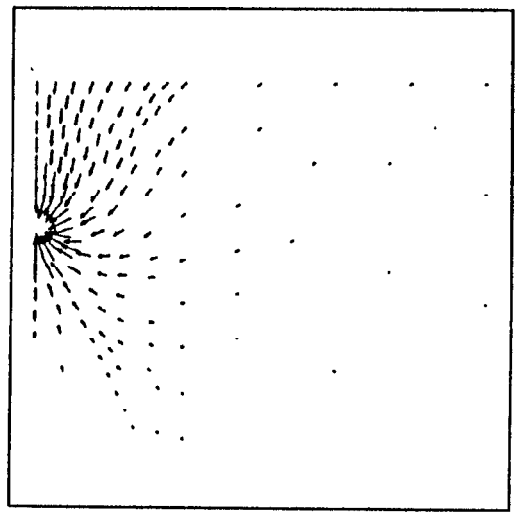

Figure 6.14: Displacement vectors obtained using the nested yield loci model for $Z = 10m$.

6.6 Predicting Settlement Profiles Using the Nested Yield Loci Model

The dimensionless plot of $\frac{i}{D}$: $\frac{Z}{D}$ for the nested yield loci model can be compared with the results from the field investigations performed by Peck (1969) to establish its ability to predict realistic values for the width of settlement trough in tunnelling problem. The results obtained by Peck for the range of $\frac{Z}{D}$ $(1.5 \rightarrow 3.0)$ used in the parametric studies are superimposed on Fig. 6.15. The point of inflection of the settlement profile, i, predicted by the nested yield loci model are in good agreement with those obtained by Peck. The shape of the curves for the nested yield loci model agree with the trend given by Peck's results.

The nested yield loci model provides better prediction of the widths of the settlement troughs than the other models that have been discussed in this thesis. Since the displacements of the soil due to tunnel excavations are

relatively small in magnitude, it is important that the soil model used for investigating this type of problem can capture the feature of higher stiffness offered by the soil during small strain deformations. The nested yield loci model can account for this effect. The stiffness predicted by the model is depended on the number of yield surfaces activated. As a result, when the strain increment is small, the behaviour of the soil is purely elastic and stiffness is higher. The predicted settlements are found more locally around the tunnel, and in closer agreement with the field data.

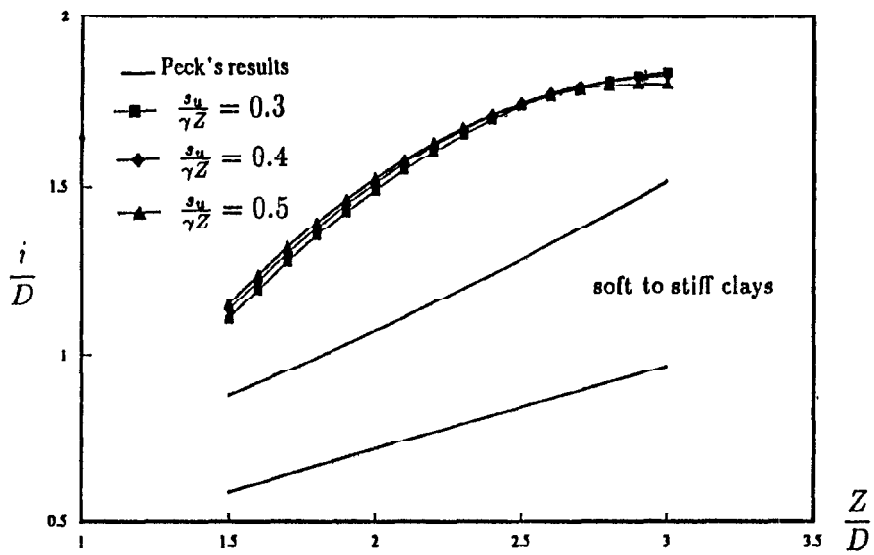

Figure 6.15: Comparison of the predicted widths of settlement troughs using the nested yield loci model with Peck's results.

Chapter 7

CONCLUSION

7.1 Summary

This thesis describes the investigation of the use of various soil models for the prediction of surface settlements due to soft ground shallow tunnelling. Methods using analytical closed form solutions and finite element modelling were examined.

Two methods were discussed in Chapter 2 to obtain the closed form solutions for the surface settlemens. The first method involved the application of a line loading in an elastic half space to model the uplift of soil caused by the removal of soil from within the tunnel. The second method, Sagaseta's method, predicted the surface displacements of soil by assuming radial movements of the soil (towards the tunnel axis) which are governed by the ground loss due to the excavation. For the first method using the line load uplift, the component of settlement associated with the contraction of the tunnel is not included, whilst the effect of stress relief caused by the excavated material is not included using Sagaseta's method. Both methods produced similar settlement profiles. The magnitude of displacements calculated using Sagaseta's method is twice that for the line load uplift solution. The width of settlement trough predicted by the two closed form solutions are identical. Comparison

of these results with the field investigation carried out by Peck (1969) showed that closed form solutions predicted narrower settlement profiles than that obtained from sites. However, both methods gave a good first approximation of the width of settlement troughs.

The method of finite element modelling used in OXFEM was discussed in Chapter 3. Two methods of simulating tunnelling process were examined: (1) application of uniform radial displacements; and (2) application of nodal forces around the periphery of the tunnel. The first method fixed the movement of soil around the tunnel, and the effect of stress relief was not included. For the second method; with the application of nodal forces, the uplift of soil due to the stress relief mechanism was taken into account, as well as the subsidence of soil due to the removal of support by the excavation. Therefore, the method of application of nodal forces was thought to be a more accurate representation of the tunnelling process. It was also shown in Chapter 3 that the size of mesh used in a finite element analysis had an important effect on the computed results. In cases where the mesh size was too small, the fixed boundaries restricted the movement of soil, producing incorrect results. For linear elasticity, the displacements of the surface of the soil increased as the mesh size was increased. This result was consistent with that obtained by Oteo & Sagaseta (1982).

Parametric studies of tunnelling using linear elastic, elastic-plastic models representing the material properties of London clay were carried out in Chapter 4. The values of undrained shear strength used for the three depths of tunnel (Z= 7.5, 10, 15m) were determined by inspecting the results for the stability of tunnels obtained by Davis *et al* (1980) using lower bound

plasticity theorem. In cases where settlement troughs could be obtained, dimensionless plots of $\frac{i}{D} : \frac{Z}{D}$ and $\frac{\delta_{max}G}{\gamma D^2} : \frac{Z}{D}$ were presented. Fig. 4.30 shows the combined $\frac{i}{D} : \frac{Z}{D}$ plot for the elastic and elastic-plastic models used in the parametric studies. It offered a useful means for comparing results predicted by various elastic and elastic-plastic soil models. The predicted width of settlement troughs decreased with the introduction of plasticity. Comparison of the results with Peck's results showed that the elastic and elastic-plastic models overestimated the width of the settlement trough.

The effect of stress amplitudes on the non-linearity of soil was considered in Chapter 5. The non-linear elastic model that has been implemented into OXFEM assumed a power law relationship between the elastic moduli and the mean effective stress. The constitutive equations used for the mathematical formulations of the model were obtained by Houlsby & Rojas (1993). The closed form solution was used to verify the implementation of the formulations. Parametric studies on tunnelling showed that the non-linear elastic model was not suitable for the prediction of surface settlements. The model predicted increasing stiffness with increasing mean effective stress, and since deformation of soil due to tunnelling produced small strains, resulting stiffness predicted by the model was low. In most cases ($n \leq 0.9$), heaves were obtained because the effect of stress relief dominated.

In Chapter 6 the effect of strain amplitudes on the behaviour of soil was discussed. An elastic-plastic model with nested yield loci was considered. The basic assumption for the nested yield loci model was that non-linearity resulted from material's plasticity. The constitutive laws for this model were derived in an attempt to describe the hysteresis effect and the path-dependent

stress-strain property of soil. Closed form solution was used to check against the implementations of the model in OXFEM. Simple test problems indicated qualitatively that the nested yield loci model could predict hysteresis effect and path-dependent stress-strain property of soil. Substantially higher stiffness was predicted for small strains deformation. The results from the parametric studies showed that the width of settlement trough predicted were smaller than those for the linear soil models (Fig. 6.13). The comparison of Peck's results with those obtained using the nested yield loci mode (Fig. 6.15) showed that the nested yield loci model agreed with the general trend established from field observations.

7.2 Concluding Remarks

From the results of the parametric studies on tunnelling carried out in this thesis, it has been shown that the nested yield loci model is the most effective model to predict the width of surface trough. Linear and non-linear elastic models are not suitable for the prediction of settlement profiles. The behaviour of soil with higher stiffness at small strains level has an important effect on the movement of soil for this type of problem. The ability of the nested yield loci model to produce hysteresis effect on unloading and reloading soil, and to describe the dependency of stress-strain on past loading history is valuable to other geotechnical problems. The model can be improved by introducing non-homogeneous property and anisotropy of the soil.

References

Burd, H.J. (1986) - *A large displacement finite element analysis of a reinforced unpaved road.* D.Phil thesis, University of Oxford.

Davis, E.H., Gunn, M.J., Mair, R.J. & Senevirate, H.N. (1980) - *The stability of shallow tunnels and underground openings in cohesive material.* Géotechnique, vol. 30, no. 4, pp 397-416.

Duncan, J.M. & Chang, C.Y. (1970) - *Non-linear analysis of stress and strain in soils.* Journals of the Soil Mechanics and Foundation Division. Proceedings of the American Society of Civil Engineers, vol. 96, no. SM5, pp 1629-1653.

Gunn, M.J. (1993) - *The prediction of surface settlement profiles due to tunnelling.* Predictive Soil Mechanics. Proceedings of the Wroth Memorial Symposium, pp 304-316.

Houlsby, G.T. & Chow, L. (1994) - *Modelling the variable stiffness of undrained clay using multiple yield surfaces.* Oxford University Department of Engineering Science Report OUEL 2024/94.

Houlsby, G.T. & Rojas, E. (1993) - *Elastic moduli of soil dependent on pressure.* Paper in preparation.

Janbu, N. (1963) - *Soil compressibility as determined by oedometer and triaxial tests.* European Conference on Soil Mechanics and Foundations Engineering, Weisbaden, Germany, vol. 1, pp 19-25.

Jardine, R.J., Symes, M.J. & Burland, J.B. (1984) - *The measurement of soil stiffness in triaxial apparatus.* Géotechnique, vol. 34, no. 3, pp 323-340.

Jardine, R.J., Potts, D.M., Fourie, A.B. & Burland, J.B. (1986) - *Studies of the influence of non-linear stress-strain characteristics in soil-structure interaction.* Géotechnique, vol. 36, no. 3, pp 377-396.

Jardine, R.J., Potts, D.M., St. John, H.D. & Hight, D.W. (1991) - *Some practical application of a non-linear ground model.* Deformation of Soils and Displacements of Structures, XECSMFE, vol. 1, pp 223-228.

Mair, R.J., Gunn, M.J. & O'Reilly, M.P. (1981) - *Ground movements around shallow tunnels in soft clay.* Proceedings of 10th International Conference of Soil Mechanics and Foundation Engineering, vol. 2, pp 323-328.

REFERENCES

Mair, R.J. & Taylor, R.N. (1993) - *Prediction of clay behaviour around tunnels using plasticity solutions.* Predictive Soil Mechanics. Proceedings of the Wroth Memorial Symposium, pp 449-463.

Mair, R.J., Taylor, R.N. & Bracegirdle, A. (1993) - *Subsurface settlement profiles above tunnels in clays.* Géotechnique, vol. 43, no. 2, pp 315-320.

Oteo, C.S. & Sagaseta, C. (1982) - *Prediction of settlements due to underground openings.* International Symposium on Numerical Models in Geomechanics, Zurich, pp 653-659.

Peck, R.B. (1969) - *Deep excavations and tunnelling in soft ground.* Proceedings of 7th International Conference of Soil Mechanics and Foundation Engineering, State of the Art volume, pp 226-290.

Poulos, H.G. & Davis, E.H. (1980) - Elastic Solutions for Rock Mechanics, John Wiley & Sons, New York..

Prevost, J.H. (1979) - *Mathematical modelling of soil stress-strain-strength behaviour.* Proceedings of 3rd International Conference of Numerical Methods in Geotechnics, Aachen, vol. 1, pp 347-361.

Sagaseta, C. (1987) - *Analysis of undrained soil deformation.* Géotechnique, vol. 37, no. 3, pp 301-320.

Simpson, B., O'Riordan, N.J. & Croft, D.D. (1979) - *Acomputer model for the analysis of ground movements in London Clay.* Géotechnique, vol. 26, no. 2, pp 149-175.

Simpson, B. (1992) - *Retaining structure: displacement and design.* Géotechnique, vol. 42, no. 4, pp 541-576.

Simpson, B. (1993) - *Development and application of a new soil model for prediction of ground movements.* Predictive Soil Mechanics, Proceedings of the Wroth Memorial Symposium, pp 628-643.

Sloan, S.W. & Assadi, A. (1993) - *Stability of shallow tunnels in soft ground.* Predictive Soil Mechanics. Proceedings of the Wroth Memorial Symposium, pp 644-663.

Wood, D.M. (1992) Soil Behaviour and Critical State Soil Mechanics, Cambridge.

REFERENCES

Zienkiewicz, O.C. (1977) The Finite Element Method, McGraw-Hill, Maidenhead.